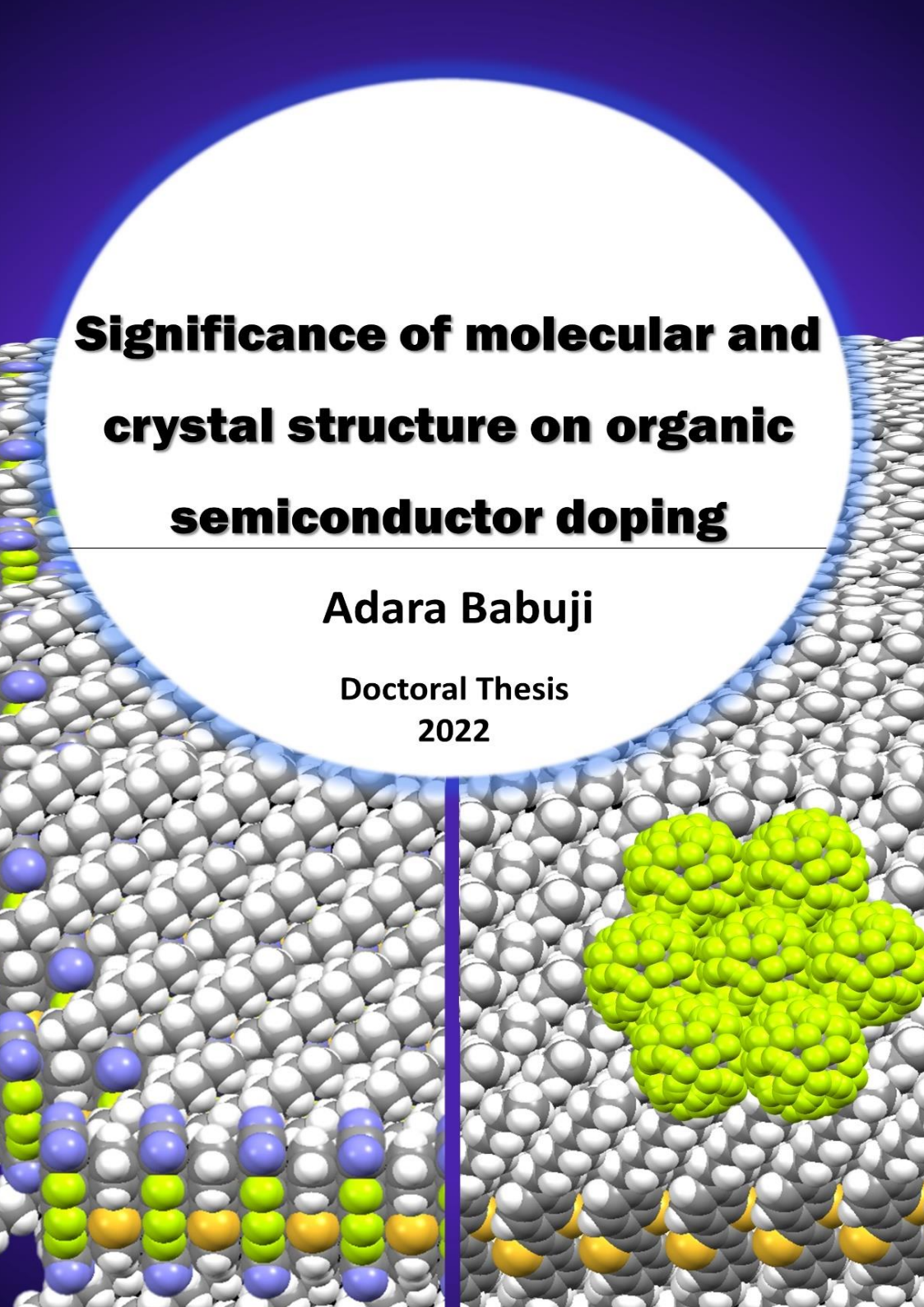


**ADVERTIMENT.** L'accés als continguts d'aquesta tesi queda condicionat a l'acceptació de les condicions d'ús establertes per la següent llicència Creative Commons:  [http://cat.creativecommons.org/?page\\_id=184](http://cat.creativecommons.org/?page_id=184)

**ADVERTENCIA.** El acceso a los contenidos de esta tesis queda condicionado a la aceptación de las condiciones de uso establecidas por la siguiente licencia Creative Commons:  <http://es.creativecommons.org/blog/licencias/>

**WARNING.** The access to the contents of this doctoral thesis it is limited to the acceptance of the use conditions set by the following Creative Commons license:  <https://creativecommons.org/licenses/?lang=en>

The background of the cover is a detailed 3D molecular model. It features a large, flat, hexagonal lattice of white spheres, representing a crystal surface. On the left side, there are vertical columns of spheres in blue, green, and orange, suggesting different chemical environments or dopants. On the right side, there is a cluster of bright yellow-green spheres, possibly representing a molecule or a specific dopant configuration. The entire scene is set against a dark blue background with a large white circle in the center, which contains the title and author information.

# **Significance of molecular and crystal structure on organic semiconductor doping**

**Adara Babuji**

**Doctoral Thesis  
2022**





---

# Significance of molecular and crystal structure on organic semiconductor doping

---



DOCTORAL THESIS  
IN MATERIALS SCIENCE

*Author:* ADARA BABUJI

*Supervisors:* Dr. ESTHER BARRENA and Dr. CARMEN OCAL

*Tutor:* Dr. EVA MARIA PELLICER VILA

Group of Physical Chemistry of Surfaces and Interfaces,  
Institut de Ciència de Materials de Barcelona

Department of Physics, Faculty of Science,  
Universitat Autònoma de Barcelona

July 2022





# Abstract

---

Organic semiconductor devices are gaining importance by opening a wide variety of applications nowadays. A key strategy for developing better performing organic electronic devices is via molecular doping, where a dopant molecule is introduced to increase charge carriers. Despite the advances in the field, very few studies have focused on understanding the structural-property relationships in molecular doping. It is well known that the structure of OSC molecules affect the crystallinity of the films but its implications on the doping mechanism and efficiency of doping have not been fully explored.

In this thesis, we explore the dopant/organic semiconductor interfacial properties in relation to the molecular structure of the employed molecules. BTBT derivatives with different side groups in combination with two dopants, which have similar ionization energy but with different molecular shapes have been chosen for the investigation. By using a combination of synchrotron-based X-ray diffraction techniques, AFM and spectroscopic methods, the interfacial properties and evolution of electronic levels during doping have been investigated.

First, the structure of the interface formed between  $C_{60}F_{48}$  and C8-BTBT has been investigated. The impact of  $C_{60}F_{48}$  on C8-BTBT OFETs was demonstrated to have a double beneficial role in improving the mobility and stability of C8-BTBT OFETs. Further investigation of the role of organic semiconductor side groups in the interfacial properties has been conducted by comparing the  $C_{60}F_{48}$ /DPH-BTBT and  $C_{60}F_{48}$ /C8-BTBT interfaces. Different interfacial morphologies are observed in both cases, which strongly affect the nanoscale work function distribution of the interface. To investigate the influence of dopant molecular structure, heterostructure films of F6TCNNQ on C8-BTBT were investigated. Unlike  $C_{60}F_{48}$ , F6TCNNQ is planar. It is observed that F6TCNNQ-C8-BTBT charge transfer complexes were forming at the interface during F6TCNNQ deposition, which generates free mobile carriers in the film hence enhancing the mobility and causing a shift in threshold voltage of C8-BTBT OFETs. Finally, characterization of charge transfer complex formation at different temperatures, inverted heterostructures and C8-BTBT-F6TCNNQ co-evaporated films have been performed.

## Acknowledgement

---

I would like to thank all people who have helped and supported me throughout my thesis. Especially, Dr. Esther Barrena and Dr. Carmen Ocal who are my mentors. I am happy to be a part of their group and it was a comfortable working space for me. I am fortunate to have mentors like them who have always supported, guided, and encouraged me during the whole journey. Both inspired me a lot with their love and curiosity towards science and their expertise. Apart from research, I am always amazed seeing them gracefully disagreeing with each other, maintaining a work-life balance, updating worldwide political scenarios, and working against gender discrimination and a lot of aspects of society. I realized that all these qualities are important and one should contribute in some way to have a better society. Thank you for helping me to develop as a person also.

I would like to thank Esther for patiently answering my millions of questions, concerns, and suggestions. I know sometimes it was too much. All those discussions helped me to have a deeper knowledge and refine my understanding of the subject. I will always cherish our discussion about politics, feminism, religion etc.

I am very thankful to Carmen for all the support and guidance. Also, for bearing with my careless writing mistakes. I felt like she has solutions for everything, whether it is about measurement set-up, data analysis, office work or other bureaucratic stuff, anything. Whenever I confront a problem, she immediately comes and finds out a solution. I felt secure, I know one way or another, I will overcome.

Another important person I am indebted to is Dr. Francesco Silvestri, yes, now I should add the title Dr. I am so glad and feel lucky that we have gone through a comparable situation together like, starting the PhD, getting the training, enrolling in the university, setting up measurements, preparing for the conferences, publishing papers, thesis defence and so many other things. I have got a responsible, organized person to look up to verify things. Thank you so much for being there and listening to all those concerns, and doubts. It means a lot. I would like to thank Prof. Eva Maria Pellicer Vilà, my PhD tutor.

I am grateful to Ana Perez who introduce me to the lab set-up and helped me with the formalities and paper works. She was very welcoming and explained

everything in the initial days. I thank Rogger Palacio for all the help and kindness. Shunya, Alba and Shaco, it was nice to share these last months with you guys. I thank Laura, Elizabeth Pach, and Rossella for their support.

I would like to thank all my collaborators, Dr. Marta Mas, Rapha, Tommaso, Ines and Jinghai from ICMB and Dr. Hans Kleemann, Prof. Karl Leo, and Carsten from IAPP, for the support and insight they have given. I would like to express my gratitude to Dr. Maria Vila (ESRF), Dr. Linus Pithan (ESRF), Dr. Alina Vlad (Soleil), Dr. Andrea Resta (Soleil) and Dr. Eduardo Solano (ALBA) for their support during the synchrotron experiments and analysis of the data.

I am taking this opportunity to thank my Amma, Achan and Monu for having faith in me.

I met a lot of nice people at ICMB. I would like to thank Pedro, Alejandro, Pamela, Jordi, Vladimir, Andrea, Arthur, Mathieu, Juri, Alex, Laia, Julia, Irene, Soledad, Jose, Simona, Sumitra and Vinod for the nice chats and memorable moments. I thank Sohini for always being there to support and encourage me.

കേരളത്തിൽ നിന്നുള്ള സുഹൃത്തുക്കൾക്ക് നന്ദി മലയാളത്തിൽ പറയാം എന്ന് വെച്ചു. എന്നെ ഏറ്റവും അധികം മനസ്സിലാക്കിയ എന്റെ ഉറ്റ സുഹൃത്തായ സനീഷിന്റെ പിന്തുണ ഇല്ലാതെ ഈ പി. എച്ച്.ഡി സുഗമമായി പോയില്ലായിരുന്നു. നന്ദി കൂട്ടുകാരാ! ഈ കാലമത്രയും എന്നെ കേൾക്കുകയും പിന്തുണയ്ക്കുകയും ചെയ്ത ആർദ്രയും, അച്ചുവിനും, രേഷ്മയ്ക്കും ഒരുപാട് നന്ദിയുണ്ട്. ബാഴ്സലോണയിൽ ഏറ്റവും കൂടുതൽ സമയം ചിലവഴിച്ചത് ദിയയുടെ കൂടെ ആണ്. ഒരുപാട് നല്ല ഓർമകൾക്കും പിന്തുണയ്ക്കും നന്ദി. വ്യന്ദ, തോമസ്, വികാസ്, റിനു, ചിത്രൻ, ജ്യോതിഷ്... ഹാ അതൊക്കെ ഒരു കാലം. ഫുഡിന്റേയും ചീട്ടുകളികളുടേയും നല്ല ദിനങ്ങൾ ഇനി എന്നാണാവോ? സൗമ്യതയുടെ അങ്ങേ അറ്റം കാണിച്ചു തന്ന ജുവൽ, എല്ലാം കേട്ടിരുന്നതിനും വിലയേറിയ അഭിപ്രായങ്ങൾ പങ്കു വെച്ചതിനും നന്ദി. കുറച്ചു കാലം മാത്രമേ ഒരുമിച്ചു ചിലവഴിക്കാൻ സാധിച്ചു എന്നുള്ളു എങ്കിലും, പ്രിയങ്കരർ ആയി മാറിയ ജെറിക്കും, കിരണിനും, ശരത്തിനും കുടുംബത്തിനും, ഗൗരിയ്ക്കും, സെബിനും, ഐശ്വര്യയ്ക്കും, അപർണയ്ക്കും, സ്റ്റേഫ്യ്ക്കും, അഷിതയ്ക്കും ഒരുപാട് സ്നേഹവും നന്ദിയും. I would like to express my gratitude to a few amazing people: Bhavna, Jean chechi, Enma and Fathma, whom I have met here in Barcelona. They helped me a lot and we shared some nice moments together.

## Publications

---

1. Adara Babuji, Inés Temiño, Ana Pérez-Rodríguez, Olga Solomeshch, Nir Tessler, Maria Vila, Jinghai Li, Marta Mas-Torrent, Carmen Ocal and Esther Barrena. Double Beneficial Role of Fluorinated Fullerene Dopants on Organic Thin-Film Transistors: Structural Stability and Improved Performance, *ACS applied materials & interfaces*, 2020, 12, 28416
2. Adara Babuji, Francesco Silvestri, Linus Pithan, Audrey Richard, Yves H Geerts, Nir Tessler, Olga Solomeshch, Carmen Ocal and Esther Barrena. Effect of the organic semiconductor side groups on the structural and electronic properties of their interface with dopants, *ACS applied materials & interfaces*, 2020, 12, 57578
3. Adara Babuji, Alba Cazorla, Eduardo Solano, Carsten Habenicht, Hans Kleemann, Carmen Ocal, Karl Leo and Esther Barrena. Charge transfer complexes in organic field-effect transistors: superior suitability for surface doping, submitted to *ACS applied materials & interfaces*
4. Francesco Silvestri, Mauricio J. Prieto, Adara Babuji, Liviu C. Tănase, Lucas de Souza Caldas, Olga Solomeshch, Thomas Schmidt, Carmen Ocal and Esther Barrena. Impact of Nanomorphology on Surface Doping of Organic Semiconductors: The Pentacene-C<sub>60</sub>F<sub>48</sub> Interface, *ACS applied materials & interfaces*, 2020, 12, 25444
5. Tommaso Salzillo, Antonio Campos, Adara Babuji, Raul Santiago, Stefan T. Bromley, Carmen Ocal, Esther Barrena, Rémy Jouclas, Christian Ruzie, Guillaume Schweicher, Yves H. Geerts and Marta Mas-Torrent. Enhancing Long-Term Device Stability Using Thin Film Blends of Small Molecule Semiconductors and Insulating Polymers to Trap Surface-Induced Polymorphs, *Adv. Func. Mat.*, 2020, 30, 2006115
6. Francesco Silvestri, Linus Pithan, Adara Babuji, Carmen Ocal and Esther Barrena. Design Dependence of the Interface Structure and Crystalline Order of Organic Semiconductor/Dopant Heterojunctions: Pentacene/C<sub>60</sub>F<sub>48</sub>, *ACS applied materials & interfaces*, 2021, 125, 5363
7. Jinghai Li, Adara Babuji, Inés Temiño, Tommaso Salzillo, Francesco D'Amico, Raphael Pfattner, Carmen Ocal, Esther Barrena and Marta

- Mas-Torrent. Chemical Doping of the Organic Semiconductor C8-BTBT-C8 Using an Aqueous Iodine Solution for Device Mobility Enhancement, *Advanced Materials Technologies*, 2022, 2101535
8. Esther Barrena, Rogger Palacios Rivera, Adara Babuji, Luca Schio, Massimo Tormen, Luca Floreano and Carmen Ocal. On-surface products from de-fluorination of  $C_{60}F_{48}$  on Ag (111):  $C_{60}$ ,  $C_{60}F_x$  and silver fluoride formation, *Phys. Chem. Chem. Phys.*, 2022,24, 2349-2356

## List of Symbols and Abbreviations

---

AFM	Atomic Force Microscopy
BE	Binding Energy
CPD	Contact Potential Difference
CTC	Charge Transfer Complex
EA	Electron Affinity
$F_0$	Amplitude of the driving force
FFM	Friction Force Microscopy
FWHM	Full Width at Half Maximum
FZ curve	Force-Distance curve
GIXD	Grazing Incidence X-ray Diffraction
$h$	Plank's constant
HOMO	Highest Occupied Molecular Orbital
$I_{ds}$	Drain-source current
$I_{off}$	Lowest drain current
$I_{on}$	Maximum drain current
IP	Ionization Potential (IP)
$k$	Force constant of the cantilever
KE	Kinetic Energy
KPFM	Kelvin Probe Force Microscopy
$L_c$	Coherence length
LF	Lateral Force
OFET	Organic Field Effect Transistor
OMBD	Organic Molecular Beam Deposition
OOP	Out-of-Plane Diffraction

OSC	Organic Semiconductors
Q	Quality factor of the cantilever
$R_c$	Contact Resistance
$r_e$	$2.813 \cdot 10^{-6} \text{nm}$ is the classical radius of an electron
RT	Room Temperature
SAXS	Small Angle X-ray Scattering
SECO	Secondary Electron Cut Off region
SP	Surface Potential
SPM	Scanning Probe Microscopy
UHV	Ultra High Vacuum (UHV)
UPS	Ultraviolet Photoelectron Spectroscopy
UV-vis	Ultraviolet- visible
VB	Fermi-edge Valence Band
$\Delta V$	Voltage drop
$V_{ds}$	Drain-Source voltage
$V_g$	Gate voltage
VL	Vacuum Level
$V_{th}$	Threshold voltage
WAXS	Wide Angle X-ray Scattering
XPS	X-ray Photoelectron Spectroscopy
XRD	X-ray Diffraction
Z	Cantilever oscillation amplitude
$\theta$	Angle of the incident X-ray beam with respect to the surface
$\vartheta$	Frequency of the photon
$\lambda$	Wavelength of the incident light
$\rho_e$	Electron density
$\varphi$	Phase shift of the oscillation
$\phi$	Work function



$\chi$	Azimuthal angle
$\omega$	Resonance frequency
$\omega_0$	Natural frequency

# Contents

---

Abstract .....	2
Acknowledgement .....	3
Publications .....	5
List of Symbols and Abbreviations .....	7
Contents .....	10
1. Motivation and Objectives .....	14
2. State of art .....	16
2.1. An overview of organic semiconductors .....	16
2.2. BTBT derivatives .....	18
2.2.1. C8-BTBT .....	19
2.2.2. Asymmetric BTBT-C8 .....	20
2.2.3. DPh-BTBT .....	21
2.3. Molecular doping .....	22
2.3.1. Ion pair formation by integer charge transfer .....	23
2.3.2. Ground state charger transfer complex formation by partial charge transfer .....	23
2.4. P-type dopants .....	24
2.4.1. C <sub>60</sub> F <sub>48</sub> .....	25
2.4.2. F6TCNNQ .....	25
2.5. Doping in OFETs .....	26
2.5.1. Doping as a solution for challenges at the dielectric/OSC interface .....	27
2.5.2. Doping as a solution for challenges at the metal/OSC interface .....	27
2.6. Doping in BTBT derivatives .....	28
2.7. Concerning aspects of molecular doping in OFETs .....	30
3. Experimental Details .....	31
3.1. Molecules .....	31
3.2. Sample preparation and film growth .....	31

3.3.	Organic molecular beam deposition (OMBD) .....	32
3.4.	AFM .....	33
3.4.1.	Contact mode.....	35
3.4.2.	Dynamic Mode .....	37
3.5.	Kelvin Probe Force Microscopy (KPFM).....	38
3.6.	X-ray diffraction.....	41
3.6.1.	Out-of-plane diffraction .....	43
3.6.2.	Grazing Incidence X-ray diffraction (GIXD).....	44
3.6.3.	Synchrotron Measurements .....	46
3.7.	Photoelectron Spectroscopy .....	48
3.8.	UV-vis absorption .....	50
3.9.	OFET fabrication and characterization .....	51
3.10.	KPFM in OFETs.....	53
4.	Contact doping of C8-BTBT OFETs with C <sub>60</sub> F <sub>48</sub> .....	54
4.1.	Structure and morphology .....	55
4.2.	Evaluation of contact doping in OFETs .....	57
4.3.	Dopant-induced morphological stability of the OSC films.....	60
4.4.	Long-term stability of doped OFETs .....	63
5.	Effect of the Organic Semiconductor Side Groups .....	66
5.1.	Interface formed between asymmetric BTBT-C8 and C <sub>60</sub> F <sub>48</sub> .....	67
5.2.	Interfacial structure of C <sub>60</sub> F <sub>48</sub> on C8-BTBT or DPh-BTBT.....	70
5.3.	Local changes in the work function .....	74
5.4.	Energy level alignment .....	78
5.5.	Contact doping of DPh-BTBT OFETs .....	84
6.	F6TCNNQ on C8-BTBT.....	88
6.1.	Co-crystal formation during F6TCNNQ deposition .....	88
6.2.	Charge transfer complex formation .....	93
6.3.	Surface doping of C8-BTBT OFET by CTC .....	96
7.	Effect of interfacial architecture in the co-crystal formation .....	102
7.1.	Role of temperature .....	102

7.1.1.	Impact of thermal annealing on the structure.....	102
7.1.2.	Impact of thermal annealing on the electrical properties .....	108
7.2.	Relevance of the deposition sequence on the co-crystal formation.....	110
7.3.	Influence of the OSC side groups on the co-crystal formation.	112
8.	Co-evaporation of F6TCNNQ and C8-BTBT.....	116
9.	Conclusion.....	121
10.	Appendix.....	123
10.1.	F6TCNNQ-C8-BTBT co-crystal formation from solution processing .....	123
10.2.	XRD features of F6TCNNQ.....	124
11.	References.....	126



# 1. Motivation and Objectives

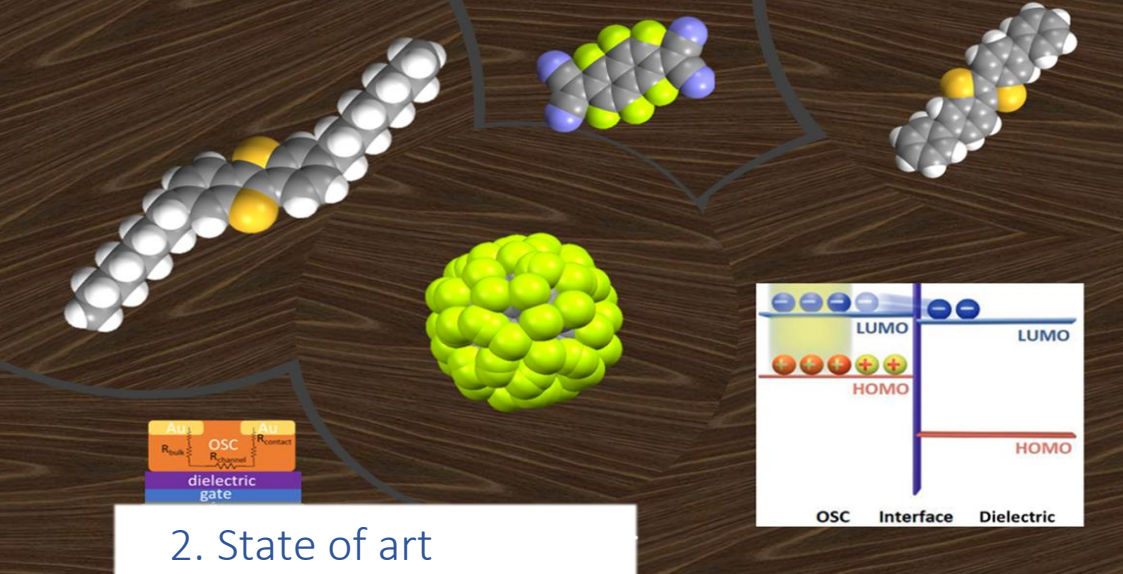
---

Over the past few decades, a large number of studies were reported about the design, optimization and fundamental mechanisms of organic semiconductors (OSC). The research in the field of organic semiconductors is growing quickly and several devices have already entered the market. Ever since Sony launched the 11 inch OLED TV in 2008, the OLED displays have been expanding their application in other electronic devices also. Even though several organic electronic devices are commercialized, aspects like mobile charge carrier formation, transport and doping mechanisms are not fully understood. Extensive research in the design and synthesis of different OSCs with enhanced mobility, environmental robustness and tuneable opto-electronic properties have been reported. However, a lack of understanding of the basic properties is a bottleneck in the field hindering the development of more efficient devices. This undesired outcome is often due to interfacial mismatches in a multi-layered device structure. Therefore, understanding the fundamental properties of interfaces and surfaces of organic semiconductors is crucial for the development of efficient device designs. Another important challenge in the field is to develop controllable and stable doping techniques. Even though the doping mechanisms in organic semiconductors are not fully understood and may depend on the particular system, it is widely accepted that the chemical structure and relative orientation of the host and dopant molecules play a key role.

The main objective of the thesis is to provide an accurate description of the dopant/OSC structural properties and to understand the influence of the molecular structure in the formation of the interface, the effectiveness of interfacial doping in OFETs and electronic characteristics of the interface. To address the influence of the molecular structure of OSC in the interface formation, two symmetric derivatives of BTBT ([1] benzothieno[3,2-b]-[1] benzothiophene) molecules, containing either phenyl or octyl side groups, were employed for the study. Hence, the OSC film surface termination will consist of the corresponding side groups, here long linear chains versus short cyclic groups. As molecular dopants, spherical  $C_{60}F_{48}$  and planar F6TCNNQ were employed to understand the effect of dopant structure on interfacial properties.

The main techniques used for the investigation are atomic force microscopy (AFM), Kelvin probe force microscopy (KPFM) and X-ray diffraction using synchrotron light. AFM combined with crystallographic measurements of the interface provides a full set of nanoscale structural information about the dopant/OSC interface. KPFM was used to investigate the surface potential distribution across the interface. In addition, photoelectron spectroscopy, as well as UV-Visible absorption spectroscopy, were employed to investigate the changes in the electronic levels with doping. In-situ and real-time X-ray and XPS/UPS measurements were also performed to follow the evolution of interface morphology and the electronic levels. The evaluation of doping in OFETs (organic field effect transistor) has been accomplished for different combinations of OSCs and dopants.

The thesis is organized as follows. Recent developments in the field of research are introduced in chapter 2. The fundamentals of OSC and molecular doping as well as the challenges in the fabrication of OFETs, which could be overcome with molecular doping are described. Chapter 3 presents experimental details and data analysis used in the thesis. The results obtained during the thesis are presented throughout chapters 4 to 8. Chapter 4 focuses on the study of the interface formed between C8-BTBT and C<sub>60</sub>F<sub>48</sub>. Enhanced structural stability and OFET performance via C<sub>60</sub>F<sub>48</sub> doping on C8-BTBT OFETS were presented. Chapter 5 presents a detailed discussion of the influence of side groups in the formation of the C<sub>60</sub>F<sub>48</sub>/BTBT interface. Chapter 6 is dedicated to the investigation of the interface formed between C8-BTBT and F6TCNNQ and the doping mechanism. This is followed in chapter 7 by a detailed study of the effect of interfacial architecture in charge transfer complex (CTC) formation. In chapter 8, the study of co-evaporated OFETs of C8-BTBT and F6TCNNQ along with the detailed structural study is reported. Chapter 9 presents the relevant conclusions gained from the thesis work. Finally, Chapter 10 presents a complementary research work done during the thesis.



This chapter briefs the evolution and recent developments in the field of organic electronics and molecular doping, which are the principal areas of interest in this thesis. The important aspects of the materials used during the research work are also reviewed.

### 2.1. An overview of organic semiconductors

Semiconductors are the fundamental building blocks of modern technologies. For flexible electronic applications or single-use devices organic semiconductors (OSC) are considered as a suitable alternative to inorganic semiconductors, because the OSCs can be deposited by low-cost, solution or vacuum-based coating at low process temperature ( $< 100^{\circ}\text{C}$ ) (and therefore enable the use of flexible substrates) and offer large bandgap tunability. Along with advances in printable electronics, organic semiconductors open a wide range of markets for low-cost electronic devices and flexible display systems.<sup>[1],[2],[3],[4]</sup> The electrical properties of organic semiconductors arise from the  $\pi$ -orbital overlap of the molecules, which facilitate electron delocalization and charge transport. The energy difference between the highest occupied molecular orbitals (HOMO) and the lowest occupied molecular orbitals (LUMO) defines the band gap of the OSC and governs its opto-electrical properties (an example is shown in Figure 2.1). Organic semiconductors can be classified into two, small molecules and polymers.



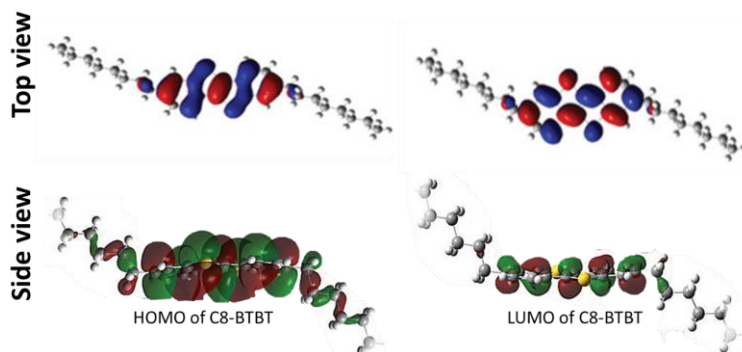


Figure 2.1. Illustration displaying the conjugated system with delocalized  $\pi$  electrons in an organic semiconductor molecule named, C8-BTBT. Adapted from ref [5],[6]

Several types of devices based on OSCs have already been developed, including solar cells, light emitting diodes (OLEDs) and field effect transistors (OFETs). Some devices are already on the market, such as OLEDs, whereas OFETs are still the subject of investigation and development.<sup>[7]</sup> This thesis focus on small-molecule OSCs used for the fabrication of OFETs.

Besides their technological interest, OFETs are used to study the basic electrical properties of organic semiconductors and to correlate them with structural information. Despite this convenient platform to study structure–property relations, individual material optimization is often addressed on a case-by-case basis in a trial-and-error fashion. The overlap of neighbouring orbitals and, herewith, the charge transport properties of OSCs films, are determined by the packing of the molecules in the solid-state. The fact that organic solids are held by weak intermolecular forces make them sensitive to the processing conditions. Thus, surface-induced polymorphism, structural variations in local molecular packing or the formation of metastable phases are common phenomena in OSC thin films.<sup>[8]</sup> The use of quantitative characterization techniques such as X-ray diffraction is the key to obtaining a description of the microstructure of the films and guiding its optimization.<sup>[9]</sup> The charge carrier mobility of OSCs, which is one of the main performance metrics for OFETs has improved from the very low values of  $10^{-5} \text{cm}^2/\text{Vs}$  of the first OFETs demonstrated in the late 1980s to values  $>10 \text{cm}^2/\text{Vs}$ .<sup>[10]</sup> This impressive progress in performance has been enabled by a broad exploration of new molecular structures by organic chemistry, a detailed understanding of the structure-property relationships, and the development of diverse engineering approaches for optimising the device

architecture.<sup>[11]</sup> However, the contact resistance ( $R_c$ ) persists as a major impediment to the further development of circuits based on organic transistors.<sup>[12]</sup> Many efforts are devoted to tailoring the contact interface to enhance charge injection/extraction in OFETs (here addressed in section 2.5.2).

Rubrene and pentacene are the most widely studied, prototypical molecular semiconductors.<sup>[8],[11]</sup> In recent years, however, organic chemistry has provided a wide range of new small molecule OSC materials that have allowed a more comprehensive understanding of the key requirements for achieving high carrier mobility. [1]benzothieno[3,2-b][1]benzothiophene (BTBT) derivatives are among the best performing p-type OFETs and are described in detail in the next section.

## 2.2. BTBT derivatives

A family of molecules with a BTBT core and with different side groups has emerged as a promising class of OSCs for p-type OFET fabrication.<sup>[13],[14],[15],[16],[17],[18],[19],[20]</sup> The reports of BTBT based OFETs with field effect mobility higher than  $1.0\text{cm}^2/\text{Vs}$  demonstrate the superior intrinsic charge transport properties among OSCs (Figure 2.2).<sup>[17],[18],[19],[21],[22]</sup>

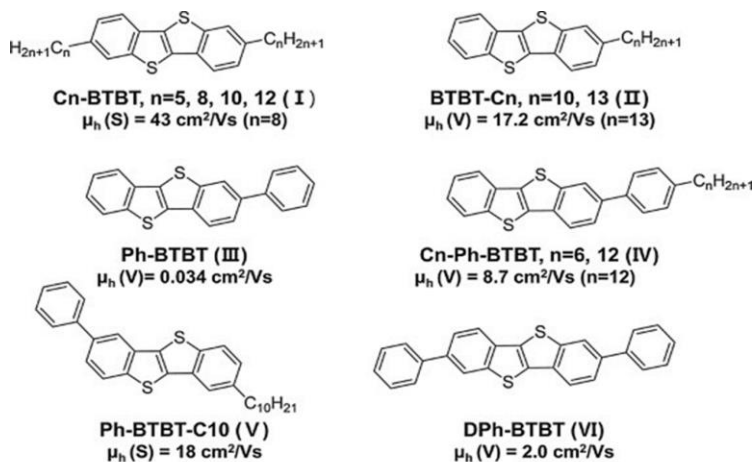


Figure 2.2. Chemical structure and maximum measured mobility for different BTBT derivative molecules. The symbols (V) and (S) denote films formed and vacuum-process and by solution-process. Adapted from ref [23]

Another attractive feature of BTBT molecules is the stable electrical performance in ambient conditions. A deep-lying HOMO of BTBT derivative molecules is the reason for ambient condition operation but is also responsible for prominent contact resistance in BTBT OFETs due to the interfacial mismatch with the contact metal.<sup>[24],[25],[14],[15],[26]</sup> Large contact resistance is detrimental for OFET performance. Besides, the degradation with time due to film dewetting, a phenomenon strongly affecting the long-term stability of BTBT OFETs, is another important challenge in the area of interest.<sup>[27],[28]</sup> An extensive study of the structure of BTBT molecules and the OFET's efficiency have been reported by varying the side groups,<sup>[16],[18],[29],[30]</sup> alkyl chain length,<sup>[15],[20]</sup> as well as incorporating atoms between the side group and the BTBT core etc.<sup>[31]</sup> The BTBT derivatives, which were employed for the investigation of this thesis are introduced in the next sections.

#### 2.2.1. C8-BTBT

One of the molecules used in this thesis is 2,7-dioctyl [1] Benzothieno[3,2-b][1] benzothiophene (C8-BTBT) (Figure 2.3a). Among the BTBT derivative molecules, C8-BTBT is widely used for OFET fabrication due to its high charge mobility and stability in the air.<sup>[19],[27],[32]</sup> The highest mobility reported is  $43\text{cm}^2/\text{Vs}$ .<sup>[17]</sup> The high mobility of C8-BTBT is attributed to the tight horizontal packing of the BTBT core due to the flexible alkyl chain.<sup>[33]</sup>

The crystal structure of C8-BTBT is monoclinic with space group  $P2_1/a$  and consists of a lamellar arrangement with a herringbone packing of the BTBT cores within the lamellae. The lattice parameters are summarized in Figure 2.3d. The packing arrangement of molecules in the thin films correspond to the bulk crystal structure only with a slight relaxation in the b lattice parameter.

Charge injection is largely determined by the alignment between the work function of the contact and the HOMO level of the semiconductor. The HOMO of C8-BTBT is 5.39eV, the LUMO is 1.55eV and the HOMO-LUMO gap is 3.84eV.<sup>[5]</sup> For widely used metal contacts, the deep HOMO is a cause of contact resistance in OFETs due to the presence of a hole injection barrier.<sup>[25],[34]</sup>

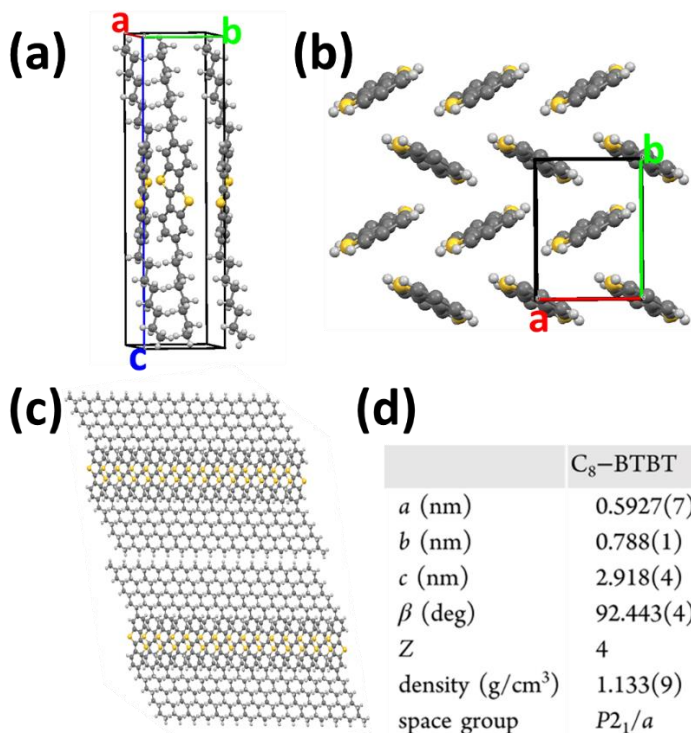


Figure 2.3. Crystalline packing structure of C<sub>8</sub>-BTBT: (a) side view and (b) top view. (c) schematic representation of the vertical alignment of C<sub>8</sub>-BTBT structure, (d) C<sub>8</sub>-BTBT unit cell parameters, *Z* is the number of molecules in the unit cell. Adapted from ref [29]

### 2.2.2. Asymmetric BTBT-C8

Synthesis of the asymmetric BTBT-C8 (octyl [1] Benzothieno[3,2-b][1] benzothiophene) molecule was reported in 2003<sup>[35]</sup> and the thin film structure was reported by Gbabode *et al.*<sup>[29]</sup> Thin films of asymmetric BTBT-C8 molecules have been reported to order in the so-called form III structure (see Figure 2.4b). This crystal phase is quite similar to that exhibited by C<sub>8</sub>-BTBT, with the main difference being formed by bilayers composed of head-to-head (or tail-to-tail) stacked molecules. Asymmetric BTBT-C8 has been less investigated than its symmetric counterpart.

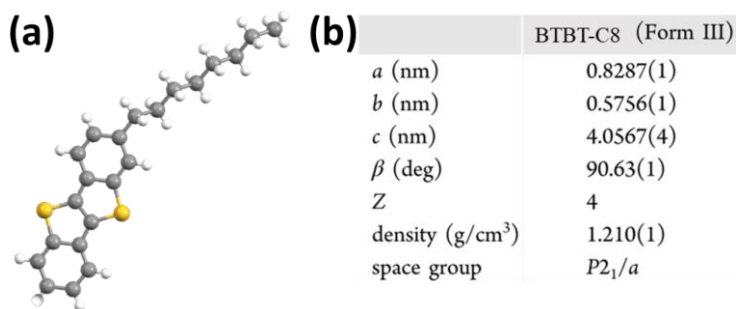


Figure 2.4. (a) Molecular structure of the asymmetric BTBT-C8 molecule. (b) unit cell parameters of the reported crystalline structure of form III, *Z* is the number of molecules per unit cell. Adapted from ref [29]

### 2.2.3. DPh-BTBT

The molecule, 2,7-diphenyl[1]Benzothieno[3,2-b][1]benzothiophene (DPh-BTBT) was first synthesized and characterized by Takimiya *et. al.*, in 2006.<sup>[30]</sup>

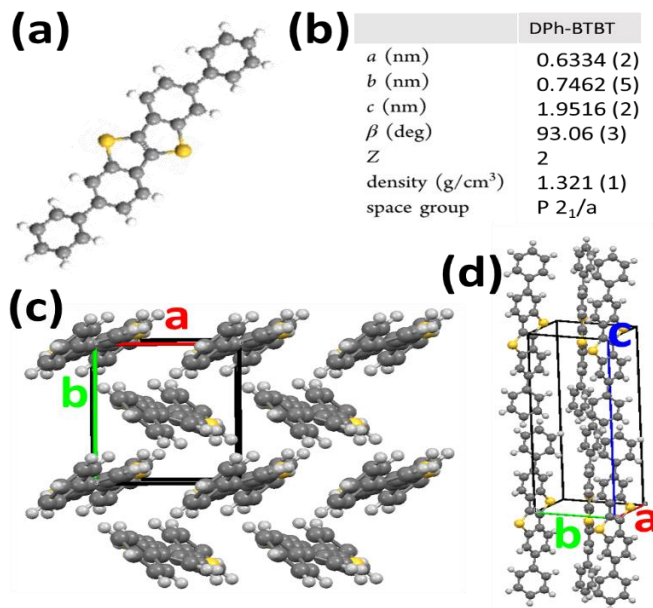


Figure 2.5. (a) Molecular structure of DPh-BTBT molecule and (b) the unit cell parameters. Crystalline packing structure of DPh-BTBT, *Z* is the number of molecules in the unit cell. (c) top view and (d) side view. Adapted from ref [36]

This molecule has an aromatic phenyl group at both ends of the BTBT core. Thin-film structure of DPh-BTBT is similar to that of C8-BTBT, with a lamellar stacking and HB packing of the BTBT cores. The unit cell is monoclinic with space group  $P2_1/a$  and the lattice parameters are given in Figure 2.5b. The higher reported mobility for DPh-BTBT OFETs is  $\sim 2\text{cm}^2/\text{Vs}$ .<sup>[30]</sup> A rigid phenyl group at both the ends hinders the tight intermolecular orbital overlap in the solid-state as indicated by a larger value of lattice parameter  $b$ , than C8-BTBT. The reported value of the HOMO for DPh-BTBT in solution is  $5.6\text{eV}$ <sup>[14],[30]</sup> and for the single crystal is  $5.41\text{eV}$ .<sup>[37]</sup> DPh-BTBT OFETs show stable electrical performances in ambient conditions.<sup>[14],[30]</sup>

### 2.3. Molecular doping

Doping a semiconductor is the process by which impurities (dopants) are intentionally introduced into the semiconductor material to modulate its electrical properties. The Fermi level or thermodynamic equilibrium position of the electrochemical potential will shift from the mid gap position towards the OSC LUMO (conduction band) by n-doping and towards the HOMO (valence band) during p-doping, which results in the modification of the optoelectrical properties of the OSC. Similar to doping in inorganic semiconductors, the charge carrier concentration in OSC also increases with doping. Successful doping of OSC was reported in the late 1970s by exposing the OSC to halides and alkali metals. But doping of OSC with atoms is not an efficient method as the dopants exhibit a tendency to diffuse due to a lack of bond formation with the OSC, which results in unstable device performances.<sup>[9],[38]</sup> Doping with molecular species came up as a viable solution to this problem. Molecular dopants can either donate electrons to the LUMO of the OSC (n-type dopants) or accept electrons from its HOMO (p-type dopants), thus leading to enhanced carrier concentration in OSC.

To enable charge transfer between dopant and the host organic semiconductor, the LUMO of p-type dopant should be deeper than the HOMO of host molecules. For n-type doping, the HOMO of n-type dopant should be shallower than the LUMO of the OSC. There are several models reported, describing the molecular doping mechanisms in OSC,<sup>[39],[40],[41],[42],[43]</sup> but none of them could describe all the doped systems. The factors leading to different doping efficiency are still debatable. In any case, degradation of the structural order of the OSC film as well as the distribution and local packing of the dopant molecules within the OSC matrix are factors that affect the effectiveness of doping.<sup>[44],[45],[46]</sup> There are two

models describing the molecular doping in OSC, which are described in the next sections.

### 2.3.1. Ion pair formation by integer charge transfer

In this model, charge carriers are generated due to the integer transfer between the organic semiconductor and the dopant (Figure 2.6).

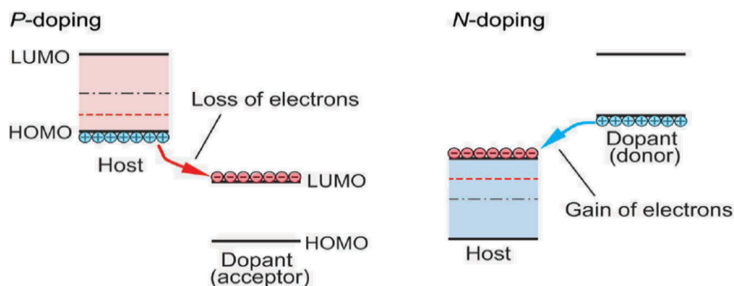


Figure 2.6. Scheme showing ion pair formation by integer charge transfer. Adapted from ref<sup>[41]</sup>

For example, in p-type doping, the transfer of electrons from the HOMO of OSC to the LUMO of the dopant is energetically favourable and results in the formation of an ion pair (dopant anion and OSC cation). This is regulated by the thermodynamic Fermi level equalization at the interface between OSC and the dopant.<sup>[39]</sup>

### 2.3.2. Ground state charge transfer complex formation by partial charge transfer

In this model, partial charge transfer occurs between the organic semiconductor and the dopant (Figure 2.7) leading to the formation of a ground-state charge transfer complex (CTC) due to the interaction between the  $\pi$ -systems of dopant and OSC molecules. Their frontier molecular orbitals hybridize, forming a bonding and an antibonding supramolecular orbital, thus exhibiting a new set of energy absorption features within the optical gap of the pristine materials.<sup>[40],[43],[47],[6],[48],[49],[50],[51],[52]</sup> Depending on the energy of the newly formed orbitals, charge transfer from OSC to CTC can take place resulting in ionized charge-transfer complexes.<sup>[41]</sup>

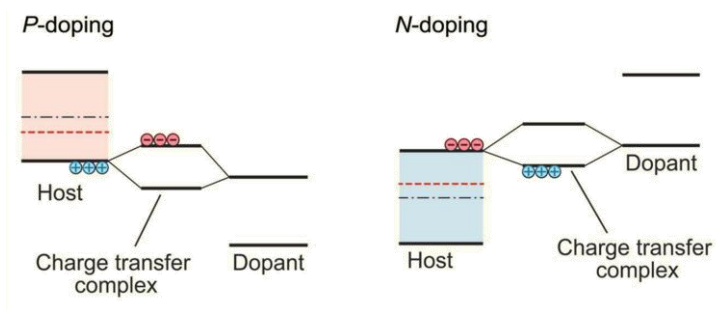


Figure 2.7. Scheme showing charge transfer complex formation by partial charge transfer. Adapted from ref <sup>[41]</sup>

As it is described in section 2.6, some reported cases of CTC formed from co-facially stacked dopant-OSC molecules forming well-ordered crystalline structures (co-crystals).<sup>[45]</sup>

## 2.4. P-type dopants

Figure 2.8 shows the energy of the LUMO for some of the most commonly used p-type dopants. Among them, F4TCNQ (2,3,5,6-Tetrafluoro-7,7,8,8-tetracyanoquinodimethane) is the most used.<sup>[53],[54]</sup>

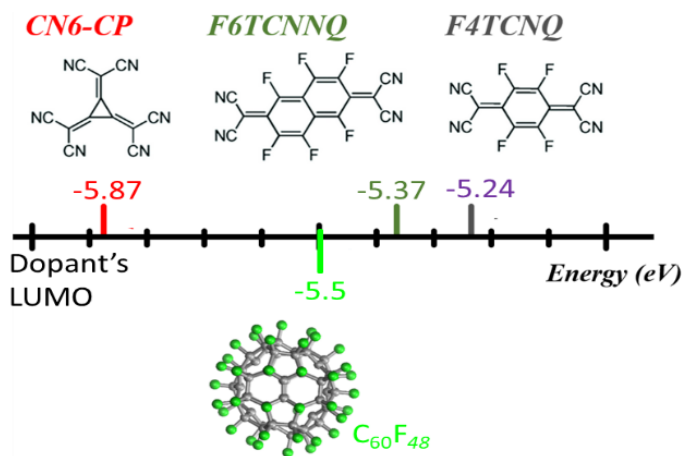
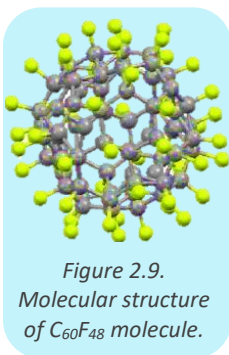


Figure 2.8. Scheme showing the energy of the LUMO of some p-dopant molecules.



The small size and planar shape of this molecule enable an efficient blending with the OSC host. This characteristic is, however, detrimental to the device stability because the diffusion of F4TCNQ into the host OSC matrix disturbs the structural integrity of the film.<sup>[55],[56],[57]</sup> The use of bulkier molecules can surmount such issues.

#### 2.4.1. C<sub>60</sub>F<sub>48</sub>



C<sub>60</sub>F<sub>48</sub> is one of the dopants used in this thesis. (Figure 2.9) The bulkier shape and size of this molecule compared to F4TCNQ, are advantageous to fabricate a well-defined dopant/OSC interface and avoid the commented inter-diffusion problems often encountered with F4TCNQ.<sup>[58],[59]</sup> It is reported that C<sub>60</sub>F<sub>48</sub> modifies the HOMO of the host OSC thin films.<sup>[59],[60],[61]</sup> Kawasaki *et. al.*, demonstrated that the structural phase adopted for this fluorinated fullerene at higher temperatures (> 353K), has the unit cell parameter of 1.716nm. While at lower temperatures, the structure is Face Centered Tetragonal (FCT) or Body Centered Tetragonal (BCT), which is derived by elongation of the FCC structure along the c axis. The lattice parameters for the BCT structures are a = 1.675nm and c = 1.79nm.<sup>[62]</sup> The transition between the two phases is reversible. C<sub>60</sub>F<sub>48</sub> dopant is stable in air when it is dry at RT.<sup>[63]</sup> The LUMO of C<sub>60</sub>F<sub>48</sub> is 5.5eV.<sup>[64],[65]</sup> As compared to its non-fluorinated parent (C<sub>60</sub>), C<sub>60</sub>F<sub>48</sub> exhibits a reduced  $\pi$ -conjugation ( $sp^2 \rightarrow sp^3$ ), an increase in band gap and a lowering of the LUMO and HOMO levels, resulting in a strong molecular acceptor.

#### 2.4.2. F6TCNNQ

The other dopant used in this thesis is F6TCNNQ (1,3,4,5,7,8-hexafluorotetracyanonaphthoquinodimethane). This molecule is also known as F6TNAP and was synthesized for the first time in 2010.<sup>[66]</sup> Unlike, the spherical C<sub>60</sub>F<sub>48</sub>, F6TCNNQ is a planar molecule. LUMO levels of both molecules has similar value, which makes the investigation of C<sub>60</sub>F<sub>48</sub> and F6TCNNQ an interesting case to study the effect of the dopant molecular structure. This material was developed as a potential p-type dopant for OLEDs. There are two polymorphs reported for the F6TCNNQ molecule: form I and form II. F6TCNNQ is an established molecular dopant for OFETs in combination with several widely used OSCs.<sup>[47],[51],[53]</sup> However, recent studies reveal the tendency of F6TCNNQ molecules to form CTC co-crystals with a

wide range of OSC small molecules.<sup>[45],[52],[42],[67],[68],[69],[70]</sup> In the case of F6TCNNQ, the reported LUMO is  $\sim 5.37\text{eV}$  and HOMO is  $\sim 7.81\text{eV}$ .<sup>[70],[69]</sup>

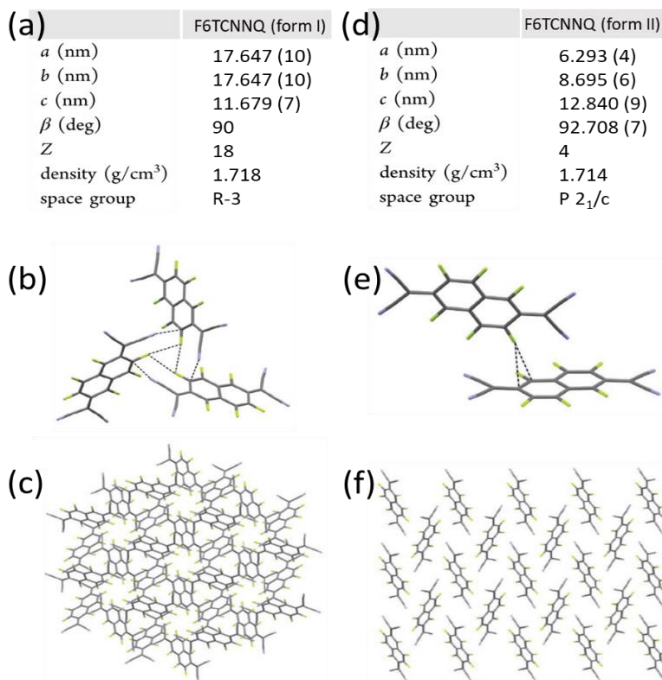
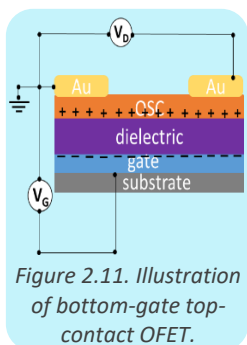


Figure 2.10. Crystalline packing of F6TCNNQ form I structure: (a) lattice parameters (b) side view and (c) top view. Packing of F6TCNNQ form II structure: (d) lattice parameters (e) top view and (f) side view. Adapted from ref<sup>[71]</sup>

## 2.5. Doping in OFETs

Electric field-controlled charge transport in an organic material was first identified by Koezuka *et. al.*, in 1986 in a polythiophene film.<sup>[72]</sup> Since then, there has been a thrive to develop a tuneable, cost-effective alternative to silicon-based FETs and notable advancements has been made to employ organic options in e-paper displays, chemical and biological sensors and flexible OLEDs.<sup>[73]</sup>

The conventional OFET consists of three electrical contacts: the gate, the source, and the drain (Figure 2.11). The conductive channel forms in the OSC



layer between source and drain. The conductivity of the channel between the source and the drain is controlled by the voltage applied at the gate. Hence the important interfaces of the OFETs contributing to its efficient performance are the interface between the OSC and the dielectric and the interface between the OSC and the contacts. Any issues in these parts result in a non-ideal transistor behaviour. Molecular doping in OFETs can be used in a variety of ways to solve the non-ideal behaviour of OFETs as well as to enhance mobility by providing extra charge carriers which are discussed below.

#### 2.5.1. Doping as a solution for challenges at the dielectric/OSC interface

The conducting channel is formed at the few semiconductor layers near the dielectric/semiconductor interface. This interface is prone to have charge traps, which could evoke a decrease in drain current as well as an increase in threshold voltage. In the widely used  $\text{SiO}_2$  dielectric, charge traps can be generated from oxygen vacancies and adsorbed water and oxygen with  $\text{SiO}_2$  forming  $\text{SiOH}$  groups. This can shift the threshold voltage and lead to the degradation of n-channel OFETs. After electron carriers are trapped in these sites, they no more contribute to drain current but altogether act as a space charge layer. These space charge layers create an electric field which bends the electronic bands of the semiconductor. The charges trapped at the dielectric/OSC interface might be injected into the channel while the OFET is in operation which results in a double slope in transfer characteristics.<sup>[73]</sup> Using materials with a lower tendency to form traps as dielectric does not solve the problems fully because a lower dielectric constant and capacitance results in a high operating voltage and subthreshold region. Hence molecular doping is advocated as a solution to passivate the traps. Charges formed by doping can fill the traps at the dielectric-OSC interface as well as hinder minority charge carriers.

#### 2.5.2. Doping as a solution for challenges at the metal/OSC interface

A Schottky electric potential barrier at the metal contact causes a contact resistance. This resistance decreases the effective drain-source voltage. Different scenarios can contribute to contact resistance such as an energy

mismatch at the interface (between the work function of the metal and the HOMO level of the OSC, for p-type transport) and unfavourable interfacial morphology at the contacts, etc. Moreover, in bottom-gate top-contact (BG-TC) devices, the charge carrier transport across the film also contributes to the contact resistance (access resistance).

A key strategy for the enhancement of device properties is contact doping, where a dopant thin layer is incorporated at the source and drain metal/semiconductor interface, i.e., inserting a dopant layer between the OSC and the metal in the BG-TC geometry. The dopant modifies the width of the Schottky barrier and fills trap states that exist in the access region. Nevertheless, the thickness of the dopant layer must be carefully optimized and sometimes it can induce changes in the microstructure of the semiconductor layer (by diffusion and/or intermixing), which causes prominent issues related to the stability of the doped interfaces.<sup>[12],[74],[75],[76],[77],[78]</sup>

## 2.6. Doping in BTBT derivatives

As described before, the deep-lying HOMO of BTBT derivative molecules is beneficial for ambient condition operation but is also the reason for prominent contact resistance in BTBT OFETs.<sup>[24],[25],[14],[15],[26]</sup> Hence contact doping is widely used to fabricate higher efficiency BTBT derivatives OFETs. Organic<sup>[27],[79],[80]</sup> and inorganic<sup>[25]</sup> p-type molecular dopants<sup>[81],[82]</sup> have been employed but it has been reported that the diffusion of small molecular weight dopants<sup>[55],[83],[57]</sup> adversely affects the microstructure of the OSC thin film and worsened the OFET performance with time.<sup>[80]</sup>

Experimentally, bulk doping can be obtained by exposing a pristine OSC to doping agents (in the liquid or gas phase) but also by forming a solution of a mixture of a host-dopant that is directly deposited or by co-evaporation of OSC and dopant, to become a doped composite OSC layer. It is reported that after dopant incorporation in the bulk of the BTBT layer, the OSC microstructure is destroyed and restricts the enhanced device performance.<sup>[6],[54],[84]</sup> A wide range of studies on doping in BTBT derivative molecules have been reported in the past years and most of them reveal the formation of a ground-state charge-transfer complex. Mendez *et. al.*, in 2013 provided one of the early reports of molecular doping by CTC, attributed to the co-crystallization in solution of C10-BTBT and different TCNQ derivative molecules. It was demonstrated that the co-crystals are doping the C10-BTBT film, using different characterization techniques. Figure 2.12a and b show the

evolution of (the proposed CTC structure is shown in Figure 2.12) UV-Vis absorption and X-ray diffraction data with respect to the increase in dopant ratio. The conductivity was observed to increase with the dopant ratio (Figure 2.12c), achieving a maximum value for a dopant concentration of 5 mol% and decreasing beyond this value.<sup>[45]</sup>

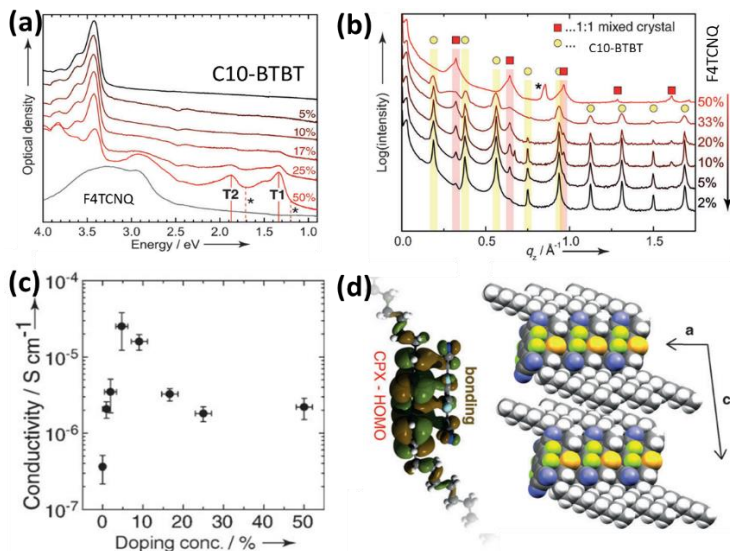


Figure 2.12. (a) UV-Vis absorption spectra (T1 and T2 are the transitions from the CTC), (b) specular XRD (yellow circles are C10-BTBT reflections and red squares correspond to co-crystals) and (c) Conductivity of films of C10-BTBT doped with F4TCNQ at different ratios. (d) Scheme of CTC crystal structure along with the corresponding orbital iso-surface plots of the hybrid orbitals calculated by DFT. Adapted from ref <sup>[45]</sup>

Synthesis and characterization of co-crystals based on BTBT derivatives reveal the potential applications of the co-crystals themselves as a new class of OSC.<sup>[53],[85],[86],[71],[87]</sup> Several articles have further confirmed that the CTC formed between the BTBT derivatives and the TCNQ derivatives in the bulk are doping the OSC films.<sup>[88],[89],[90]</sup> However, these results also reveal the difficulty to control the microstructure, order and spatial distribution of the co-crystalline regions within the OSC film.

Only a few articles mention the integer charge transfer doping mechanism in BTBT derivative thin films. Paterson *et. al.*, achieved hole mobility exceeding  $13\text{cm}^2\text{V}^{-1}\text{s}^{-1}$  in C8-BTBT: C<sub>16</sub>IDT-BT OFETs via p-doping with 1wt% C<sub>60</sub>F<sub>48</sub> as well

as revealed the presence of the ion-pair formation between C<sub>60</sub>F<sub>48</sub> and C8-BTBT.<sup>[76]</sup>

## 2.7. Concerning aspects of molecular doping in OFETs

Molecular doping is a strategic tool to develop organic electronic devices with versatile properties but still, there is a lack of understanding of the factors governing doping. The factors may vary depending on the system; however, it is widely accepted that the microstructure of the host OSC, the relative orientation of host and dopant molecules and their interface play key roles. Another limiting factor is the increase in the off current in doped OFETs due to the presence of a large number of charge carriers. These charge carriers are either formed in the film or injected from the contacts due to the lower energy barrier at the contact. In some doped devices, an opposite gate polarity was required to turn off the conductive channel.<sup>[91],[92]</sup> Also, care should be taken in bulk doping of OSC film, because it can adversely affect the molecular packing of the film and worsen the performance.<sup>[45],[43],[93],[44],[55],[56],[57],[52]</sup> Hence, in order to get doping without deteriorating other device parameters, which is essential to obtain efficient devices, a deeper understanding of the interfacial properties as well as the factors affecting the interface between the dopant-OSC is required.



### 3. Experimental Details

#### 3.1. Molecules

C8-BTBT and asymmetric BTBT-C8 were purchased from Sigma-Aldrich and F6TCNNQ from Novald AG Dresden as a part of a collaboration work. All molecules were used without further purification except in-situ degasification. DPh-BTBT and  $C_{60}F_{48}$  were provided by other research labs as a part of collaboration work. DPh-BTBT has been synthesized according to an established procedure<sup>[30]</sup> by the group of Dr. Yves H. Geerts, Laboratoire de Chimie des Polymères, Université Libre de Bruxelles (ULB), Belgium. Fluorinated fullerene  $C_{60}F_{48}$  was provided by Nir Tessler and synthesized as per the method developed at the Josef Stefan Institute (Slovenia).<sup>[94]</sup> The product was characterized by chemical analysis, electron-ionization mass spectrometry and IR-spectroscopy. The estimated purity was 95%. All molecules were degassed under vacuum at 120°C for 15min.

#### 3.2. Sample preparation and film growth.

Thin films were either grown on Si wafers with native oxide or thermally grown thick  $SiO_2$  or glass as indicated in the respective sections. All these substrates were cleaned by ultra-sonication in acetone and then in ethanol for 10 - 15min each. Soon after ultra-sonication, the substrates were dried

with nitrogen flux. Before thin film deposition, substrates were in-situ annealed under vacuum at 250°C for 10min.

### 3.3. Organic molecular beam deposition (OMBD)

The OMBD method is a widely used technique to fabricate organic epitaxial thin films. The molecules are sublimated by increasing the temperature under high vacuum ( $< 10^{-6}$  mbar) conditions. Molecules in powder form are placed inside a crucible in the Knudsen/effusion cell. The rate is tuned by adjusting the temperature of the crucible with an electrical current controller and is monitored with a quartz crystal microbalance (QCM). Both are in the cone range of the cell. A shutter in the substrate holder is used to cover the samples until the required deposition rate is achieved. The position of the shutter can be controlled manually from outside the chamber in order to cover certain regions of the substrate holder, which aids to grow films with different thicknesses from a single deposition. The photos of the OMBD set-up are shown in Figure 3.1. For in-situ electrical measurements, the electrical feed-throughs at the bottom of the chamber are used. To desorb contaminants and moisture, substrates are heated up to 250°C and crucibles to 120°C. Transmission electron microscopy (TEM) grids were used as shadow masks where indicated.

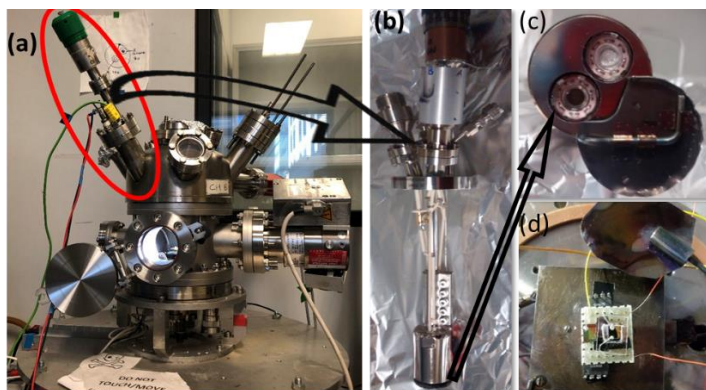


Figure 3.1. Photos of (a) evaporation chamber (b) Knudsen cells (c) top view of the cells with the shutter open and (d) the sample holder with its shutter. The shown sample is an OFET connected for in-situ characterization.



### 3.4. AFM

Atomic force microscopy (AFM) is a technique under the family of different scanning probe microscopy (SPM) techniques, which scans the sample surface with a probe. Atomic force microscopy was developed in 1986 by IBM scientists as a technique that can be used to probe even non-conductive samples in the ambient atmosphere<sup>[95]</sup>. AFM is a powerful technique which can be used to measure the surface of almost everything. Also, different properties of the surface like friction, adhesion, conductivity, work function, magnetic potential, piezo electric potential etc., can be probed using different measuring modes with AFM.

The chemical structure of pentacene was the first high resolution image obtained using AFM and was a game-changer in the field of SPM imaging.<sup>[96]</sup> Figure 3.2 shows the images of pentacene on Cu(111) measured in 2009, resolving the atomic positions and the bonds. The frequency shift maps are sensitive to the electron density and are giving contrast as in Figure 3.2c.

In common AFM, the probe is a very sharp tip with a tip radius in nanometers (ideally equal to the diameter of a single atom). This tip is attached to a flexible cantilever.

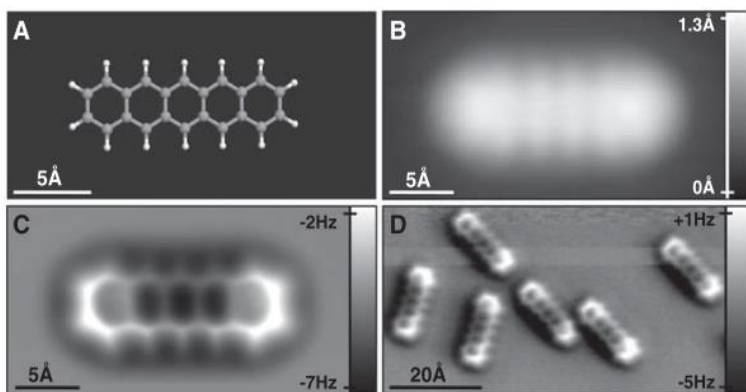


*Figure 3.2. STM and AFM imaging of pentacene on Cu (111). (A) Ball-and-stick model of the pentacene molecule. (B) Constant-current STM and (C and D) constant-height frequency shift AFM images of pentacene acquired with a CO-modified tip. Adapted from ref <sup>[96]</sup>.*

The force between the sample surface and the tip causes a deflection of the cantilever that is detected and used as a feedback signal to keep at a constant

value of the force between the tip and the sample. When the tip scans the sample surface, height variation in morphology induces a deflection in the cantilever. To keep the force constant, the distance between the sample and the tip is adjusted according to the feedback. The vertical movement of the sample with respect to the tip is monitored and used to obtain topographic images. The movement of the tip is probed with a collimated laser that is focused on top of the cantilever. The cantilever has a reflective coating of gold or aluminium. The deflection of the laser is monitored with a four-segmented photodiode (Figure 3.3). Before starting the measurement, the photodiode should be positioned in a way that the four segments are equally illuminated. During the scan, if the cantilever bends upwards following the taller regions in the morphology (due to normal force) then the laser illuminates the two upper segments more, which corresponds to a deflection in the z-direction, and vice versa for the deeper regions in the morphology. When the tip experiences friction with the sample, the cantilever twists and the laser beam move sideways illuminating photodiode segments on one side.

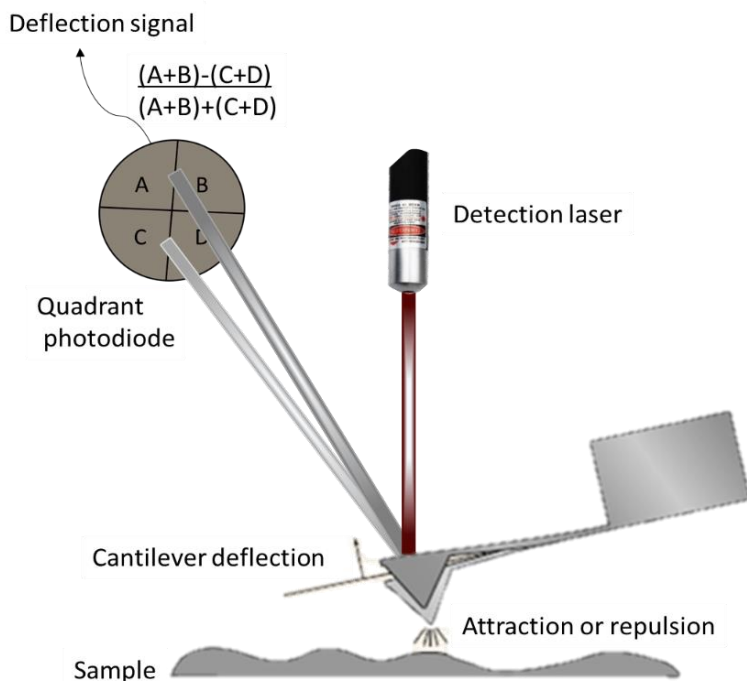
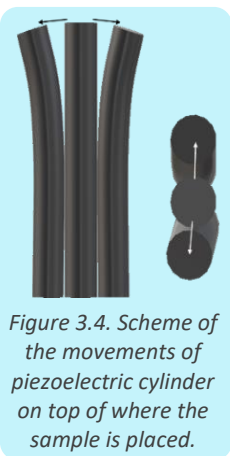


Figure 3.3. Scheme showing laser deflection due to the bending of the cantilever during the measurement.



The amount of torsion of the cantilever due to friction is derived from the comparison of two left-hand and two right-hand segments of the photodiode. The material, coating of the tip, shape and size of the cantilever, and movement of the tip or sample vary between AFMs and different modes of AFM. All the measurements reported in this thesis were carried out under ambient conditions using a commercial head and control unit from Nanotec Electrónica S.L. In our AFM setup, the tip is kept fixed in the AFM head along with the laser, optical components and photodetector. The sample, placed on a piezoelectric tube and secured by magnets, moves during the measurement. The position and movement of the sample are controlled by an electronic feedback loop via the piezo ceramic tube (Figure 3.4).

To avoid electromagnetic and mechanical noises affecting the measurement, the whole set-up is kept inside a metallic cabin, which in turn is fixed on a heavy plate supported by four springs. We employed two main modes of operation of AFM in this thesis: contact mode and dynamic mode.

#### 3.4.1. Contact mode

In contact mode AFM measurements, the tip is in direct contact with the sample surface while the vertical deflection of the cantilever is kept constant by a feedback loop. Microscopically, different forces are involved in the process. Figure 3.5 shows the force experienced by the tip versus the tip-sample distance. During the approach of the tip towards the sample, the cantilever deflection is approximately constant until an attractive interaction such as van der Waals forces, electrostatic or capillary forces, and the tip bends downwards. When this attractive force becomes greater than the force by the cantilever spring, the tip snaps into physical contact with the sample; adhesion of the tip to the sample occurs. Once the tip is in contact with the sample, the cantilever deflection is linear with the further approach. When the tip is retracted from the sample after being in contact, the tip sticks to the sample by the adhesion until the retraction pulls the tip out of contact. The deflection of the tip is monitored with a photodiode during the approach and retraction, which is recorded as a function of the tip-sample distance. In the linear part of the repulsive regime, the cantilever behaves like a spring. The bending of the cantilever can be converted to the normal force (perpendicular to the surface) of the surface experienced by the tip, using the spring constant of the cantilever. Figure 3.5b shows a typical normal force versus AFM tip-

sample distance (FZ curve). The arrows in the curves show the direction of the tip motion during the approach-retraction sequence.

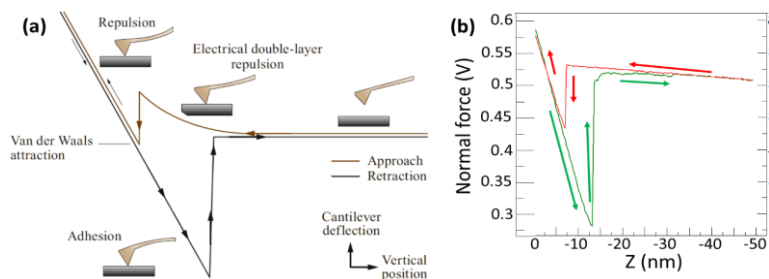


Figure 3.5. (a) Scheme demonstrating the tip-sample interaction w.r.t the distance between them. The image is taken from ref <sup>[97]</sup>. (b) Normal force vs. AFM tip-sample distance curve.

During AFM imaging, the tip in physical contact with the sample may alter and can result in a damaged surface and/or the tip. Most measurements during this thesis consist of organic surfaces, which are soft. Hence, to obtain AFM images with maximum resolution, care has been taken to measure the samples at minimal load. There is a hysteresis in the normal force versus tip-sample distance curve while approaching and retracting. The minimal force experienced on the tip is during the retraction while the adhesion force dominates. So, the AFM images taken during this thesis are measured at a tip-sample distance where adhesion dominates (distance corresponds to the lowest point of the green curve).

As mentioned before, the AFM cantilever can also twist left or right along with bending up or down, due to the frictional force between the tip and the sample. A difference in friction between regions on a surface can arise from their different mechanical properties, chemical compositions, density or structures. In conventional AFM, the fast-scanning direction ( $\pm x$  axis) is perpendicular to the cantilever's long axis direction which coincides with the slow scan direction ( $\pm y$  axis). The torsion of the cantilever at each point on the surface responds to the frictional inhomogeneity of the sample surface that results in a lateral deflection of the laser spot on the photodiode, the imaging channels are named "lateral force," forward ( $LF_f$ ) or backwards ( $LF_b$ ) for right or left fast scan directions, respectively. A friction map of the surface is obtained by subtracting the lateral force maps and dividing by two (i.e.,  $F = (LF_f - LF_b)/2$ ). However, because no quantitative analysis of friction is made in this thesis, only images obtained from the forward scans are used, in which

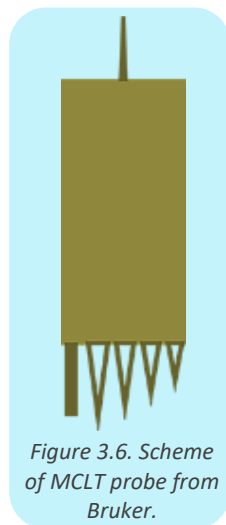


Figure 3.6. Scheme of MCLT probe from Bruker.

lower and higher friction corresponds to a darker and lighter colour, respectively.

During this thesis, for contact mode measurements, MLCT probes from Bruker were used. Each probe has a rectangular and five different triangular cantilevers, with metal-coated silicon nitride tips (Figure 3.6). The spring constants of the cantilevers are from 0.016N/m to 0.6N/m.

### 3.4.2. Dynamic Mode

Unlike contact mode, in dynamic mode, the tip is not in direct contact with the sample surface but set to mechanically oscillate in its natural frequency ( $\omega_0$ ) at a certain distance from the surface. The interaction of the tip with the sample is evaluated by monitoring the changes in the cantilever dynamics (amplitude, frequency, and phase) with respect to a reference. The cantilever is driven to mechanical oscillation by electrical excitation of a small piezo actuator placed in the cantilever holder. The resulting force oscillator is mathematically analogous to a point mass-spring whose motion can be approximated by a non-linear second order differential equation (eqn 3.1).

$$m \frac{d^2 z(t)}{dt^2} + \frac{m\omega_0}{Q} \frac{dz(t)}{dt} + kz(t) = F_{ts} + F_0 \cos \omega t \quad (\text{eqn 3.1})$$

Where  $\omega$  and  $F_0$  are the frequency and the amplitude of the driving force,  $Q$  and  $k$  are the quality factor and the force constant of the cantilever, respectively.  $F_{ts}$  is the force between the tip and the sample. When the tip is far from the sample,  $F_{ts}$  is zero and the system behaves like a forced harmonic oscillator with damping.

The cantilever probe is electrically connected to a piezoelectric component (actuator) which applies a sinusoidal excitation with a frequency  $\omega$  and amplitude  $A$ , which maintains the mechanical oscillation of the tip in its natural frequency against the damping. Hence the cantilever oscillates in a steady state around its equilibrium position and eqn 3.2 shows the corresponding equation of motion of the cantilever.

$$z(t) = Z(\omega) \sin(\omega t + \phi(\omega)) \quad (\text{eqn 3.2})$$

For the AFM used during the thesis, the recommended amplitude for the tip oscillation is around 3.5V (obtained from the photodiode signal). This is the case where there is no interaction with the sample. During AFM imaging, cantilever oscillation amplitude ( $Z(\omega)$ ), its resonance frequency ( $\omega$ ), and the phase shift ( $\varphi$ ) of the oscillation vary due to the tip-sample interaction. Generally, conservative forces due to van der Waals interaction, polarization, electrostatics, Pauli repulsion etc., cause a shift in resonance frequency. Dissipative interactions from plastic deformation, viscosity etc., cause a decrease in amplitude and  $Q$ , which can be used as a feedback signal to measure the topography. There are two basic modes of operation possible to restore the resonance condition, which are either by modulating frequency (frequency modulated AFM, FM-AFM) or by modulating amplitude (amplitude modulated AFM, AM-AFM). AM-AFM was used in this thesis. In this mode, the sample is moved away or closer to the tip to restore the resonance amplitude. The amplitude of the tip is the input for the feedback loop to construct the sample topography. A proportional-integral-derivative (PID) controller is used to maintain the distance between the tip and the sample constant.<sup>[98]</sup> Presence of different materials on the surface results in a phase difference between the natural frequency of the tip and the external frequency applied by the piezoelectric component. This is given as another channel in the dynamic mode called “phase” and is influenced by the chemical nature of the surface. There is another optional feedback loop called PLL (phase-locked loop), which maintains the phase constant. The additional frequency applied to compensate for the phase shift is provided as a new channel called “frequency shift” and gives the same information: the chemical nature of the surface.

A lot of tips and cantilevers with different spring constants are commercially available and must be chosen wisely depending on the sample properties and measurement modes. The dynamic experiments for this thesis were done with ElectriMulti75-G cantilevers from Budget Sensors (natural frequency = 75kHz,  $k = 3\text{N/m}$ ) with only one tip and cantilever per probe with an electrically conductive Cr/Pt coating.

### 3.5. Kelvin Probe Force Microscopy (KPFM)

KPFM is a technique which uses AFM to measure the surface potential map/work function difference of a surface by measuring the contact potential difference (CPD) between the AFM tip and the sample. The work function of a material is the minimum thermodynamic work required to remove an

electron from the surface of a given material to infinity. When two materials are electrically connected, a potential difference develops at the contact. As shown in Figure 3.7, when two metals of different work functions are electrically in contact, charges flow from one to the other to align the Fermi level. This causes opposite charges to build up in each of the materials which results in an electrostatic potential force between them, modifying the vacuum level (VL). This change in the VL is the CPD, in effect the same as the work function difference of both materials. The concept was first discussed by Lord Kelvin thus the technique got the name.<sup>[99]</sup> The method used in KPFM to measure the CPD was adapted from the work published by William Zisman.<sup>[100]</sup> It is impressive that the method was developed as a part of his Master's thesis at MIT in 1928. Two electrically connected materials with different work functions in proximity are considered as parallel plate capacitor.

Zisman reported that a mechanical oscillation of the capacitor generates an alternating electrical current which can be nullified by applying a DC bias ( $V_{DC}$ ) equal to the CPD difference between the two materials (Figure 3.7). In KPFM, a  $V_{DC}$  is applied to cancel the CPD between the tip and the sample at each point of the surface, hence the final image of the surface is called the surface potential (SP) map. Contrary to the Kelvin/Zisman method, in KPFM the electrostatic force is detected and nullified. Surface regions with different work functions result in a different CPD with the tip and show contrast in the SP maps.

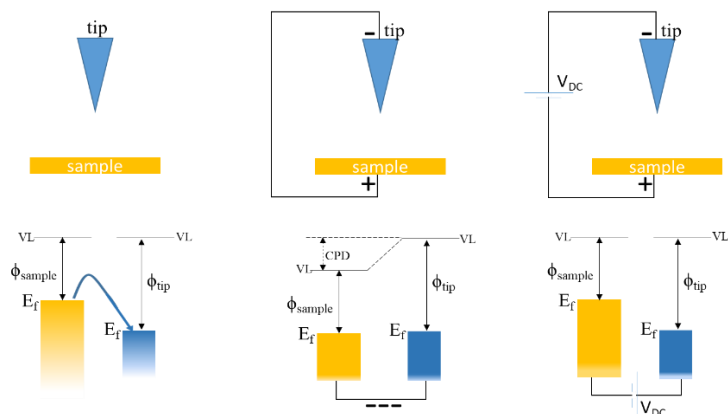


Figure 3.7. Scheme showing the concept of CPD and the method used to measure CPD with KPFM.

In KPFM an alternating voltage is applied between the tip and the sample with an amplitude  $V_{AC}$  and frequency  $\omega_{AC}$ . Along with the DC bias, the total electrostatic force between the tip and the sample which has an AC voltage component,  $F_{El, AC}$

$$F_{El, AC} = -\frac{1}{2} \frac{dC}{dz} [(V_{DC} - CPD) + V_{AC} \sin(\omega_{AC} t)]^2 \quad (\text{eqn 3.3})$$

This electrostatic force can be expressed as a sum of three independent terms

$$F_{El, AC} = F_{DC} + F_{\omega AC} + F_{2\omega AC} \quad (\text{eqn 3.4})$$

where,

$$F_{DC} = \frac{dC}{dz} [(V_{DC} - CPD)]^2 + \frac{1}{2} V_{AC}^2 \quad (\text{eqn 3.5})$$

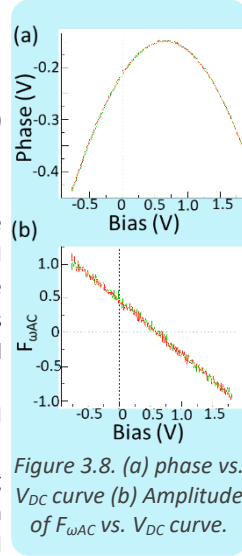
$$F_{\omega AC} = \frac{1}{2} \frac{dC}{dz} (V_{DC} - CPD) V_{AC} \sin(\omega_{AC} t) \quad (\text{eqn 3.6})$$

$$F_{2\omega AC} = \frac{1}{4} \frac{dC}{dz} V_{AC}^2 \cos(2\omega_{AC} t) \quad (\text{eqn 3.7})$$

There is no frequency term in  $F_{DC}$  and it induces a constant deflection of the cantilever. The AFM we used, takes  $F_{\omega AC}$  for the feedback loop for KPFM. Also, frequency modulated KPFM increases the lateral resolution of the map.

$$\Delta\omega \propto \frac{dF_{\omega AC}}{dz} \quad (\text{eqn 3.8})$$

When  $V_{DC} = CPD$ ,  $F_{\omega AC} = 0$  as well as  $\Delta\omega = 0$  and the feedback loop adjust the DC bias needed to nullify the mechanical frequency shift of the tip at  $\omega_{AC}$  and gives the final SP maps. To double-check if the feedback works properly, we check the maxima of the phase ( $\Delta\omega$  with PLL) versus the  $V_{DC}$  curve, which has the same value as the CPD from KPFM (Figure 3.8).  $F_{2\omega AC}$  can be also extracted and used for capacitive force microscopy. To avoid electronic interaction between tip and sample that may modify the surface potential, we employed the so called “retrace mode” (also named lift mode in some other AFM) when needed. In this mode, the tip scans each line two times: first time measuring the topography in the usual way and a second time measuring only CPD from a larger tip-sample distance. This is also used to double-check if the measured CPD is correct.







levels in the material can interact with the material. Elastically emitted EM wave has a dependence in space-time (Figure 3.10a). Depending on the distance between the adjacent atoms/molecules, the scattered light produces diffraction patterns due to interference of light, as shown in Figure 3.10. Hence a material with a periodic lattice produces a well-defined diffraction pattern which gives information about the structure of the lattice. Lattice planes are denoted by miller indexes (hkl). The periodicity of the lattice,  $d_{hkl}$  can be estimated from the angle of diffraction,  $\theta$  and the wavelength of the incident light,  $\lambda$  by Bragg's law, which states as

$$n\lambda = 2d_{hkl} \sin \theta \quad (\text{eqn 3.9})$$

and  $n$  is the order of diffraction peak.

The orientation of the lattice planes can be estimated from the diffraction features. A parameter defined as a scattering vector,  $\bar{q}_{hkl}$  is the difference between the incident wave vector,  $\bar{k}_i$  ( $|\bar{k}_i| = \frac{2\pi}{\lambda}$ ) and the diffracted wave vector,  $\bar{k}_f$  ( $|\bar{k}_f| = \frac{2\pi}{\lambda}$ ), i.e.

$$\bar{q}_{hkl} = \bar{k}_f - \bar{k}_i = 2 \left| \bar{k}_i \right| \sin \theta = 2 \frac{2\pi}{\lambda} \sin \theta \quad (\text{eqn 3.10})$$

Hence, the inter-planar distance,  $d$  can be written in terms of the scattering vector,  $\bar{q}$  (Figure 3.11).

$$q_{hkl} = \frac{2\pi}{d_{hkl}} \quad (\text{eqn 3.11})$$

When the scattering vector,  $\bar{q}$  is perpendicular to the substrate, the diffracted pattern refers to the out-of-plane periodicity of the lattice. When the scattering vector is on the sample plane, diffracting planes are perpendicular to the sample plane. The work in this thesis is done in these two geometries and explained in the next section.

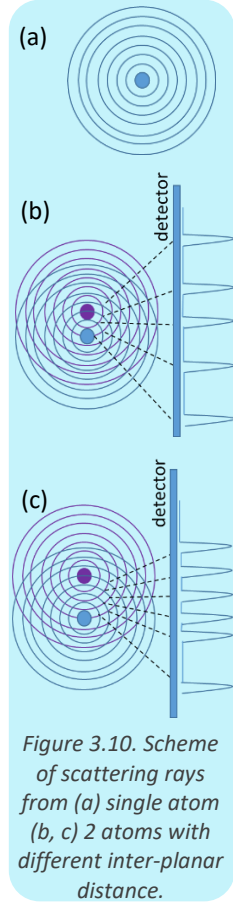
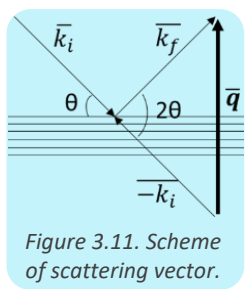


Figure 3.10. Scheme of scattering rays from (a) single atom (b, c) 2 atoms with different inter-planar distance.

### 3.6.1. Out-of-plane diffraction



In, out-of-plane (OOP) diffraction geometry, the incident angle is equal to the diffracted angle and is called specular or  $\theta - 2\theta$  geometry. During the scan, the incident angle and the detection angle vary simultaneously from 0 to  $\theta$ . For this thesis, we measured the samples in different synchrotrons with different measurement setups and with different wavelengths of X-rays. Hence, we present all the data in  $q$ -space. The OOP XRD data for  $q_z < 0.2 \text{ \AA}^{-1}$  is called X-ray Reflectivity (XRR) and this region gives more information about the thickness and roughness of the film. Figure 3.12 shows the main information one can get from the OOP diffraction pattern.

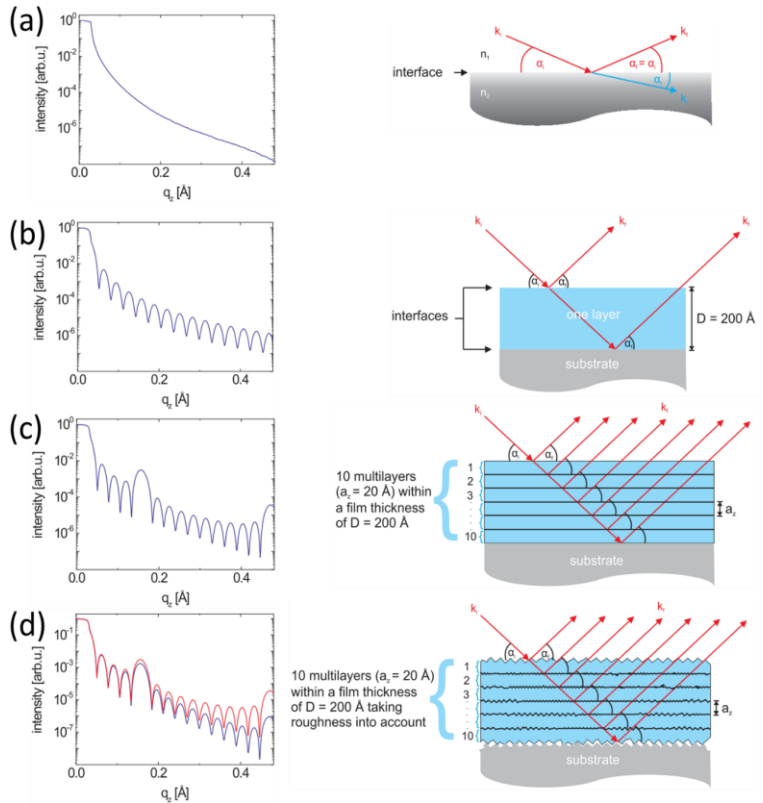


Figure 3.12a shows the case where you have only one interface in the material. The roughness of the substrates can be checked by the x-ray reflectivity of the sample. A uniform (Figure 3.12b) sample with two interfaces produces an interference pattern of periodic fringes superposed to the reflected intensity. These fringes are called Kiessig oscillations and their period ( $\Delta q$ ) is inversely proportional to the thickness of the film, i.e.,  $t = \frac{2\pi}{\Delta q}$ . If the film is rough, their amplitude will diminish, hence can give quantitative information about the smoothness of the film. As shown in Figure 3.12c, the periodic structure within the film gives Bragg peaks. The width (Full width at half maximum, FWHM) of the Bragg peaks can give information about the coherence length of the film as described by coherence length,  $L_c \sim \frac{2\pi}{\text{FWHM}}$ . The amount of vertical periodic structures/lattice planes inside the film is finite and can give interference patterns around the Bragg peaks, and these oscillations are called Laue oscillations. If a film contains domains with a different number of lattice planes, it leads to incoherent superposition and weakens the Laue oscillations, hence can give qualitative information about the amount of coherently ordered domains giving Bragg peaks. The width of Laue oscillations ( $\Delta q_L$ ) gives the corresponding domain size,  $t_{\text{domain}} = \frac{2\pi}{\Delta q_L}$ .

### 3.6.2. Grazing Incidence X-ray diffraction (GIXD)

In GIXD also known as Grazing Incidence X-ray scattering (GIXS), the incident angle is set below the critical angle of the sample,  $\theta_c$ . The critical angle is the incident angle at which total external reflection occurs and is proportional to the refractive index of the material. Neglecting absorption,  $\theta_c$  for small angles (Taylor approximation) is given by,

$$\theta_c = \sqrt{2\delta}, \text{ where} \quad (\text{eqn 3.12})$$

$$\delta = \frac{r_e}{2\pi} \lambda^2 \rho_e \quad (\text{eqn 3.13})$$

Where  $r_e = 2.813 \cdot 10^{-6} \text{nm}$ , is the classical radius of the electron,  $\rho_e$  is the electron density and  $\lambda$  is the X-ray wavelength.<sup>[105]</sup> Near the critical angle, the incident X-ray penetrates only a few nanometers (depending on the electronic density in the material) from the surface but illuminates a large area on the sample surface, making the technique surface sensitive.<sup>[9]</sup> In this geometry, the scattering vector is (nearly) parallel to the sample surface ( $q_{xy}$ ) and gives in-plane diffraction patterns. Two types of detectors are widely

used: point detectors and 2D detectors (Figure 3.13). A point detector moves at an angle,  $\delta$ , across the line of incidence.  $\delta$  scans obtained from the point detector, for a range of vertical angles  $\gamma$ , tailored to give 2D-GIXD maps, show the diffraction pattern for different scattering vector directions. While a 2D detector takes images of the diffraction pattern and later convert into 2D maps in  $q$  space using the reference distance between the sample and the detector. The orientation of different lattice planes in the sample can be deduced from the 2D-GIXD maps. Depending on the range of  $\delta$  or  $q_{xy}$ , there are two types of GIXD measurements to probe different range of periodicities: wide angle X-ray scattering (WAXS) and small angle X-ray scattering (SAXS).

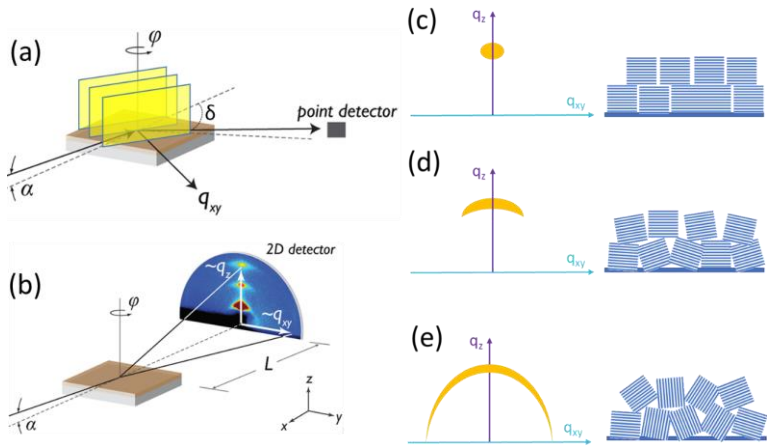


Figure 3.13. Scheme of a GIXD measurement setup (a) with a point detector (b) with a 2D detector. In the right panels, three main types of diffraction patterns and their corresponding thin-film structure: (c) highly oriented crystallites, (d) less oriented crystallites and (e) fully randomly oriented crystallites. Adapted from ref [9]

The former scans a larger range of  $q_{xy}$  and gives information about smaller periodicities in the sample while the latter probes smaller  $q_{xy}$  and provides data of larger periodicities up to a few hundreds of nanometers. The geometry for the measurement is the same for both cases and the main difference is in the sample-detector distance. As shown in Figure 3.13, a qualitative understanding of the crystalline orientations of thin films can be acquired from the GIXD patterns. Textured film: highly oriented and isotropic in-plane structures give a bright spot like diffraction pattern whereas the crystallite with vertical orientation gives an arc. And randomly oriented crystallites give a ring-like diffraction pattern, known as Debye-Scherrer rings.

### 3.6.3. Synchrotron Measurements

When electrons accelerate at high speed, they emit X-rays and synchrotron facilities (cyclic particle accelerators) are the sources of all types of EM waves including high and low-energy X-rays. The radiation obtained from synchrotrons is usually called synchrotron light (also called magneto-bremsstrahlung radiation) which has high brilliance, stability, and flux. Also has a broad spectrum and the users can choose the wavelength required. Hence, different high resolution probing techniques use synchrotron light. The work presented in this thesis has been done in three different synchrotron facilities and four beamlines: SpLine beamline (BM25 at ESRF, Grenoble, France), ID03 beamline (at ESRF, Grenoble, France), SIXS (at Soleil, Paris, France) and BL11 - NCD-SWEET beamline (at ALBA, Barcelona, Spain).

X-ray diffraction studies of asymmetric BTBT-C8 and symmetric C8-BTBT were conducted on the six-circle diffractometer at the SpLine beamline (BM25 Beamline at ESRF, Grenoble, France) with  $\lambda = 1.2\text{\AA}$ . The design and details of the beamline measurement setup are available online.<sup>[106],[107]</sup> The XRD measurements were performed on in-situ grown films under ultra-high vacuum (UHV) conditions. The experiments were performed in a portable UHV-compatible chamber mounted in a vertical geometry on the six-circle multipurpose diffractometer.<sup>[108]</sup> I would like to thank Dr. Maria Vila for the support during the experiments at the BM25 beamline at ESRF.

X-ray diffraction measurements of DPh-BTBT molecules were conducted at the ID03 beamline of the European Synchrotron Radiation Facility (ESRF, Grenoble, France). Out-of-plane and grazing incidence geometries were used to investigate the film structure in the direction perpendicular (out-of-plane) and parallel (in-plane) to the substrate, respectively. A 2D Maxipix 2x2 detector was used for x-ray scattering measurements. The x-ray wavelength was 0.99 Å. For GIXD experiments an incident angle of 0.11° was set, which is below the critical angle of Si (~0.14° at this energy). The 2D GIXD maps were built up and analysed by BiNocular software. I would like to thank Dr. Linus Pithan and Paul Bayer for their support during the experiments at the ID03 beamline at ESRF.

X-ray diffraction studies of C8-BTBT with F6TCNNQ molecules were conducted at the SIXS beamline at Soleil, Paris, France, with  $\lambda = 0.6727\text{\AA}$ . Both molecules were evaporated and annealed in situ under a high vacuum. The detector used was an XPAD S140. It is a hybrid pixel detector of 560x240 pixels with a pixel size of 130x130µm<sup>2</sup>, therefore having an active area of 75x32mm<sup>2</sup>. The typical sample-detector distance is 1.15m. 2D GIXD maps were analysed by BiNocular software. I would like to thank Dr. Alina Vlad and

Dr. Andrea Resta for their support during the experiments at the SIXS beamline at Soleil.

X-ray diffraction studies of C8-BTBT co-crystals from solutions and co-evaporation were conducted at the BL11-NCD-SWEET beamline at ALBA synchrotron, Barcelona, Spain, with an energy of 12.4keV (Figure 3.14a).

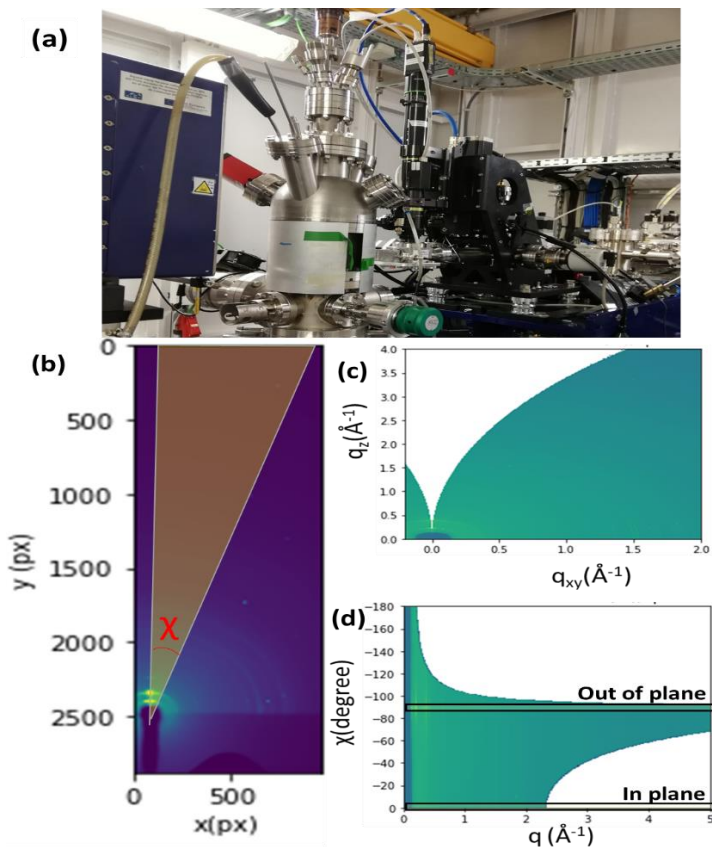


Figure 3.14. (a) Photo of the measurement set up in BL11-NCD-SWEET beamline at ALBA synchrotron (b) Image obtained from the 2D detector at ALBA. X and Y axis are in pixels. The data are processed by including the sample-detector distance and incident angle. (c) 2D reciprocal maps and (d) Data remapped as a function of azimuthal angle and scattering vector.

Some measurements conducted at ALBA were in ambient conditions and are specified in the respective chapters. The expected critical angle of the C8-BTBT is  $0.074^\circ$  and F6TCNNQ is  $0.172^\circ$ . Unlike the other beamlines mentioned

before, the detector in this beamline is a Rayonix LX 255-HS 2D detector of 960x2880 pixels with an area of 88.54 x 88.54  $\mu\text{m}^2$  for the binning employed with a beam stopper. The diffraction pattern is collected as a 2D image and converted into reciprocal space coordinates from the exit scattering angles calculated for each pixel (and the incident angle). A calibration sample is used to obtain the sample-detector distance and rotation angles of the detector. Figure 3.14 shows different 2D GIXD maps used in the analysis.  $q_z$  vs.  $q_{xy}$  map shows the reciprocal space of the sample. The azimuthal angle  $\chi$  vs.  $q$  map (Figure 3.14c) is used for quantitative analysis of the preferred crystallite orientation and crystallite coherence length. I would like to thank Dr. Eduardo Solano for the support during the experiments at the BL11-NCD-SWEET beamline at the ALBA synchrotron.

### 3.7. Photoelectron Spectroscopy

A photon with sufficient energy can excite and extract an electron from its atomic orbital to the vacuum level. The excess energy will be converted into the kinetic energy (KE) of the emitted electron. In other words, the difference in the energy of the incident photon and the KE of the emitted electrons give the binding energy (BE) of the corresponding electronic states in a particular chemical environment. This concept is employed in Photoelectron Spectroscopy (Figure 3.15). Each element has different electronic levels/orbitals with their characteristic BE, the minimum energy required to remove an electron from the specific orbital to the vacuum level, which are the fingerprints of the chemical bonds between atoms. As commented, the KE of the emitted electron is the difference between the energy of the photon ( $h\nu$ ) and the BE of the electron's orbital, i.e.

$$KE = h\nu - BE \quad (\text{eqn 3.14})$$

where  $h$  is the Planck's constant and  $\nu$  is the frequency of the EM wave. It is clear that the BE of an orbital depends on the surrounding chemical environment and chemical changes like charge transfer, new chemical bonds, or dipole formation in the surroundings. To probe orbitals with large BE (core levels), X-rays are used and are called X-ray photoelectron spectroscopy (XPS). BE of the electrons from the core levels can be calculated from the KE of the emitted electrons using the eqn 3.14. Casa XPS software was used to



fit the XPS spectra to obtain core level shifts with a 30:70 Gaussian: Lorentzian ratio.

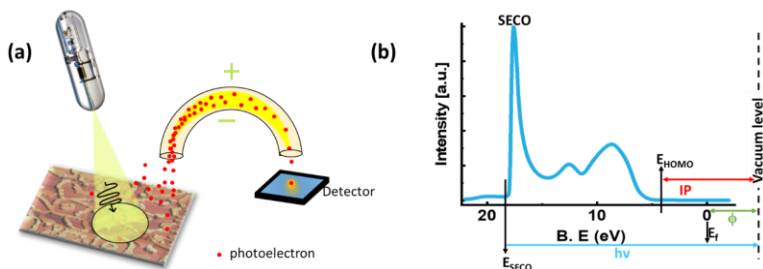


Figure 3.15. (a) Scheme of Photoelectron Spectroscopy (b) A representative spectroscopic curve from UPS measurement.

Because of the small BE, the density of states at the Fermi-edge valence band (VB) and the highest occupied molecular orbital (HOMO), UV rays are used in the so-called ultraviolet photoelectron spectroscopy (UPS). UV excited photoelectrons experience an inelastic scattering which generates secondary electrons before leaving the surface. These electrons appear as a polynomial background in the spectra. The energy at which this background ends abruptly is called the secondary electron cut off region ( $E_{SECO}$ ). Photoelectrons with the highest KE originate from the Fermi level for metals while, for an organic semiconductor, they are from the HOMO. Hence the region at the lowest BE electrons from the material appears ( $E_{HOMO}$ ) gives the value of HOMO. Both SECO and HOMO were estimated from the intersection of the corresponding fitted linear curve with the background (Figure 3.16). The sample is in contact with the spectrometer, and therefore the Fermi level is equalized, hence is obtained the zero of the UPS spectra. The spectrometer is calibrated using the Fermi energy of a gold sample for the measurements reported in this thesis. UPS is a surface-sensitive measurement which probes a few nanometers of the surface. As illustrated in Figure 3.15, the HOMO of the molecules on the surface as well as the work function ( $\phi$ ) and ionization potential (IP) can be estimated from the spectrum.

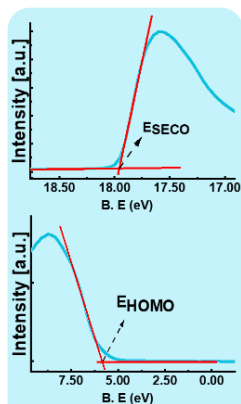


Figure 3.16. Illustration of how  $E_{SECO}$  and  $E_{HOMO}$  are determined.

$$\text{The work function of the surface, } \phi = h\nu - E_{SECO} \quad (\text{eqn 3.15})$$

The ionization potential of the surface,

$$IP = h\nu - (E_{SECO} - E_{HOMO}) \quad (\text{eqn 3.16})$$

Precautions were made to reduce surface contaminants by preparing the samples and measuring them under ultra-high vacuum (UHV).

Photoelectron spectroscopy measurements were done at the Institut Català de Nanociència i Nanotecnologia (ICN2) and at Institut für Angewandte Photophysik Fachrichtung Physik (IAPP). In the ICN2, a monochromatic X-ray source with Al K $\alpha$ ,  $h\nu = 1486.6\text{eV}$  and a monochromatic He I- $\alpha$  line source with  $h\nu = 21.21\text{eV}$  were used for XPS and UPS, respectively. The detector used was a Specs Phoibos 150 hemispherical energy analyser. In IAPP, soft x-ray source XR50 by Specs, equipped with a twin anode made from aluminium and magnesium which can be used separately for the excitation was used. The corresponding energy for Al K $\alpha_{1/2}$  is  $1486.61\text{eV}$  and for Mg K $\alpha_{1/2}$  is  $1253.64\text{eV}$ . The UV source used was a helium discharge lamp (UVS10/35, Specs) with the main He I excitation line at  $21.22\text{eV}$ . Phoibos 100 hemispherical analyser was used as the detector system in the so-called fixed analyzer transmission mode. To have access to the work function of the samples from the SECO signal, the corresponding spectra were taken with the samples biased at  $-10\text{V}$  at ICN2 and  $-8\text{V}$  at IAPP. An Au (111) single crystal was used as the reference for the determination of the Fermi energy. Both XPS and UPS were measured under UHV for samples fabricated in-situ using the native SiO $_2$ /Si as substrate.

### 3.8. UV-vis absorption

When a material is irradiated with an electromagnetic wave of energy equal to the energy difference between the electronic orbitals of the material, absorption occurs. An electronic transition takes place when an electron in the ground state orbital absorbs the incoming light and is excited to a higher energy orbital: this is the fundamental phenomenon exploited in absorption spectroscopy.

UV-vis absorption spectroscopy performed during this thesis was measured by a Cary-5000 Scan (Varian) UV-Vis-NIR spectrophotometer. A baseline spectrum is recorded with respect to air and is subtracted from the spectra before further analysis. The substrate used for the measurement was glass. Organic semiconductor molecules were thermally evaporated on top of the glass substrate under a vacuum (commonly as twin samples of those grown on SiO $_2$  employed for structural characterization by XRD or AFM).

### 3.9. OFET fabrication and characterization

A transistor is a three-terminal device designed to obtain a controlled current flow between two electrodes (source and drain), regulated by the voltage applied to a third electrode (gate). In an organic field-effect transistor (OFET), the semiconductor will be an organic material (organic semiconductor, OSC), either a polymer or a small molecule. An applied voltage at the gate creates an electric field across the dielectric which causes an accumulation of charges at the dielectric/semiconductor interface to nullify the field. These accumulated charges function as a conductive channel between the source and drain.

There are mainly, two distinct types of current-voltage characteristics for an OFET: output and transfer. During an output characteristic measurement, the drain current ( $I_{ds}$ ) is measured for a range of drain voltages ( $V_{ds}$ ) keeping the gate voltage ( $V_g$ ) constant. In a transfer characteristic measurement, the drain current ( $I_{ds}$ ) is measured for a range of gate voltages ( $V_g$ ) keeping the drain voltage ( $V_{ds}$ ) constant. Depending on the value of  $V_{ds}$ , two regimes are defined: saturation and linear.

When,

$$|V_{ds}| > |V_g - V_{th}| > 0, I_{ds,sat} = \mu_{sat} \frac{WC_d}{2L} (V_g - V_{th})^2 \quad (\text{eqn 3.17})$$

the device is in the saturation regime and when,

$$|V_g - V_{th}| > |V_{ds}|, I_{ds,lin} = \mu_{lin} \frac{WC_d}{L} (V_g - V_{th}) v_{ds} - \frac{1}{2} V_{ds}^2 \quad (\text{eqn 3.18})$$

Then the device is in linear regime.  $L$  is the channel length;  $W$  is the channel width and  $C_d$  is the capacitance of the dielectric ( $3.46 \cdot 10^{-8} \text{F/cm}^2$  for 100nm  $\text{SiO}_2$  and  $4.646 \cdot 10^{-8} \text{F/cm}^2$  for 40nm CYTOP). OFET parameters discussed in this thesis are calculated as explained below.

$I_{on}$  is the maximum and  $I_{off}$  is the lowest drain current measured during transfer characteristics in a linear regime.  $V_{on}$  is the gate voltage at which the  $I_{ds}$  start to show an exponential increase from  $I_{off}$ . For each regime, the mobility can be extracted:

*Linear field effect mobility,*

$$\mu_{lin} = \frac{\frac{\partial(I_{ds})}{\partial V_g} L}{WC_d |V_{ds}|} \quad (\text{eqn 3.19})$$

*Saturation field effect mobility,*

$$\mu_{sat} = \frac{2L(\frac{\partial(\sqrt{I_{ds}})}{\partial V_g})^2}{WC_d} \quad (\text{eqn 3.20})$$

both measured at a constant  $V_{ds}$ .

Another important OFET parameter we used in this thesis is,

$$\text{Threshold voltage, } V_{th} = V_g - \frac{1}{2}V_{ds} \quad (\text{eqn 3.21})$$

$V_{th}$  is the minimum  $V_g$  needed to create a conductive channel in the OSC layer between the source and the drain. If the applied  $V_g$  is below the  $V_{th}$  of the OFET, then the device is turned off .

The substrates used are thermally grown  $\text{SiO}_2$  on Si wafers with a thickness of either 200nm or 100nm. The wafers were cleaned by rinsing with acetone and next with ethanol. Then dried with a nitrogen flux avoiding solvent stains on the substrate.

For bottom-gate bottom-contact devices (BG-BC), 50nm of gold were evaporated through a shadow mask. Then, these substrates were dipped in 1mM perfluorodecanethiol in ethanol for 30min, to optimize the OSC film growth. First, the OSC molecules were thermally evaporated on the substrates, then the dopant was deposited on top. For in-situ measurements, contacts were taken out using silver paste via a feed through in the vacuum deposition chamber and connected to the source meter.

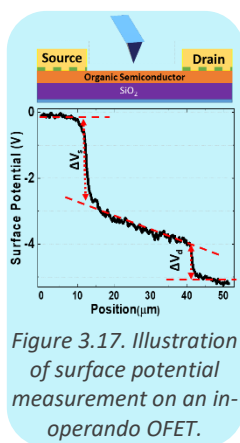
For bottom-gate top-contact devices (BG-TC), the OSC was thermally evaporated under a vacuum and the dopant was evaporated on top unless specified. Later, 50nm of gold were evaporated on the films that were exposed to ambient conditions while putting on the shadow mask. OFETs with dopant evaporated on top after gold deposition was also used for the studies as mentioned in the respective sections. Two diverse kinds of masks were used: first from OSSILA with 6 different channel lengths ( $L = 30\mu\text{m}, 40\mu\text{m}, 50\mu\text{m}, 60\mu\text{m}, 80\mu\text{m}$  and  $100\mu\text{m}$ ) and fixed channel width ( $W = 4\text{mm}$ ) and an in-house mask from IAPP with channel lengths ( $L = 80\mu\text{m}, 130\mu\text{m}, 180\mu\text{m}, 230\mu\text{m}$  and  $330\mu\text{m}$ ) and fixed channel width ( $W = 2\text{mm}$ ).

The electrical characterization of BG-TC OFETs was performed in ambient conditions using a semiconductor characterization system (SCS): Agilent

B1500A semiconductor device analyser connected to the samples with a Karl Suss probe station. Sweepme program was used for the measurement. The BG-BC in-situ OFET measurements were performed with two 2450 Keithley source-meters with the Kickstart program. I would like to thank Dr. Ines Temiño and Jinghai Li and Dr. Carsten Habenicht for their support during the OFETs measurements.

### 3.10. KPFM in OFETs

KPFM data can be used to obtain contact resistance and channel mobility values in transistors.<sup>[73],[12],[109],[110]</sup> The contact resistance measurements using KPFM during the thesis were done with an AFM head from Nanotec Electrónica S.L and the two 2450 Keithley source meters. KPFM measurements were performed to monitor the surface potential within the OFET channel for various applied gate and drain voltages. In Figure 3.17, a line profile taken on the surface potential map measured by KPFM across the channel on an OFET operated at a non-zero drain-source voltage and gate voltage (applied by the Keithley source meter) provides the voltage drop across the surface. The voltage drop ( $\Delta V$ ) at the source ( $\Delta V_s$ ) and drain ( $\Delta V_d$ ) contacts are measured from the surface potential profile. The source-drain current ( $I_{ds}$ ) is simultaneously measured by the Keithley. The ratio between the  $\Delta V$  at each electrode and  $I_{ds}$  gives the respective contact resistance ( $R_c = \Delta V/I_{ds}$ ). It is observed that there is a difference between the potential measured with KPFM and the applied source-drain potential due to a difference in work function between the electrode material and the tip.<sup>[111]</sup> In addition, rescaling of SP profiles has been reported to obtain the applied  $\Delta V$ .<sup>[111],[112],[113]</sup> During the thesis, we follow this procedure for the estimation of contact resistance.





## 4. Contact doping of C8-BTBT OFETs with C<sub>60</sub>F<sub>48</sub>

This chapter presents the structural study of the interface between C8-BTBT and C<sub>60</sub>F<sub>48</sub> and the electrical doping mechanism in the system. The content of this chapter is adapted from the *ACS Appl. Mater. Interfaces*, 2020, 12, 25, 28416– 28425; Copyright 2020 American Chemical Society.<sup>[32]</sup> Figures and parts of the text were reprinted with permission.

The investigation was conducted by employing the C8-BTBT molecule as OSC and C<sub>60</sub>F<sub>48</sub> as the dopant. Section 2.2.1 explains in detail why C8-BTBT is a suitable candidate for OFETs fabrication. The low-lying HOMO of C8-BTBT (5.4eV) permits the OFETs to work in ambient conditions,<sup>[114]</sup> but it also causes a barrier for charge carrier injection at the Au/C8-BTBT interface (work function of Au is 5.1eV), which contributes to an increase in contact resistance.<sup>[25],[24]</sup> Contact doping, i.e., incorporation of a thin layer of dopant at the contact/OSC interface, is an important strategy for reducing contact resistance.<sup>[54],[12],[74],[77]</sup> For the most commonly used p-type small molecular dopant, F4TCNQ, it has been reported that the deposited dopant diffuses through the OSC layer, affecting the thin-film structure hence resulting in a worsened device performance.<sup>[44],[55],[57],[56]</sup> C<sub>60</sub>F<sub>48</sub>, was chosen here to dope C8-BTBT films as this molecule has a deeper LUMO (5.5eV) level than the HOMO of C8-BTBT (see section 2.2.1).<sup>[60]</sup> In addition, the bulkier shape of the C<sub>60</sub>F<sub>48</sub> molecule prevents diffusion and film disruption. This is an add-on advantage for efficient contact doping without compromising the structural order of the C8-BTBT film. The objective of this chapter is to provide a

microscopic view of the interfacial properties by sequential deposition of C<sub>60</sub>F<sub>48</sub> on C8-BTBT films.

## 4.1. Structure and morphology

First, the morphology and the structure of pristine C8-BTBT films on native oxide/Si substrates are presented. In-situ XRD measurements were performed right after the growth in UHV at the SPLINE beamline at ESRF while ex-situ AFM measurements were performed a few days after the growth. Figure 4.1 shows the morphology and out-of-plane XRD pattern of a C8-BTBT thin film, which reveals a crystalline multi-layered structure.

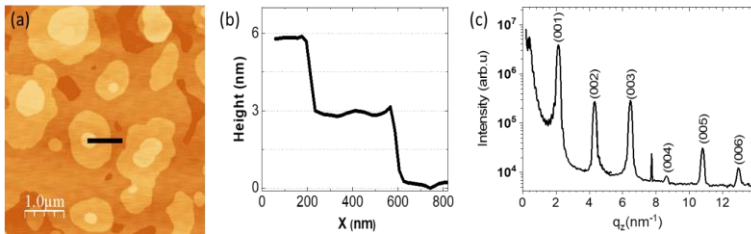


Figure 4.1. (a) Topographic AFM image and (b) height profile along the segment in (a) for a 27nm thick C8-BTBT film (nominal thickness). (c) Out-of-plane XRD for a 48nm thick C8-BTBT film. The spike at  $q_z = 7.8 \text{ nm}^{-1}$  is not a structural feature of the samples.

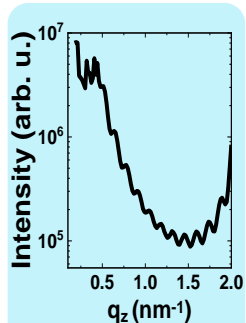


Figure 4.2. Kiessig fringes which indicate that the thickness of the film is 48nm.

The height measured by AFM for each individual layer is 3nm (Figure 4.1a, b) coinciding with the length of a C8-BTBT molecule and the reported standing-up orientation of the molecule on SiO<sub>2</sub> substrates.<sup>[115],[116]</sup> The Bragg peak positions in the OOP XRD data (Figure 4.1c) correspond to an interlayer spacing of 2.91nm, consistent with the AFM results. Bragg peaks up to the sixth orders of diffraction are visible, which is the manifestation of a (001) oriented film with a well-ordered and layered structure. The observed Kiessig fringes (Figure 4.2) and Laue oscillations indicate the smoothness and the coherent order of the film. To study the dopant/OSC interfacial structure, C<sub>60</sub>F<sub>48</sub> molecules were thermally evaporated on top of the C8-BTBT thin film. For contact doping, lower coverages of dopants are used.<sup>[74],[117]</sup> Figure 4.3a,b shows representative topographic and lateral force images obtained for a coverage of  $\sim 2 \text{ nm}$  C<sub>60</sub>F<sub>48</sub>. Lateral force images give a contrast between surface areas consisting of different materials,<sup>[118]</sup> here, between C<sub>60</sub>F<sub>48</sub> and C8-BTBT. Thus, C<sub>60</sub>F<sub>48</sub> can be distinguished by a lighter colour (i.e., higher friction) from the surrounding OSC surface in Figure 4.3c. By direct

comparison with the corresponding topography, it can be seen that the  $C_{60}F_{48}$  molecules form flat islands, most of them decorating the step edges of the C8-BTBT film. The heights of the  $C_{60}F_{48}$  islands range between 5nm and 12nm. A profile across one hexagonal  $C_{60}F_{48}$  crystallite is shown in Figure 4.3a. Since the size of the  $C_{60}F_{48}$  molecule is  $\sim 1$ nm, these crystallites consist of 5 -12 individual layers. The formation of flat hexagonal assemblies supports the reported crystalline FCC structure of  $C_{60}F_{48}$ .<sup>[62],[119]</sup> The island growth of  $C_{60}F_{48}$  on C8-BTBT follows the so-called Volmer-Weber mode suggesting a weak interaction of the  $C_{60}F_{48}$  molecules with the alkyl-terminated OSC surface. Statistical analysis performed on AFM images confirms that the  $C_{60}F_{48}$  islands decorating the steps are located on the inferior terraces. This fact is probably due to a stronger interaction between the  $C_{60}F_{48}$  molecules and the aromatic core of the BTBT molecules (exposed at the step edges) than with the alkyl chains (exposed at the terrace surface).

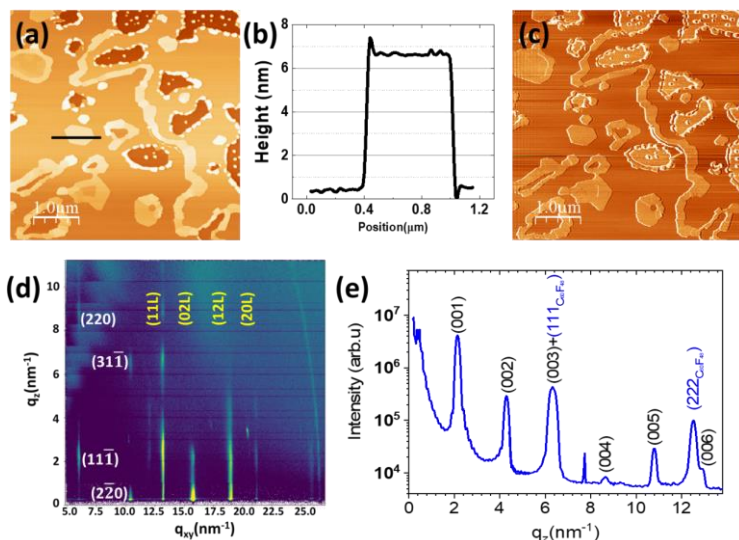


Figure 4.3. (a) Topography of a film with 2nm of  $C_{60}F_{48}$  on a 9nm thick C8-BTBT film. (b) The height profile along the black segment in (a). (c) Corresponding lateral force image (forward). (d) 2D GIXD map of 9nm of  $C_{60}F_{48}$  on a 9nm thick C8-BTBT film and (e) the out-of-plane XRD for 15nm of  $C_{60}F_{48}$  on a 48nm thick C8-BTBT film.

The lower level (darker regions) in the topography corresponds to the uncovered  $SiO_2$  substrate, where  $C_{60}F_{48}$  grows in the form of small, isolated aggregates. Figure 4.3d displays the 2D GIXD patterns of a C8-BTBT film with



a larger coverage of C<sub>60</sub>F<sub>48</sub> deposited on top. Diffraction intensities corresponding to (11L), (02L), (12L) and (20L) planes of the C8-BTBT thin-film structure are observed at  $q_{xy} \sim 13.1\text{nm}^{-1}$ ,  $q_{xy} \sim 15.7\text{nm}^{-1}$ ,  $q_{xy} \sim 18.8\text{nm}^{-1}$  and  $q_{xy} \sim 20.94\text{nm}^{-1}$ , respectively. These peaks have been already reported for the C8-BTBT thin film structure and assigned to the herringbone packing of the BTBT cores.<sup>[120],[29]</sup> The obtained in-plane lattice parameters of the unit cell are  $a = 5.95\text{\AA}$  and  $b = 8.03\text{\AA}$ . Additional diffraction features from C<sub>60</sub>F<sub>48</sub> at  $q_{xy} \sim 5.99\text{nm}^{-1}$ ,  $q_{xy} \sim 10.39\text{nm}^{-1}$  and  $q_{xy} \sim 11.90\text{nm}^{-1}$  are observed. Instead of rods, the C<sub>60</sub>F<sub>48</sub> features are spindle-like spots indicating a certain degree of 3D crystallinity.

Figure 4.3e shows the out-of-plane XRD data of C8-BTBT films upon deposition of 15nm C<sub>60</sub>F<sub>48</sub>, a larger dopant coverage. The Bragg peaks from C8-BTBT remain the same, demonstrating that C<sub>60</sub>F<sub>48</sub> does not alter the structure of the underlying OSC film. The emergence of two new Bragg peaks after C<sub>60</sub>F<sub>48</sub> deposition at  $q_z = 6.27\text{nm}^{-1}$  and  $q_z = 12.52\text{nm}^{-1}$  is observed. These peaks are in agreement with the reported FCC crystal structure of C<sub>60</sub>F<sub>48</sub> and correspond to the (111) and (222) Bragg peaks, indicating that the (111) crystal plane is parallel to the substrate.<sup>[62]</sup> The inter-plane spacing corresponding to  $q_z = 6.27\text{nm}^{-1}$  is 1nm ( $d_{111}$ ). The estimated mean crystalline size of C<sub>60</sub>F<sub>48</sub> islands from the full width half maximum (FWHM) of the (222) peak is 27nm. Importantly, the position and width of the BTBT peaks remain unaltered before (Figure 4.1c) and after dopant deposition (Figure 4.3e) establishing that the C<sub>60</sub>F<sub>48</sub> deposition does not disrupt the structure and packing of the underlying OSC films.

Hence, the deposition of C<sub>60</sub>F<sub>48</sub> molecules on C8-BTBT results in close-packed 3D crystallites decorating the C8-BTBT step edges, forming an abrupt and well-defined dopant/OSC interface, without dopant intercalation or any modification of the C8-BTBT packing.

## 4.2. Evaluation of contact doping in OFETs

In the (001) oriented C8-BTBT films, the conjugated BTBT core and the C<sub>60</sub>F<sub>48</sub> are separated by the alkyl chains. This implies no direct overlap between the dopant electronic states and the  $\pi$ -conjugated core of the C8-BTBT. However, charge transfer between the HOMO of C8-BTBT and the LUMO of C<sub>60</sub>F<sub>48</sub> may occur across the alkyl chains by electron tunnelling. To confirm the occurrence of doping, it is important to show that the incorporation of the dopant improves one or more device parameters. As reported in previous

studies and commented in section 2.6, contact doping can reduce the contact resistance of OFETs.<sup>[24],[25],[74],[44],[27],[117],[121]</sup> In the present case, the morphology reveals a discontinuous layer of  $C_{60}F_{48}$  on the C8-BTBT surface. This is certainly not the optimal nanoscale morphology to improve charge injection between the metal/OSC interface when the metal contact is deposited on top. The effect of contact doping by  $C_{60}F_{48}$  for C8-BTBT OFETs was evaluated by employing a BG-TC device architecture, with channel lengths between  $30\mu m$  and  $100\mu m$ .

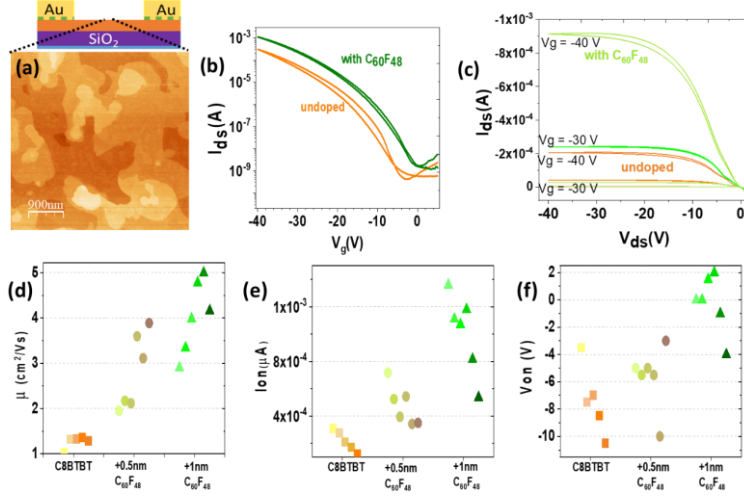


Figure 4.4. (a) BG-TC schematics and AFM topography in the OFET channel (b) transfer and (c) output curves for C8-BTBT OFETs (25nm) with  $C_{60}F_{48}$  (1nm) deposited under the contacts ( $V_{ds} = -5V$ ,  $V_g = 0V, -10V, -20V, -30V$  and  $-40V$  and  $L = 40\mu m$ ). (d) Saturation field-effect mobility, (e)  $I_{on}$  and (f)  $V_{on}$  for C8-BTBT (25nm) OFETs with two different coverages of  $C_{60}F_{48}$  under the contact. Values measured for different channel lengths,  $L = 30\mu m, 40\mu m, 50\mu m, 60\mu m, 80\mu m$  and  $100\mu m$  (represented by the darker colour gradient for larger channels), are shown. Orange squares correspond to bare C8-BTBT, while light green circles and dark green triangles to the C8-BTBT films after deposition 0.5nm and 1nm  $C_{60}F_{48}$ , respectively.

Using a shadow mask, first the  $C_{60}F_{48}$  and then the gold for drain and source contacts were deposited on top of 25nm thick C8-BTBT films grown on 200nm SiO<sub>2</sub> substrates. Two dopant coverages of 0.5nm and 1nm were used for these studies. Figure 4.4a shows the channel topography, consisting of flat C8-BTBT terraces. Figure 4.4b,c shows the transfer and output curves obtained for the undoped reference device (orange line) and device with 1nm of  $C_{60}F_{48}$  (green

lines) deposited under the gold electrodes. Although the devices show a non-ideal behaviour, contact doping is manifested through an increase of the current by one order of magnitude and a shift of the turn-on voltage ( $V_{on}$ ) towards positive values. Panels in Figure 4.4d, e and f show the increase in the saturation mobility ( $\mu$ ),  $I_{on}$ , and  $V_{on}$ , respectively, for several devices as the amount of dopant increases. For the device corresponding to Figure 4.4a and b ( $L = 40\mu\text{m}$ ), the field-effect mobility extracted from the transfer characteristics in the saturation regime increased from  $1.03\text{cm}^2/\text{Vs}$  (in the reference device) to  $3.34\text{cm}^2/\text{Vs}$ . The best value measured for contact-doped devices is  $5.00\text{cm}^2/\text{Vs}$ . These observations suggest a reduced contact resistance due to doping.

To extract the contact resistance, the potential drop across the electrode/channel interface in the OFET was measured by KPFM in operation conditions. Figure 4.5a, b show the SP line profiles and the SP maps measured on a bare C8-BTBT OFET operated at  $V_{ds} = -5\text{V}$  for  $V_g = -10\text{V}$  to  $-40\text{V}$ .

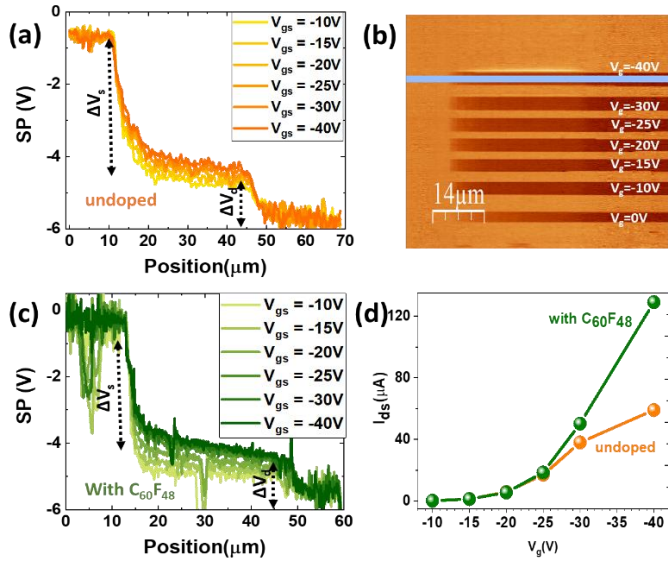


Figure 4.5. (a) Surface potential profiles were obtained as shown by the blue segment in (b) which is the surface potential recorded by KPFM on an  $L = 40\mu\text{m}$  channel C8-BTBT OFET during the application of  $V_{ds} = -5\text{V}$  and the different  $V_g$  indicated in the legend. The orange colour in (b) indicates that the device was switched off ( $V_{ds} = 0\text{V}$ ) between the indicated  $V_g$  (c) Surface potential profiles obtained from the SP for the C8-BTBT OFET with  $1\text{nm}$  thick  $\text{C}_{60}\text{F}_{48}$  under the contacts, during the operation at  $V_{ds} = -5\text{V}$  and the  $V_g$  as indicated in the legends. (d) Measured drain current corresponding to each line profile for doped (green) and undoped (orange) C8-BTBT OFETs.

Figure 4.5c shows the SP line profiles for contact doped OFETs with a C<sub>60</sub>F<sub>48</sub> coverage of 1nm. The voltage drop ( $\Delta V$ ) at the source ( $\Delta V_s$ ) and drain ( $\Delta V_d$ ) contacts can be quantified from the SP profiles while the source-drain current ( $I_{ds}$ ) is simultaneously measured. The ratio between the voltage drop at each electrode ( $\Delta V_{d,s}$ ) and  $I_{ds}$  gives the respective contact resistance ( $R_c(d, s) = \Delta V_{d,s} / I_{ds}$ ). Here the contact resistance has been normalized to the transistor width,  $W = 4\text{mm}$ . Even though the voltage drop in the doped and undoped devices did not show significant differences, the measured drain current for a  $V_g = -40\text{V}$  is more than twice for doped devices, which is an indicator of a significant reduction of contact resistance. The calculated contact resistance decreases with doping, from  $17.68\text{k}\Omega\cdot\text{cm}$  to  $12.24\text{k}\Omega\cdot\text{cm}$  and from  $8.88\text{k}\Omega\cdot\text{cm}$  to  $4.24\text{k}\Omega\cdot\text{cm}$  at source and drain, respectively. This reduction in  $R_c$  induces a lower barrier for charge injection and, therefore, an improvement at the metal/OSC interface which enhances the transport from the contacts to the channel.<sup>[122]</sup> As mentioned in section 2.5.2, possible mechanisms responsible for the reduction in contact resistance include a decrease in the depletion-layer thickness, the filling of trap states at the organic semiconductor near the electrode interface or a change in the work function (explained in detail in section 5.3). All these processes are related to electron charge transfer at the dopant/OSC interface.<sup>[24],[12],[123],[124]</sup> Even though the C<sub>60</sub>F<sub>48</sub> layer at the Au/C8-BTBT interface is discontinuous, it is locally modifying the work function of the surface at the contact region and reduces the contact resistance as well as improves the C8-BTBT OFET device performance.

### 4.3. Dopant-induced morphological stability of the OSC films

The tendency of OSC molecules to dewet from SiO<sub>2</sub>, reduces the long-term stability of organic electronic devices,<sup>[125],[34]</sup> especially C8-BTBT. A. Pérez-Rodríguez, *et al.*, demonstrated a strong dewetting of C8-BTBT thin films with time, resulting in the degradation of the fabricated OFETs.<sup>[27]</sup> In general, dewetting is more pronounced for thinner films (as will be demonstrated in section 5.1). Figure 4.6 shows the evolution of the topography of 30nm thick C8-BTBT films over 15 weeks. A similar thickness of C8-BTBT films is used in the fabrication of OFETs. Keeping the sample mounted on the AFM, the topography was measured every few days in the very same surface location. The images reveal that dewetting starts in some local spots, leaving exposed substrate regions which would be detrimental for device applications.

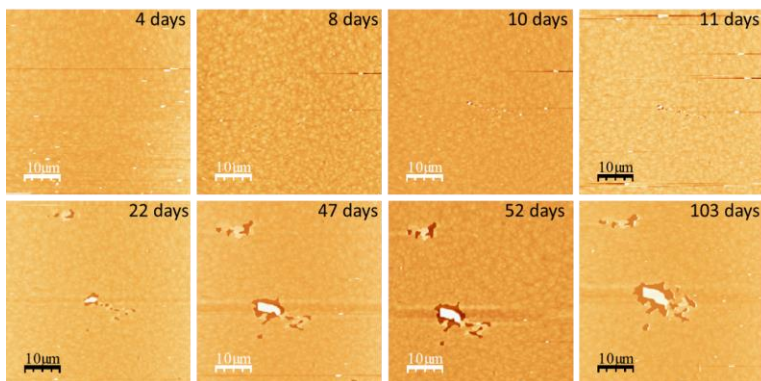


Figure 4.6. Topography of a 30nm thick C8-BTBT film, the consecutive images were taken in the very same area over 15 weeks.

The long-term stability of similar films upon deposition of  $C_{60}F_{48}$  has been studied. Figure 4.7a and b, show the topographic images of the same sample consisting of 2nm  $C_{60}F_{48}$  deposited on 13nm C8-BTBT films measured just as prepared (fresh) and one year later, respectively.

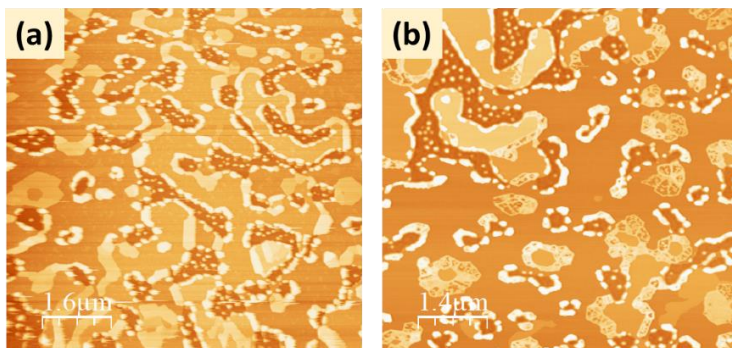


Figure 4.7. (a) AFM topography of a fresh 13nm thick C8-BTBT film with 4nm of  $C_{60}F_{48}$  deposited on top, (b) topography of the same sample measured one year later.

The quite similar morphology of the fresh and one-year-old sample confirms that C8-BTBT film dewetting is hindered by the presence of  $C_{60}F_{48}$  on the surface, which in turn enhances the stability of the  $C_{60}F_{48}$ /C8-BTBT film morphology. The dewetting process is known to be initiated by the retraction of molecules from step edges and their incorporation to higher levels.

Because  $C_{60}F_{48}$  is forming crystallites anchored at the terrace edges of the C8-BTBT film, the dewetting process is inhibited and therefore, the dopant stabilizes the film for a long time. This opens a possible application of  $C_{60}F_{48}$  deposition on the surface of OSC as a strategy to stabilize the morphology of thin layers like a capping or protective layer.

To verify if the strategy of using  $C_{60}F_{48}$  also enhances the thermal stability of the films, XRD was measured in-situ during thermal annealing. Figure 4.8a shows the out-of-plane diffraction of bare C8-BTBT films for different temperatures, performed at the ALBA synchrotron by GIXD with a 2D detector; out-of-plane profiles are obtained from the 2D images as explained in the experimental section 3.6.3. Figure 4.8b shows, for the same temperatures, the out-of-plane XRD data obtained for C8-BTBT films with  $C_{60}F_{48}$  on top (measured at ESRF synchrotron with a point detector). A maximum error of  $\sim 10^\circ\text{C}$  is possible due to a different measurement setup. C8-BTBT films with and without  $C_{60}F_{48}$  deposited on top were annealed above  $100^\circ\text{C}$ . The crystalline features of bare C8-BTBT film completely disappeared indicating that the whole film desorbs. In contrast, for the C8-BTBT film with  $C_{60}F_{48}$  on top, the crystalline Bragg peaks of C8-BTBT remain unchanged even after annealing at  $110^\circ\text{C}$  (Figure 4.8b). Yet, the (222) Bragg peak of  $C_{60}F_{48}$  started to decrease. The above XRD results confirm that the  $C_{60}F_{48}$  acts as a protecting layer and enhances the thermal robustness of C8-BTBT films.

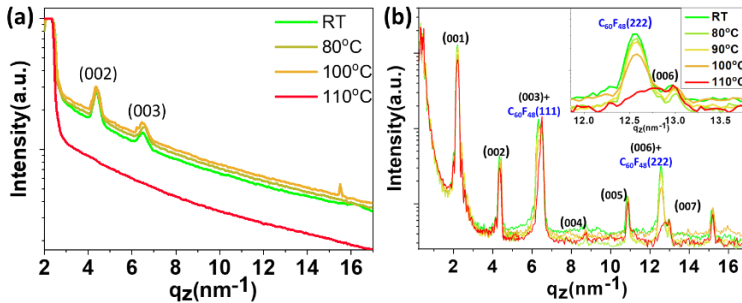


Figure 4.8. Out-of-plane XRD for (a) a bare 20nm thick C8-BTBT film and (b) a 50nm thick C8-BTBT film with  $C_{60}F_{48}$  on top, annealed at different temperatures (from RT to  $110^\circ\text{C}$ ). Inset in b is the  $C_{60}F_{48}$  peak at  $q_z = 12.52 \text{ nm}^{-1}$  which decreases with temperature while the characteristic Bragg peak of C8-BTBT at  $q_z = 12.95 \text{ nm}^{-1}$  remains unaltered.

As in the case of enhanced stability with time, the thermal stability of the films is attributed to the  $C_{60}F_{48}$ /C8-BTBT interfacial morphology, in which closed-packed  $C_{60}F_{48}$  crystallites nucleate at the C8-BTBT step edges. It is justifiable

to infer that these crystallites behave as pinning centres, hindering the structural changes or sublimation of the less bound C8-BTBT molecules located at the edges.

#### 4.4. Long-term stability of doped OFETs

To evaluate if the stabilizing effect of  $C_{60}F_{48}$  on C8-BTBT films enhances as well the OFET stability, the dopant molecule was deposited all over the entire surface of the C8-BTBT film, i.e., under the Au contacts (contact doping) as well as covering the whole channel region (channel doping). The schematics of the geometry employed and the channel morphology are shown in Figure 4.9a. The topographic image measured on the channel shows the discontinuous  $C_{60}F_{48}$  layer with the characteristic step decoration at C8-BTBT terrace edges. Figure 4.9b shows the transfer curves for pristine C8-BTBT OFET (undoped) and the OFET with  $C_{60}F_{48}$  deposited all over the C8-BTBT layer.

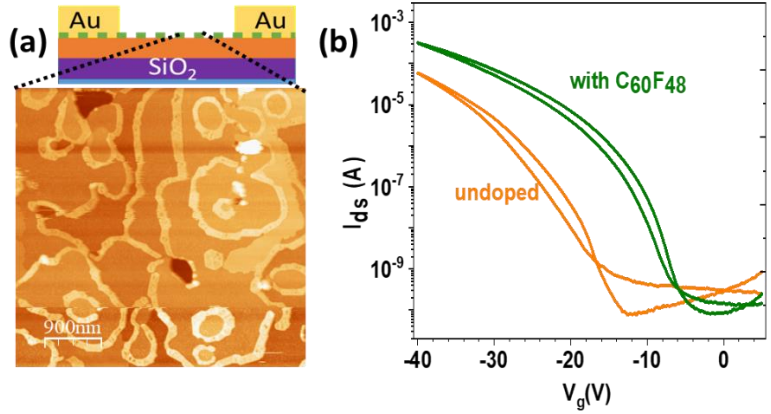


Figure 4.9. Topography of the channel and the transfer curve for C8-BTBT (25nm) OFETs with 1nm  $C_{60}F_{48}$  deposited under the contacts and at the channel region (green) with the reference device (orange). ( $V_{ds} = -5V$ ,  $L = 40\mu m$ ).

The OFET parameters obtained from the doped (all over the surface) devices show a similar trend as in the only contact doped OFETs described in Figure 4.4, i.e., the shift of  $V_{on}$  towards positive gate values, accompanied by an increase of  $I_{on}$ . In addition, the effective field-effect mobility (obtained in the

saturation regime) increased from  $1.14\text{cm}^2/\text{Vs}$  (in the reference device) to  $2.17\text{cm}^2/\text{Vs}$ . In accordance with the previous results shown for doped devices, the measured contact resistance per unit length decreases upon doping, from  $33.8\text{k}\Omega\text{-cm}$  to  $8.96\text{k}\Omega\text{-cm}$  and from  $14.4\text{k}\Omega\text{-cm}$  to  $3.44\text{k}\Omega\text{-cm}$  at source and drain, respectively.

It is noteworthy that the presence of  $\text{C}_{60}\text{F}_{48}$  over the channel does not cause any notable change in the  $I_{\text{on}}/I_{\text{off}}$  current ratio ( $\approx 10^5$ ), which implies that the channel conductivity is not modified. In other words, the electronic interaction of the dopant and the OSC at the interface does not cause an increase in free charges in the channel contrary to other reported systems.<sup>[74],[124]</sup> The effect of  $\text{C}_{60}\text{F}_{48}$  either only under the contact or both under the contact and on the channel is comparable. Interestingly, after one year of device storage in the air, the same OFETs were characterized. The obtained results are shown in Figure 4.10. The OFET with  $\text{C}_{60}\text{F}_{48}$  all over the C8-BTBT surface shows comparable mobility to the as-prepared devices. C8-BTBT OFET with dopant only under the contact shows a shift of  $V_{\text{on}}$  towards  $-30\text{V}$  after being exposed to air for one year. A shift that is opposed to the expected, for a hole-doped channel by  $\text{C}_{60}\text{F}_{48}$ .

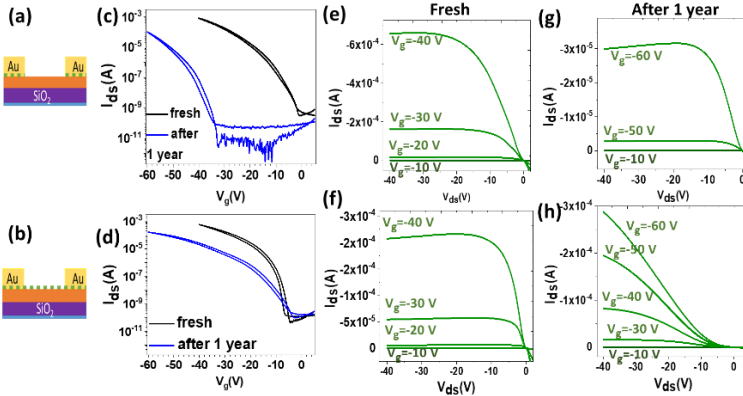


Figure 4.10. Scheme and transfer curves of as prepared doped OFETs (black curve) and after one year (blue line) ( $V_{\text{ds}} = -5\text{V}$ ), with  $1\text{nm}$  of  $\text{C}_{60}\text{F}_{48}$  deposited (a, c) only under the contacts and (b, d) all over C8-BTBT film surface (before depositing the contacts). The corresponding output curves between doped devices, as prepared (e, f) and after one year (g, h),  $L = 80\mu\text{m}$ .

There is no significant shift in  $V_{\text{on}}$  observed for the OFETs with  $\text{C}_{60}\text{F}_{48}$  all over the surface (Figure 4.10d). Although the underlying reasons are not verified experimentally, the shift in  $V_{\text{on}}$  can be attributed to the combination of



several effects due to the presence of  $C_{60}F_{48}$  on the surface. First, is the stable and continuous channel morphology without dewetting of the OSC layer. Second, the hydrophobicity of fluorinated fullerenes (due to the high fluorine content)<sup>[126],[127]</sup> makes the crystalline  $C_{60}F_{48}$  islands at step edges of C8-BTBT film act as a kinetic barrier that hinders the interlayer and/or inter-grain (through structural defects or grain boundaries) water penetration.<sup>[128]</sup> Moreover, a continuous, compact and stable OSC film (without voids due to dewetting) protects the dielectric/OSC interface. In addition, the off current in the transistors is not affected by ageing, indicating that the conductive channel remains undoped. This validates the long-term stability of  $C_{60}F_{48}$  doped C8-BTBT OFETs without interdiffusion of the dopant that would otherwise worsen the device performances.

In summary, the interfaces formed between C8-BTBT and the  $C_{60}F_{48}$  deposited on top have been studied.  $C_{60}F_{48}$  on C8-BTBT at RT results in the formation of close-packed and oriented crystallites anchored at the low part of the step edges of the OSC film surface. There is no incorporation by diffusion of  $C_{60}F_{48}$  molecules into the underlying C8-BTBT films, which thus preserves the crystallinity, even after annealing. The  $C_{60}F_{48}$ /C8-BTBT interface has a beneficial effect on the temporal and thermal stability of the films. Nucleation of  $C_{60}F_{48}$  at the C8-BTBT island edges inhibits upward mass transport and undesired film dewetting. In addition, it also reduces the sublimation of molecules providing the films with increased thermal robustness, an endurance effect similar to film encapsulation. Deposition of  $C_{60}F_{48}$  at the Au/C8-BTBT interface improves the charge injection in OFETs by reducing the contact resistance, which is reflected in an increase of the effective field-effect mobility and a lower  $V_{on}$  (with respect to control devices without  $C_{60}F_{48}$ ). It is concluded that doping the C8-BTBT surface with  $C_{60}F_{48}$  has the double beneficial effect of lowering the contact resistance and providing long-term and enhanced thermal stability of the C8-BTBT OFETs. The origin of these results is local work function modification along with a peculiar nanomorphology of the  $C_{60}F_{48}$ /C8-BTBT interface. The electrical stability of the OFETs in the air was confirmed after one year.



## 5. Effect of the Organic Semiconductor Side Groups

The focus of this chapter is the study of the electronic and structural properties of the interface formed between BTBT molecules with different side groups and the dopant  $C_{60}F_{48}$ . This chapter is adapted from the ACS Appl. Mater. Interfaces, 2020, 12, 25, 28416 – 28425.<sup>[32]</sup> and ACS Appl. Mater. Interfaces, 2020, 12, 51, 57578 – 57586.<sup>[129]</sup>; Copyright 2020 American Chemical Society. Figures and parts of the text were reprinted with permission.

In the previous chapter, we demonstrated the double beneficial effect of  $C_{60}F_{48}$  on C8-BTBT OFETs, more stability and lower contact resistance, which is attributed to the specific dopant/OSC interface. In order to understand how the structural and electronic characteristics of the dopant/OSC interface are affected by the physical-chemical properties of the OSC surface, in this chapter, we extend the investigation to other BTBT derivatives consisting of the same aromatic core but different side groups (octyl or phenyl group): asymmetric BTBT-C8, DPh-BTBT and C8-BTBT. The first section of this chapter is devoted to the interface formed between  $C_{60}F_{48}$  and the asymmetric BTBT-C8(octyl [1] Benzothieno[3,2-b][1] benzothiophene), with only one octyl termination. Then, we focus on two symmetric derivatives of BTBT, containing either two octyl or two phenyl groups. They are 2,7-dioctyl-BTBT (C8-BTBT) and 2,7-diphenyl-BTBT (DPh-BTBT). Films made out of one or the other symmetric molecules necessarily expose a different termination at their surface. However, because of the same BTBT core, both molecules are almost

similar in terms of the electronic structure, with a HOMO of  $\sim 5.39\text{eV}$  for C8-BTBT and  $\sim 5.41\text{eV}$  for DPh-BTBT, as reported.<sup>[5],[30],[37]</sup>

## 5.1. Interface formed between asymmetric BTBT-C8 and $\text{C}_{60}\text{F}_{48}$

The morphology of pristine asymmetric BTBT-C8 films on Si substrates consists of terraces separated by steps, in most cases with a height multiple of 4nm, though 2nm high steps were seldom found (Figure 5.1).

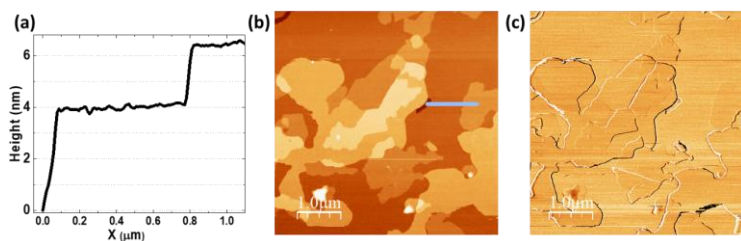


Figure 5.1. (a) Height profile of the line indicated in topography, (b) topographic image and (c) corresponding lateral force map of a pristine 16nm thick asymmetric BTBT-C8 film. All terraces, independently of the step height (one or two-layers high) have the same frictional contrast.

The length of the asymmetric BTBT-C8 molecule is  $\sim 2\text{nm}$  which indicates that the layered structure observed consists of a bilayer stacking (two molecules thick) in agreement with the reported crystal structure, in which each bilayer (lamellae) is formed by two head-to-head (or tail-to-tail) molecules.<sup>[115],[116]</sup> Due to the asymmetric structure of this molecule, it is impossible to ascertain whether the orientation of the bilayer structure is head-to-head or tail-to-tail from the topographic images. To investigate this, lateral force images, a sensitive tool to identify materials with a different chemical nature at the topmost surface, were employed.<sup>[27]</sup> As shown in Figure 5.1b and c, the topography and the lateral force image show no significant differences between single-layer and bilayer areas. Since the lateral force observed is similar to that of the symmetric C8-BTBT film, we conclude the surface consists of alkyl groups in asymmetric BTBT-C8 films. For a bilayer asymmetric BTBT-C8 stacking, an alkyl-terminated surface can only arise from a head-to-head assembly.

Out-of-plane XRD data (black curve) depicted in Figure 5.2a, show the (00L) Bragg peaks corresponding to the multilayer of asymmetric BTBT-C8. The derived interlayer spacing is  $\sim 4.12\text{nm}$  indicating the upright orientation of the molecules. However, the relative intensity of the Bragg peaks differs from the reported asymmetric BTBT-C8 structure by Gbadode *et al.*<sup>[115]</sup> In particular, the intensity ratio measured for (001):(002) = 20:27, (reported value is 20:1). The anomalous high intensity of the (002) Bragg peak can be explained by the presence of regions exhibiting the single-layer structure along with the bilayer structure, as observed in AFM (Figure 5.1a). After the deposition of 15nm  $\text{C}_{60}\text{F}_{48}$ , (blue curve in Figure 5.2 a), the Bragg peaks of BTBT-C8 remain unchanged, demonstrating that the dopant does not alter the underlying film. As in the case of C8-BTBT films, (section 4.1) two new Bragg peaks emerging at  $q_z = 6.2\text{nm}^{-1}$  and  $q_z = 12.52\text{nm}^{-1}$  are attributed to the (111) crystal plane of  $\text{C}_{60}\text{F}_{48}$  which agrees with the closed packed plane of the FCC structure parallel to the substrate. A representative topography and the corresponding lateral force image of an asymmetric BTBT-C8 film with 2nm  $\text{C}_{60}\text{F}_{48}$  on top are shown in Figure 5.2b and c. Like in the C8-BTBT case,  $\text{C}_{60}\text{F}_{48}$  form islands, most of them decorating the asymmetric BTBT-C8 step edges and are distinguished from the surrounding asymmetric BTBT-C8 layer by their lighter colour (i.e., higher friction) in the lateral force images.

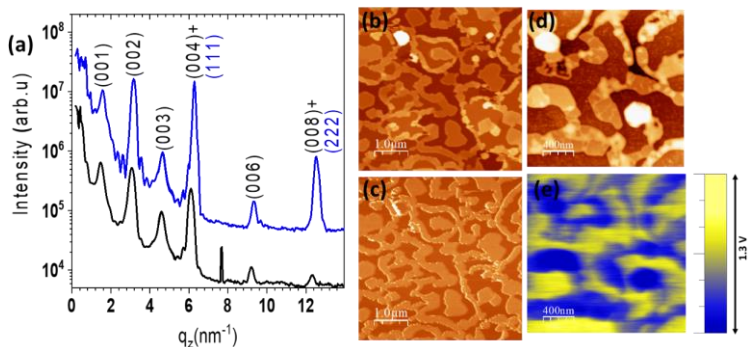


Figure 5.2. (a) Out-of-plane XRD for a 22nm thick asymmetric BTBT-C8 film before (black line) and after (blue line) 15nm thick  $\text{C}_{60}\text{F}_{48}$  deposition on top. The spike at  $q_z = 7.8\text{nm}^{-1}$  is an artefact. (b, c) Topography and corresponding lateral force map for 2nm of  $\text{C}_{60}\text{F}_{48}$  deposited on top of a 16nm thick asymmetric BTBT-C8 film (d, e) Topography and corresponding surface potential map (KPFM) of the same sample.

Like in the C8-BTBT case,  $\text{C}_{60}\text{F}_{48}$  island heights range between 5nm and 12nm, i.e., corresponding to 5 - 12 individual layers of the dopant ( $\sim 1\text{nm}$ ),

supporting the FCC structure of the  $C_{60}F_{48}$  crystallites derived from XRD data. Figure 5.2d and e show the topography and the corresponding surface potential (KPFM) map of an asymmetric BTBT-C8 film with  $C_{60}F_{48}$  on top. The SP map shows a lower (higher) surface potential (work function) in the regions covered by  $C_{60}F_{48}$ . A similar trend is observed in the SP maps of C8-BTBT, which is described later in this chapter.

The long-term stability of the asymmetric BTBT-C8 film with and without  $C_{60}F_{48}$  has been investigated. Figure 5.3a and c show the topography of a fresh asymmetric BTBT-C8 film, and the same sample measured after two years, respectively. A strong dewetting of asymmetric BTBT-C8 films from the initial laterally continuous films to high islands with large areas of the uncovered substrate is observed. However, the topographic images of fresh  $C_{60}F_{48}$ /asymmetric BTBT-C8 films and those measured more than one year later (Figure 5.3b and d) illustrate the role of the dopant to provide enhanced morphological stability to the asymmetric BTBT-C8 films. Remarkably, as in the symmetric case, dewetting of the asymmetric BTBT-C8 film is hindered by the  $C_{60}F_{48}$  on the surface.

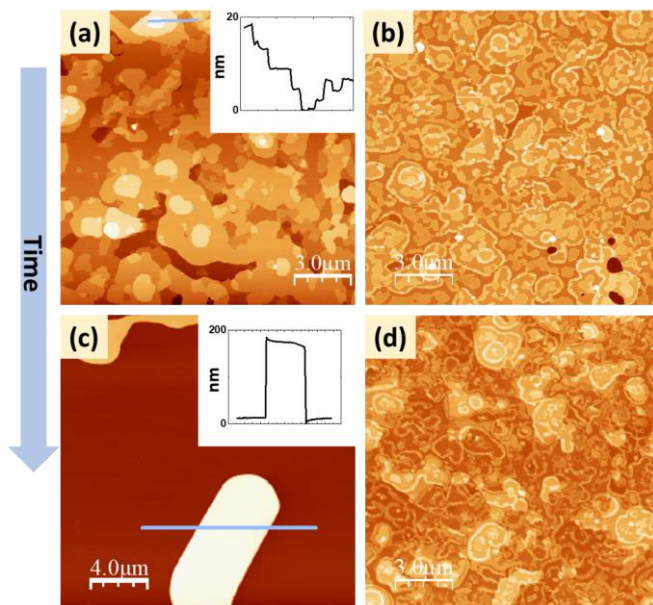


Figure 5.3. AFM topography of fresh films of (a) a pristine 16nm thick asymmetric BTBT-C8, (b) 2nm of  $C_{60}F_{48}$  on a 24nm thick asymmetric BTBT-C8 film. The topography of the same samples was measured after two years for (c) asymmetric BTBT-C8, and (d)  $C_{60}F_{48}$ /asymmetric BTBT-C8. The insets show the height profiles along the marked lines.

As it occurs in the case of the symmetric parent, the thermal stability of the asymmetric BTBT-C8 films is improved by  $C_{60}F_{48}$  deposition on the surface. On one hand, the XRD data of Figure 5.4a reveal that annealing the pristine asymmetric BTBT-C8 film at 80°C leads to film desorption, and the Bragg peaks no longer exist. On the other hand, for the asymmetric BTBT-C8 film with the dopant on top, the ordered lamellae structure stands even up to 100°C (Figure 5.4b).

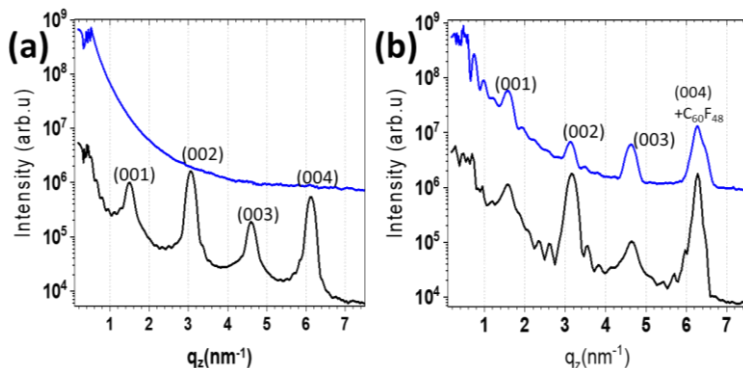


Figure 5.4. Out-of-plane XRD of (a) pristine 22nm thick asymmetric BTBT-C8 film and (b) with 15nm of  $C_{60}F_{48}$  on top. The black curves: at RT and the blue curves: after annealing the films at 80°C in (a) and 100°C in (b).

The fact that the Bragg peaks remain unaffected implies that there is no intermixing of  $C_{60}F_{48}$  and asymmetric BTBT-C8 molecules as otherwise expected from the bulky shape of the dopant. An interesting observation of intensity reduction of the (002) peak, which has a contribution from single-layer structure, with annealing at  $\sim 100^\circ\text{C}$  reveals lower stability of the single-layer structure as compared to the bilayer structure.

## 5.2. Interfacial structure of $C_{60}F_{48}$ on C8-BTBT or DPh-BTBT

To have full insight into the role of OSC side groups in the dopant/OSC interface the structure and morphology of films made out of two symmetric molecules, C8-BTBT and DPh-BTBT, are compared before and after  $C_{60}F_{48}$  deposition on their top. Because a detailed discussion on C8-BTBT was presented in chapter 4, this section focuses on DPh-BTBT and the interface

with C<sub>60</sub>F<sub>48</sub>. Figure 5.5 shows the AFM topography of a DPh-BTBT (7nm) thin film. When deposited on clean native SiO<sub>2</sub> substrates, DPh-BTBT forms layered films with a single-layer thickness of  $\sim 2$ nm, which is almost its molecular length.<sup>[30],[130]</sup> This confirms the standing-up the configuration of the molecules within each layer. The analysis of several topographic images of DPh-BTBT thin films reveals the same terrace height for all individual layers.

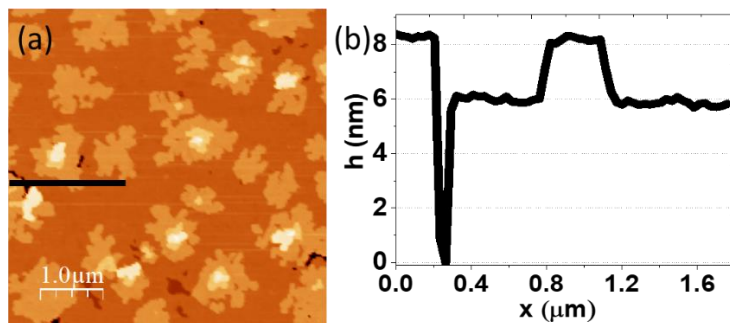


Figure 5.5. Topography and the corresponding height profile along with the indicated black segments in the image for a 7nm thick DPh-BTBT film.

The most significant difference between DPh-BTBT films and C8-BTBT is that, in the present case, the individual layers are laterally continuous covering the substrate and following a layer-by-layer growth (Frank–van der Merwe growth mode), while C8-BTBT thin films of similar thickness consist of islands with exposed uncovered substrate. We note that, however, for the thicknesses typically employed in OFETs ( $> 20$ nm), C8-BTBT forms closed films (laterally continuous).<sup>[32]</sup> Although, both DPh-BTBT and C8-BTBT films contain similar aromatic core planes within the lamellar structure, these planes (responsible for the transport characteristics of the OSC) are separated vertically by their distinct side groups (long linear chains in C8-BTBT versus short cyclic groups in DPh-BTBT). The different growth mode of DPh-BTBT and C8-BTBT on SiO<sub>2</sub> is due to the different interaction between their side groups and the substrate which determines the substrate/OSC interfacial structure and growth mode.<sup>[131],[132],[8]</sup>

X-ray diffraction measurements were carried out on DPh-BTBT thin films at ID03 beamline, ESRF, France. Out-of-plane and grazing incidence (GIXD) geometries were used to study the thin film structure, perpendicular (out-of-plane) and parallel (in-plane) to the substrate, respectively. Figure 5.6a shows the out-of-plane XRD of pristine DPh-BTBT films.



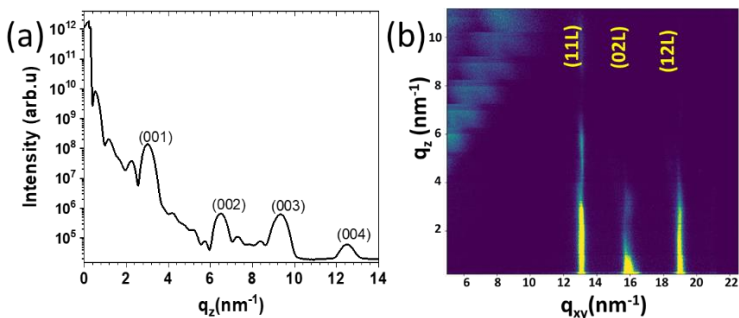


Figure 5.6. (a) Out-of-plane XRD pattern and (b) 2D GIXD map of a pristine 11nm thick DPh-BTBT film on native SiO<sub>2</sub>.

The presence of Bragg peaks up to multiple orders indicates that the films are well oriented with the (001) plane parallel to the surface. The inter-planar spacing,  $d_{001}$  calculated from the Bragg peaks is 2.01nm for DPh-BTBT and agrees with the AFM data as well as with the reported crystalline structure.<sup>[36]</sup> In 2D GIXD maps of DPh-BTBT films (Figure 5.6b), diffraction rods were observed at  $q_{xy} \sim 13.1\text{nm}^{-1}$ ,  $q_{xy} \sim 15.7\text{nm}^{-1}$  and  $q_{xy} \sim 18.8\text{nm}^{-1}$  that are assigned to (11L), (02L) and (12L) rods which are characteristic XRD features of the herringbone packing reported for other BTBT molecules, in the plane parallel to the substrate.<sup>[133],[120]</sup> The calculated lattice parameters for DPh-BTBT, from the position of the peaks for a rectangular in-plane unit cell, are  $a = 6.03\text{\AA}$  and  $b = 7.97\text{\AA}$ .

The dopant/OSC interfacial structure was characterized upon depositing C<sub>60</sub>F<sub>48</sub> on top of the same DPh-BTBT film. Figure 5.7a displays the corresponding 2D-GIXD pattern of the heterostructure. Crystalline features from C<sub>60</sub>F<sub>48</sub> at  $q_{xy} \sim 5.99\text{nm}^{-1}$ ,  $q_{xy} \sim 10.39\text{nm}^{-1}$  and  $q_{xy} \sim 11.90\text{nm}^{-1}$  were observed. The scattering intensity measured along the  $q_z$ -direction indicates the crystallinity of the C<sub>60</sub>F<sub>48</sub> structures formed on top of the DPh-BTBT films. However, there are no C<sub>60</sub>F<sub>48</sub> OOP Bragg peaks observed in the out-of-plane XRD pattern (Figure 5.7c). In the previous chapter, it was already confirmed that C<sub>60</sub>F<sub>48</sub> is forming an FCC structure with the (111) plane parallel to the surface on C8-BTBT. The GIXD data of the C<sub>60</sub>F<sub>48</sub>/DPh-BTBT heterostructure validate that a similar structure of the dopant is forming on top of DPh-BTBT.



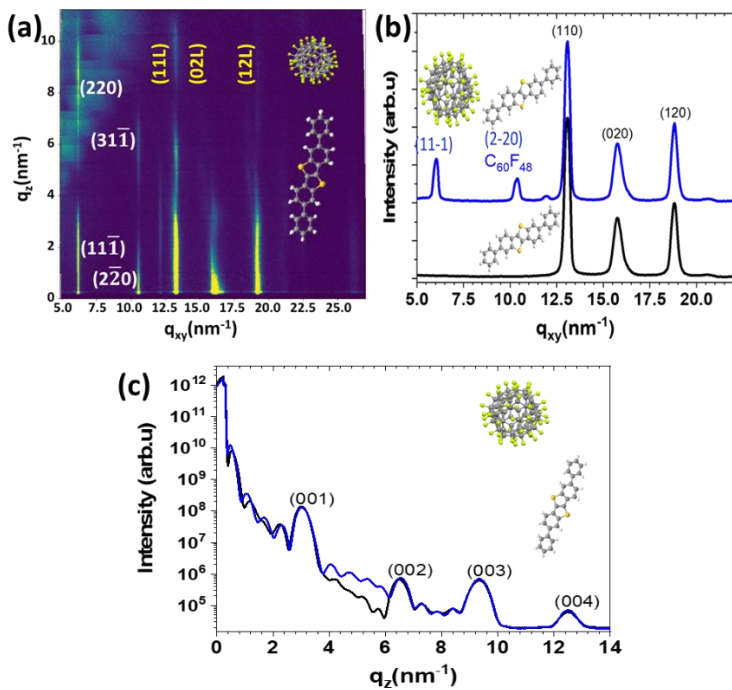


Figure 5.7. 2D-GIXD map of (a) 2nm of C<sub>60</sub>F<sub>48</sub> on a 11nm thick DPh-BTBT film grown on a native Si oxide substrate and (b) the corresponding in-plane GIXD from the 2D-GIXD maps and (c) out-of-plane XRD data of a 11nm thick DPh-BTBT film before (black) and after (blue) C<sub>60</sub>F<sub>48</sub> deposition.

AFM measurements were performed to investigate the morphology of the dopant/OSC interface and compare the cases of the two symmetric BTBTs studied, i.e., to get insight into the interaction of C<sub>60</sub>F<sub>48</sub> with the two different OSC film terminations. Figure 5.8a and c show the morphology obtained for the same sub-monolayer coverage of C<sub>60</sub>F<sub>48</sub> (0.4nm) deposited on C8-BTBT and DPh-BTBT thin films, respectively. As shown in the previous chapter, C<sub>60</sub>F<sub>48</sub> forms crystallites at the edges of C8-BTBT terraces. In contrast, on the DPh-BTBT surface C<sub>60</sub>F<sub>48</sub> forms aggregates of  $\sim$  1nm height with a rather uniform distribution over the DPh-BTBT surface, without having any preference for attaching to any morphological feature (island edges, lower or upper terraces etc). The average height of the non-compact aggregates in the case of DPh-BTBT is comparable with the C<sub>60</sub>F<sub>48</sub> molecular size (1nm). Even though XRD data suggests the same C<sub>60</sub>F<sub>48</sub> structure, the interfacial morphology is dissimilar, which implies that the phenyl-terminated films

promote a layer-by-layer growth of the fluoro-fullerenes on the OSC. A comparative study of the local work function changes caused by the deposition of  $C_{60}F_{48}$  on both BTBT derivatives is presented in the next section.

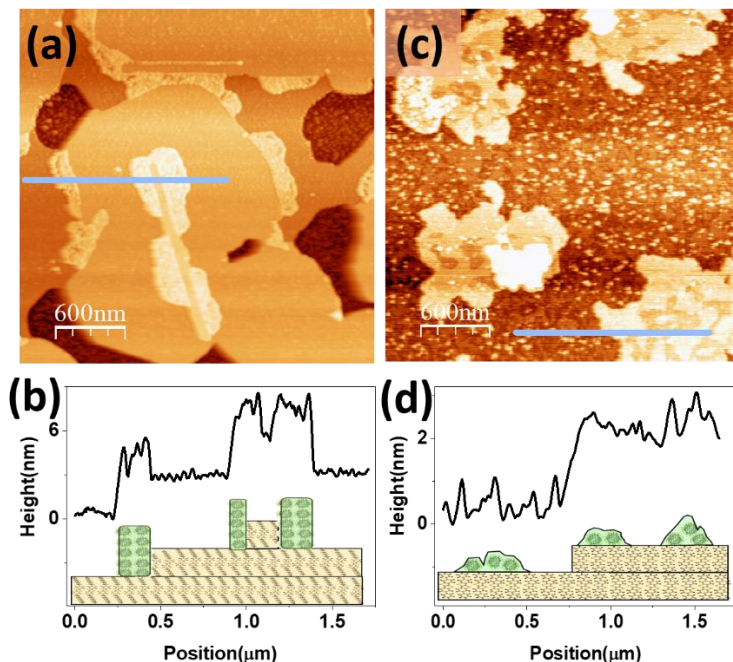


Figure 5.8. Topographic images and the corresponding profiles of 0.4nm of  $C_{60}F_{48}$  on (a, b) a 16nm thick C8-BTBT film and (c, d) a 15nm thick DPh-BTBT film grown on native silicon oxide substrate, respectively.

### 5.3. Local changes in the work function

Figure 5.9 shows the topography and the corresponding surface potential (SP) measured by KPFM for pristine C8-BTBT and DPh-BTBT (Figure 5.9a, b and h, i, respectively) and two coverages (1nm and 3nm) of  $C_{60}F_{48}$  deposited on their top (Figure 5.9c-f and j-m, respectively). The nucleation and growth of the  $C_{60}F_{48}$  crystallites on C8-BTBT have been observed in the topography as well as in the surface potential map. Upon deposition of 1nm of  $C_{60}F_{48}$  on C8-BTBT, the dopant forms compact and flat clusters at the step edges of the underlying C8-BTBT film leaving uncovered the rest of the terraces, as schematically depicted in Figure 5.9g.

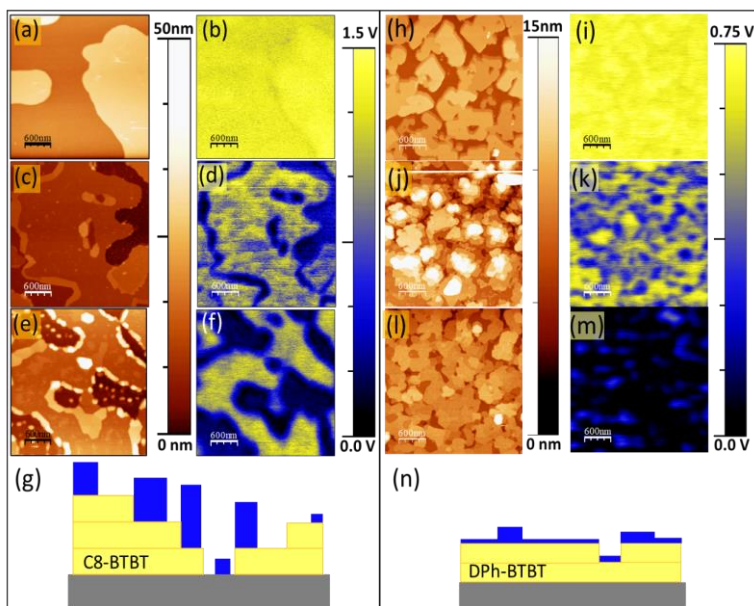


Figure 5.9. Topography and simultaneous SP maps were measured by KPFM. Left: an 8nm thick C8-BTBT film before (a, b) and after  $C_{60}F_{48}$  deposition of 1nm (c, d) and 3nm (e, f); Right: a 9nm thick DPh-BTBT film before (h, i) and after  $C_{60}F_{48}$  deposition of 1nm (j, k) and 3nm (l, m). Cartoons with the growth models are shown for each case (g, n) respectively.

For the deposited  $C_{60}F_{48}$  coverages of 1nm and 3nm, the dopant cluster's height ranges from 3nm - 5nm and up to 9nm - 12nm, respectively. The direct correlation between morphology (Figure 5.9j-l) and SP maps (Figure 5.9k-m) is obvious, showing a larger  $\phi$  (lower SP) in the areas covered by the  $C_{60}F_{48}$  crystallites.

However, as expected from the different distribution and growth of the dopant on each molecular film, for the same coverages of  $C_{60}F_{48}$ , the nanoscale SP distribution on DPh-BTBT is different than that on C8-BTBT (Figure 5.9d and k). For a  $C_{60}F_{48}$  coverage of 1nm, the correlation between dopant location and lower values of surface potential is evident, with variability due to differences in the  $C_{60}F_{48}$  distribution. Upon 3nm deposition of  $C_{60}F_{48}$ , the DPh-BTBT film surface is fully covered by the dopant (as schematically modelled in Figure 5.9n) with a nearly uniform and lower value of surface potential. The mean value of surface potential is 0.7V lower than that for the pristine DPh-BTBT i.e., an increase in work function ( $\Delta\phi$ ) of the

same magnitude. Even though the work function is found to increase as a function of the  $C_{60}F_{48}$  thickness for both cases, a variety of crystallite heights is observed in the  $C_{60}F_{48}$ /C8-BTBT heterostructure. The maximum contrast measured in SP is 1.5V. Such large values may have originated from the charge transfer between the dopant and the substrate.<sup>[134],[135]</sup> It is also noted that  $C_{60}F_{48}$  in direct contact with the exposed substrate, as seen in Figure 5.9e-f, shows an increase in work function, indicating charge transfer between Si and the dopant through the native oxide.

To disentangle the contribution from charge exchange with the substrate, Si wafers with either native or thick 200nm oxide were employed to measure the SP on  $C_{60}F_{48}$  crystallites versus aggregate thickness. Figure 5.10 shows the work function difference ( $\Delta\phi$ ) for  $C_{60}F_{48}$  on C8-BTBT and the uncovered C8-BTBT as a function of the height of the  $C_{60}F_{48}$  islands ( $h$ ) for heterostructures grown on native  $SiO_2$  (red circles) and 200nm thermal  $SiO_2$  (black squares), respectively. Error bars indicate the standard deviation of the measurements. The work function increases with  $C_{60}F_{48}$  crystallites' height and saturates for crystallites taller than 8nm. The saturation value of the work function difference is  $\Delta\phi \sim 1\text{eV}$  for heterostructures grown on native  $SiO_2$  and  $\Delta\phi \sim 0.5\text{eV}$  for heterostructures grown on 200nm thick  $SiO_2$ . Charge transfer with Si through the native  $SiO_2$  can be ruled out for heterostructures on the thick oxide (illustrated in Figure 5.10b-c), which means that the measured difference of SP exclusively arises from the electronic changes at the dopant/OSC interface.

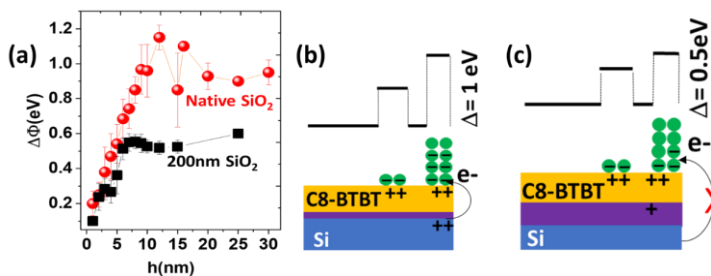


Figure 5.10. (a) Work function difference ( $\Delta\phi$ ) between  $C_{60}F_{48}$  and the surrounding C8-BTBT vs.  $C_{60}F_{48}$  crystallites' height ( $h$ ) on native  $SiO_2$  (red) and 200nm thermal  $SiO_2$  (black). Schemes of charge transfer for  $C_{60}F_{48}$ /C8-BTBT on (b) native  $SiO_2$  and (c) 200nm thick  $SiO_2$ .

This result confirms that after establishing electronic equilibrium in the whole system,<sup>[136],[137],[138]</sup> the absolute  $\Delta\phi$  measured for the  $C_{60}F_{48}$ /C8-BTBT on native  $SiO_2$  has two contributions: charge transfer between  $C_{60}F_{48}$  and C8-

BTBT (interfacial doping) and from the silicon substrate to  $C_{60}F_{48}$  through C8-BTBT and native  $SiO_2$ . For both substrates, the initial increase in  $\Delta\phi$  with  $C_{60}F_{48}$  crystallites' thickness demonstrates that band bending takes place due to the interfacial doping via integer charge transfer to the dopant.

To advance in comprehending the influence of side groups in the dopant/OSC electronic interaction, a comparison of the work function change is required without the influence of charge transfer with the substrate. This goal implies the use of wafers with thick oxide layers. Figure 5.11 shows the comparison of SP maps of  $C_{60}F_{48}$ /C8-BTBT and  $C_{60}F_{48}$ /DPh-BTBT heterostructures grown on a 200nm thick  $SiO_2$  substrate.

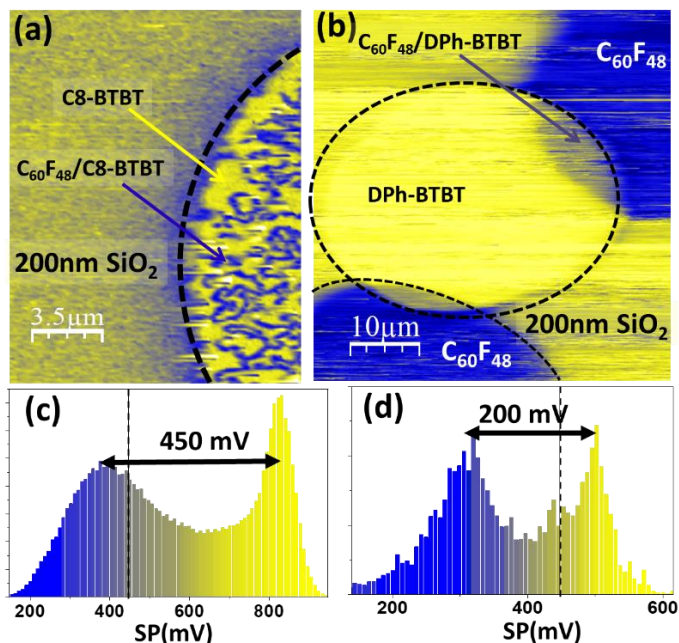


Figure 5.11. Surface potential maps and corresponding SP histograms for patterned (a, c)  $C_{60}F_{48}$  (1.5nm)/DPh-BTBT (6nm) and (b, d)  $C_{60}F_{48}$  (1.5nm)/C8-BTBT (5nm) on 200nm thick  $SiO_2$ . The blue/yellow colour scale means lower/higher SP. A shadow mask was used during the deposition of OSC and dopant. The SP histograms correspond to areas with bare and covered BTBTs in the SP maps. The vertical black dashed lines in the histograms indicate the SP of the exposed substrate.

A shadow mask was used during the deposition of the molecules to fabricate micrometer-sized regions of dopant/OSC heterojunction with exposed

regions of the substrate. The  $C_{60}F_{48}$ /C8-BTBT interface in Figure 5.11a shows the characteristic inhomogeneous SP maps with lower SP on top of  $C_{60}F_{48}$  crystallites surrounded by bare C8-BTBT regions. Because of the different growth modes of the dopant on the phenyl terminated surface, to have uncovered DPh-BTBT regions in a micrometer-sized single SP map, the shadow mask was moved (under vacuum), before the  $C_{60}F_{48}$  deposition. Hence, Figure 5.11b shows the SP measured on 200nm  $SiO_2$ , pristine DPh-BTBT and  $C_{60}F_{48}$  directly on thick  $SiO_2$  and an intersection zone with  $C_{60}F_{48}$ /DPh-BTBT interface. The different regions are indicated in the images. Two peaks in the SP histogram correspond to the mode values of measured SP data, on regions covered by  $C_{60}F_{48}$  and the uncovered BTBT region. Remarkably, the average difference in work function between regions of  $C_{60}F_{48}$ /DPh-BTBT and bare DPh-BTBT is  $\Delta\phi \sim 0.2\text{eV}$  and regions of  $C_{60}F_{48}$ /C8-BTBT and bare C8-BTBT is  $\Delta\phi \sim 0.45\text{eV}$ , for similar  $C_{60}F_{48}$  thickness. The work function change is 0.25eV lower for the DPh-BTBT case than that for the C8-BTBT one.

In this section, it has been demonstrated how the distinct dopant/OSC interfacial morphology, arising from the different side-groups of the BTBT derivatives, correlates with the surface potential distribution at the interface in each case. These differences would have clear implications on device performances.

## 5.4. Energy level alignment

Photoelectron spectroscopic studies were performed to probe the changes in the electronic levels of OSC after interfacial doping. In order to avoid undesired charging during the measurement, doped Si substrates (covered by native silicon oxide) were used. To reduce the influence of the described charge exchange between OSC and the substrate (as shown in Figure 5.10), considerably thicker ( $\sim 15\text{nm}$ ) films of BTBT molecules were deposited. UPS measurements of the secondary electrons cut-off (SECO) and the near Fermi level valence band (VB) regions were measured to probe the changes in the work function of the thin film and the HOMO of the BTBT molecules, respectively, before and after  $C_{60}F_{48}$  deposition (more details of the technique are in the experimental section 3.7). All the molecules (BTBTs and dopants) were deposited under a vacuum and in-situ UPS measurements were performed. Figure 5.12 displays the SECO region of the Si substrate, C8-BTBT and DPh-BTBT films. The spectra demonstrate that while C8-BTBT does not significantly alter the Si substrate, DPh-BTBT deposition results in a

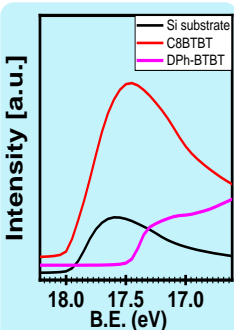


Figure 5.12. SECO measured by UPS for a 16nm thick C8-BTBT film (red solid curve) and a 15nm thick DPh-BTBT (red dotted curve) on native Si oxide.

considerable shift of the SECO. We note that the measured work function of the Si substrate (3.3eV, obtained from the SECO) and the LUMO of the BTBT derivatives ( $\sim 1.55\text{eV}$ ),<sup>[114],[5],[30]</sup> does not favour charge transfer between OSC and Si.<sup>[139]</sup> On the other hand, several interfacial phenomena like molecular disorder, adsorption induces interfacial dipoles, intramolecular polar bonds, Fermi level pinning etc.,<sup>[140],[141],[142],[143]</sup> may affect the vacuum level alignment between the OSC and the substrate. Hence the modification of vacuum level by DPh-BTBT may arise from the interplay between concurrent interfacial phenomena. Disentangling these effects needs a more detailed study using several techniques. Since in this thesis we are mainly interested in the dopant/OSC interfacial electronic level alignment, the modification of the electronic levels of the pristine films after  $\text{C}_{60}\text{F}_{48}$  deposition was analysed.

Figure 5.13 shows the SECO and VB regions of a C8-BTBT film, which give evidence of the changes in the energy of HOMO of the OSC and the vacuum level of the system with subsequent depositions of two coverages of  $\text{C}_{60}\text{F}_{48}$ , 2Å and 4Å.

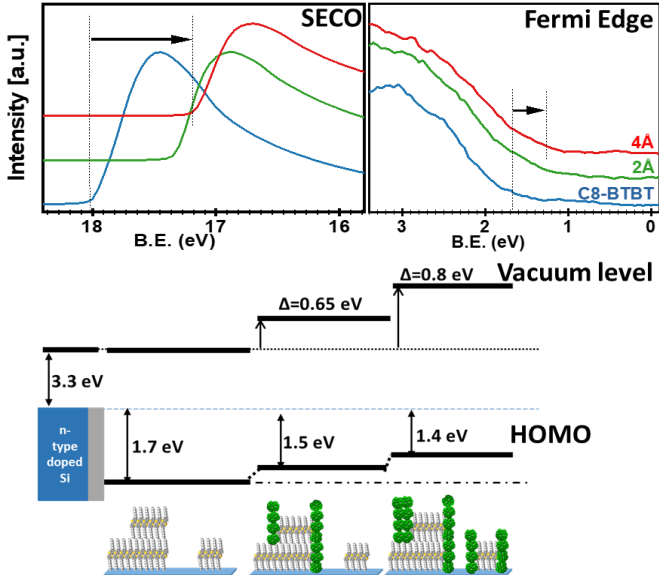


Figure 5.13. SECO and VB regions were measured by UPS for a 16nm thick C8-BTBT film grown on Si, prior (blue) and after two coverages of  $\text{C}_{60}\text{F}_{48}$  (green and red). Bottom: Energy level diagram extracted from the UPS data with the corresponding illustrative cartoons.



Both vacuum level and HOMO shifted to a lower BE upon dopant deposition. A work function increase of  $\Delta\phi \sim 0.8\text{eV}$  accompanied by a  $\Delta(\text{HOMO}) \sim 0.3\text{eV}$  of C8-BTBT, for  $4\text{\AA}$  of  $\text{C}_{60}\text{F}_{48}$  is observed. An increase in work function and a shift of the HOMO towards the Fermi level indicate that  $\text{C}_{60}\text{F}_{48}$  is doping the film. The shift in VB and SECO are not equal and this implies the presence of a surface dipole. A shift of the energy levels to lower BE with increasing coverage of  $\text{C}_{60}\text{F}_{48}$  was observed in the case of DPh-BTBT films (Figure 5.14). A shift of the SECO by  $\Delta\phi \sim 0.35\text{eV}$  and  $\Delta\phi \sim 0.55\text{eV}$  for  $2\text{\AA}$  and  $4\text{\AA}$  of  $\text{C}_{60}\text{F}_{48}$  respectively is observed. A lower work function change compared to C8-BTBT is consistent with the KPFM measurement shown in Figure 5.11. The HOMO is shifted to a lower BE by  $0.2\text{eV}$  and  $0.4\text{eV}$  for  $2\text{\AA}$  and  $4\text{\AA}$  of  $\text{C}_{60}\text{F}_{48}$ , respectively. No evidence of filled molecular orbitals of  $\text{C}_{60}\text{F}_{48}$  has been observed in the energy gap region for BTBT films after dopant deposition.

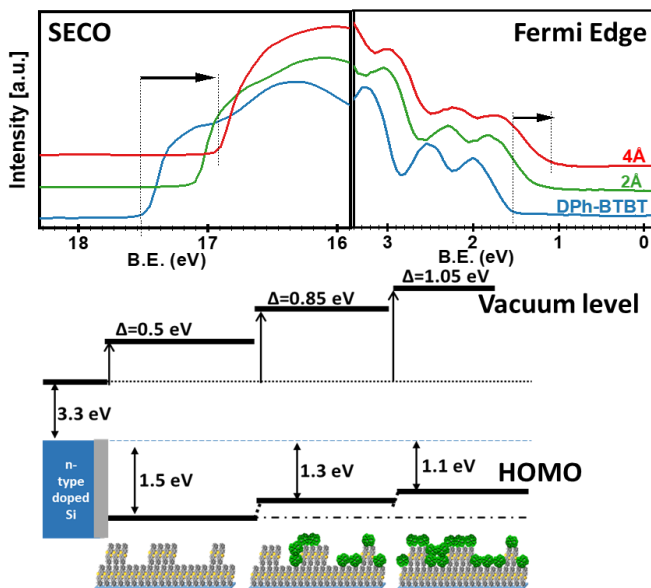


Figure 5.14. SECO and VB regions measured by UPS for a 15nm thick DPh-BTBT film on a Si substrate prior (blue) and after two coverages ( $2\text{\AA}$  and  $4\text{\AA}$ ) of  $\text{C}_{60}\text{F}_{48}$  (green and red): Bottom: Energy level diagram extracted from the UPS data with the corresponding illustrative cartoons.

The ionization potential (IP), calculated from the HOMO energy (before doping) is  $\text{IP}_{\text{C8-BTBT}} = 5.0\text{eV}$  for C8-BTBT and is  $\text{IP}_{\text{DPh-BTBT}} = 5.3\text{eV}$  for DPh-BTBT. The reported value of the LUMO for  $\text{C}_{60}\text{F}_{48}$  is  $\sim 5.5\text{eV}$ .<sup>[64],[59]</sup> This means that charge transfer from the HOMO of both BTBT molecules to the LUMO of



C<sub>60</sub>F<sub>48</sub> is energetically favourable, with more charge transfer at the C<sub>60</sub>F<sub>48</sub>/C8-BTBT interface due to the larger energy difference between the HOMO and the LUMO. Hence, a larger  $\Delta\phi$  of  $\sim 0.25\text{eV}$  observed for C<sub>60</sub>F<sub>48</sub>/C8-BTBT films in comparison to C<sub>60</sub>F<sub>48</sub>/DPh-BTBT has attributed to a larger surface dipole originating from the charge transfer at the C<sub>60</sub>F<sub>48</sub>/C8-BTBT interface due to the lower ionization energy of C8-BTBT films.

The integer charge transfer model (ICT) predicts that charge transfer occurs until electronic equilibrium between the Fermi level and the LUMO of C<sub>60</sub>F<sub>48</sub> is attained.<sup>[139]</sup> In the case of OSC between the substrate and dopant, energy levels are aligned by Fermi level pinning between the substrate and the dopant through the OSC.<sup>[44]</sup> For both BTBT systems, the substrate and the dopant are the same, then, if the ICT model stood, the vacuum level shift would be the same for both BTBT films for similar coverage of C<sub>60</sub>F<sub>48</sub>. However, for similar C<sub>60</sub>F<sub>48</sub> coverage, the change in vacuum level with respect to the substrate is different for each of the BTBT films. This result reveals the involvement of BTBT molecules in the electronic equilibrium process of the doped films via alignment of the HOMO of BTBT molecules to the LUMO of C<sub>60</sub>F<sub>48</sub> through interface charge transfer.

To disentangle the effect of doping on the electronic levels of the BTBT molecules, photoelectron spectroscopy using X-rays (XPS) was employed to probe the core levels of the different elements present. Figure 5.15 shows the BE of core electronic levels of carbon (C1s) atoms and the corresponding fits, as well as the changes in the BE of sulphur (S2p) atoms of the C8-BTBT molecules in the different heterostructures, i.e., before and after the dopant depositions. Note that while both dopant and the OSC contain C atoms, S atoms are specific for C8-BTBT and F atoms are specific for C<sub>60</sub>F<sub>48</sub>. The C1s spectra of pristine C8-BTBT (blue) show a considerable wide peak around 285eV which is well fitted with two components corresponding to the two types of carbon atoms in the C8-BTBT molecules, namely,  $sp^3$  (C-C) and  $sp^2$  (C=C) arising from the C atoms in the aliphatic chains (BE = 285.42eV) and the aromatic cores (BE = 284.82eV), respectively. The relative area between these two components coincides with their stoichiometric ratio in the molecule (16/14). After C<sub>60</sub>F<sub>48</sub> deposition on top of the OSC film, a shift by  $\sim 0.13\text{eV}$  of the C1s peak is accompanied by the emergence of two new peaks in the higher BE region (287eV – 290eV), which are the signature of the C-F and C-CF bonds in C<sub>60</sub>F<sub>48</sub>.<sup>[59],[144]</sup> Figure 5.15d shows that the corresponding S2p ( $2p_{1/2}$  and  $2p_{3/2}$ ) core levels only suffer from subtle changes during dopant deposition. In principle, the faint shifts observed in the core levels of the C8-BTBT molecules are somehow surprising because of the shift measured in the work function.

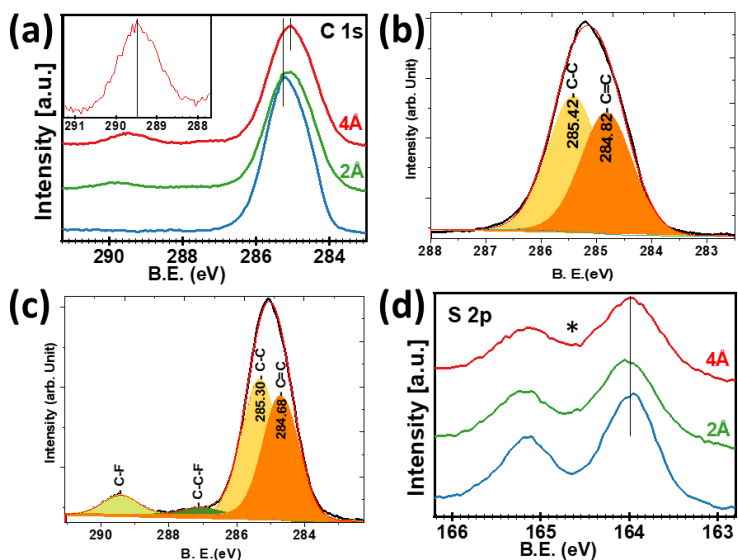


Figure 5.15. (a)  $C1s$  core levels were measured by UPS for C8-BTBT (16nm) on Si, prior (blue) and after two coverages of  $C_{60}F_{48}$  depositions (green and red). Inset shows the zoom of the higher BE region in the red curve. The fits of  $C1s$  core levels of (b) pristine C8-BTBT and (c)  $4\text{Å}$   $C_{60}F_{48}/C8\text{-BTBT}$  (d) XPS spectra of  $S2p$  core levels of C8-BTBT on Si, prior (blue) and after two coverages of  $C_{60}F_{48}$  depositions (green and red).

The crucial evidence clarifying this fact comes from the shift towards lower BE of the  $C1s$  components corresponding to  $C_{60}F_{48}$  when the coverage increases from  $2\text{Å}$  to  $4\text{Å}$  (inset of Figure 5.15a). It is worth commenting here that XPS is a macroscopic technique that provides data averaged of a relatively large area on the surface while does not describe local electronic effects. In this context, the whole scenario can be explained by the presence of a surface dipole at the  $C_{60}F_{48}/C8\text{-BTBT}$  interface, otherwise confirming the charge transfer between C8-BTBT and the dopant. The most plausible explanation for our observations (fixed  $S2p$  peak position and faint changes in  $C1s$  of C8-BTBT after  $C_{60}F_{48}$  deposition) is that only C8-BTBT molecules under the  $C_{60}F_{48}$  islands are affected by doping and the surrounding molecules remain unaffected. This explanation is fully compatible with the topographic and local surface potential data described in section 5.3. Figure 5.8a displays the topography of the samples used to measure XPS/UPS. In this particular region of the sample, only 12% of the C8-BTBT film surface is covered by  $C_{60}F_{48}$  (the percentage can be different depending on the area).

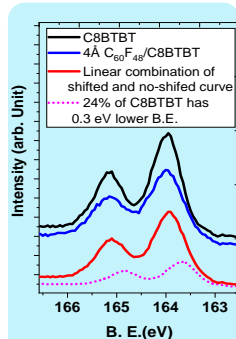


Figure 5.16. Interpretation of the  $S2p$  core level spectra of C8-BTBT.

Because of the non-uniform distribution of the dopant on the surface, the S2p and C1s core levels of the C8-BTBT species have a contribution of around 90% from the dopant-free C8-BTBT. This is well supported by slight changes in the S2p spectra of the doped C8-BTBT: a shallowing of the valley between the S2p<sub>3/2</sub> and S2p<sub>1/2</sub> doublet denoted by (\*) in Figure 5.15d. An analysis of the spectra to consider the two types of C8-BTBT molecules (in contact or not with C<sub>60</sub>F<sub>48</sub>) is illustrated in Figure 5.16. A linear combination (red) of two doublets: 76% of the pristine C8-BTBT (black) plus 24% of another one shifted by 0.3eV to lower BE (pink) shows a similar valley shallowing to the spectrum of C8-BTBT film with 4Å C<sub>60</sub>F<sub>48</sub> (blue). The same argument, considering the amount of C8-BTBT in contact with the dopant, can be extended to explain the small shift of the C1s. The present analysis highlights the importance of considering the surface morphology, which as we have already demonstrated (section 5.3) is affected by the OSC side groups, to understand the macroscopic effects.

Figure 5.17 shows the core levels measured for DPh-BTBT and subsequent C<sub>60</sub>F<sub>48</sub> deposition on the OSC film surface. Note that, due to the lack of aliphatic chains, in this case, the C1s signal of pristine DPh-BTBT (Figure 5.17a) is much narrower than for pristine C8-BTBT (Figure 5.15b).

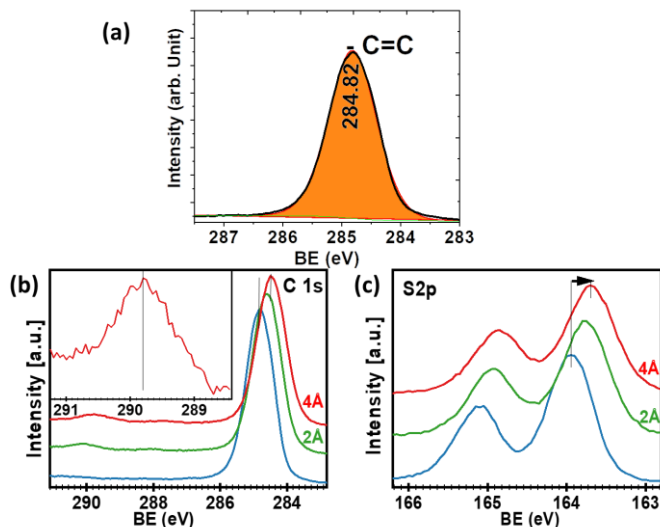


Figure 5.17. (a) The fit of the C1s core level of pristine DPh-BTBT (15nm) on Si was measured by UPS. XPS spectra of (b) C1s and (c) S2p core levels of DPh-BTBT on Si, prior (blue) and after two coverages of C<sub>60</sub>F<sub>48</sub> depositions (green and red). The inset in (b) is the magnification of the higher BE region, which corresponds to the C-F peak in the red curve.

The shifts in the core levels of DPh-BTBT confirm doping. Unlike C8-BTBT, the shifts towards lower BE are consistent with the shift observed in the HOMO of the DPh-BTBT. Yet, the magnitude of the shifts is non-identical with a  $\Delta(\text{HOMO}) \sim 0.4\text{eV}$ ,  $\Delta(\text{S}2\text{p}) \sim 0.25\text{eV}$  and  $\Delta(\text{C}1\text{s}) \sim 0.35\text{eV}$ . This type of behaviour can be attributed to an unconventional upward band bending of DPh-BTBT energy levels at the interface.<sup>[140]</sup> The shift of the C-F peak around  $\sim 290\text{eV}$  confirms charge transfer at the  $\text{C}_{60}\text{F}_{48}$ /DPh-BTBT interface. A noticeable shift of  $0.25\text{eV}$  in the  $\text{S}2\text{p}$  doublet DPh-BTBT as compared with that of C8-BTBT can be explained by the homogeneous distribution of  $\text{C}_{60}\text{F}_{48}$ , covering most of the surface and therefore affecting most of the DPh-BTBT molecules. The above results also validate that the nanomorphology of the interface, determined by the side groups of the OSC leads to surface potential inhomogeneity at small lateral dimensions which are not accessible to the photoelectron spectroscopy (area-averaged values).<sup>[145]</sup> However, despite the heterogeneity of the  $\text{C}_{60}\text{F}_{48}$ /C8-BTBT interface, a single SECO threshold value ( $0.8\text{eV}$ ) was measured, that matches the largest work function values measured on top of taller  $\text{C}_{60}\text{F}_{48}$  crystallites by KPFM ( $0.9\text{V}$ ). Even if both KPFM and UPS give similar values of work function changes with  $\text{C}_{60}\text{F}_{48}$  coverage, for each of the two systems, KPFM provides the local information with accuracy on the nanoscale.

## 5.5. Contact doping of DPh-BTBT OFETs

It is worth mentioning here that the results from the previous chapter demonstrate that  $\text{C}_{60}\text{F}_{48}$  doping enhances the effective field-effect mobility of the C8-BTBT OFETs by a reduction of the contact resistance. Achieving a doped interface is crucial for contact resistance reduction in OFETs. To evaluate the influence of OSC side groups on device performance, DPh-BTBT OFETs were fabricated and characterized. A similar fabrication method as for C8-BTBT OFETs was followed to prepare BG-TC DPh-BTBT OFETs, with different channel lengths between  $30\mu\text{m}$  and  $100\mu\text{m}$ . For simplicity,  $\text{C}_{60}\text{F}_{48}$  ( $1.2\text{nm}$ ) was evaporated all over the surface of the DPh-BTBT layer grown on  $200\text{nm}$   $\text{SiO}_2$  and gold contacts were deposited on top.

Figure 5.18 shows the device characterization of DPh-BTBT OFETs with and without dopant for a channel length of  $40\mu\text{m}$ . Surprisingly, unlike C8-BTBT OFETs, the transfer curves do not show a noticeable improvement up on  $\text{C}_{60}\text{F}_{48}$  deposition. In fact, the OFETs with/without  $\text{C}_{60}\text{F}_{48}$  fabricated, with a  $40\mu\text{m}$  channel (Figure 5.18a), show a small shift of the transfer curve towards a more negative gate value.

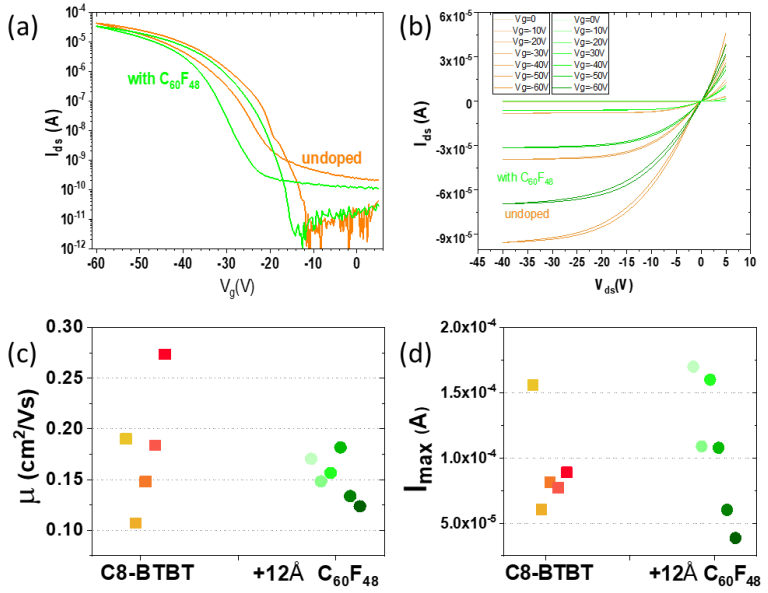


Figure 5.18. (a) Transfer and (b) output curves for devices consisting of DPh-BTBT (25nm) thin films with  $C_{60}F_{48}$  (12Å) deposited all over DPh-BTBT surface ( $V_{ds} = -5V$ ,  $L = 40\mu m$ ). (c) Linear field-effect mobility and (d) maximum measured drain current,  $I_{max}$  for 25nm DPh-BTBT OFETs and with  $C_{60}F_{48}$  contact doping. Values measured for different channel lengths,  $L = 30\mu m$ ,  $40\mu m$ ,  $50\mu m$ ,  $60\mu m$ ,  $80\mu m$  and  $100\mu m$ , are shown. Orange squares and green circles correspond to pristine DPh-BTBT, with 1nm  $C_{60}F_{48}$ , respectively.

Moreover, a small decrease in the  $I_{ds}$  current is observed in the output curves (Figure 5.18b). Figure 5.18c displays the field-effect mobility extracted from the transfer characteristics for six devices of different  $L$ , giving evidence that the addition of the  $C_{60}F_{48}$  layer has not had an appreciable effect on the field-effect mobility.  $C_{60}F_{48}$  neither affects the  $I_{max}$  (Figure 5.18 d)

To evaluate whether  $C_{60}F_{48}$  has or not an effect on the contact resistance, the potential drop across the electrode/channel was measured, before and after dopant deposition, by KPFM on DPh-BTBT OFETs in operation. Figure 5.19a shows the SP line profiles measured on the channel of the pristine OSC device, for different  $V_g$  values ( $V_{ds} = -5V$ ). The topography acquired in the channel region is shown in Figure 5.19b. As explained before, the device contact resistance is manifested as a voltage drop at the source ( $\Delta V_s$ ) or/drain ( $\Delta V_d$ ) contacts. As it can be seen in the SP, line profiles (shown in Figure 5.19), the electrostatic potential shows a linear decay along the channel and an

undetectable contact resistance in the device for both cases, with and without dopant.

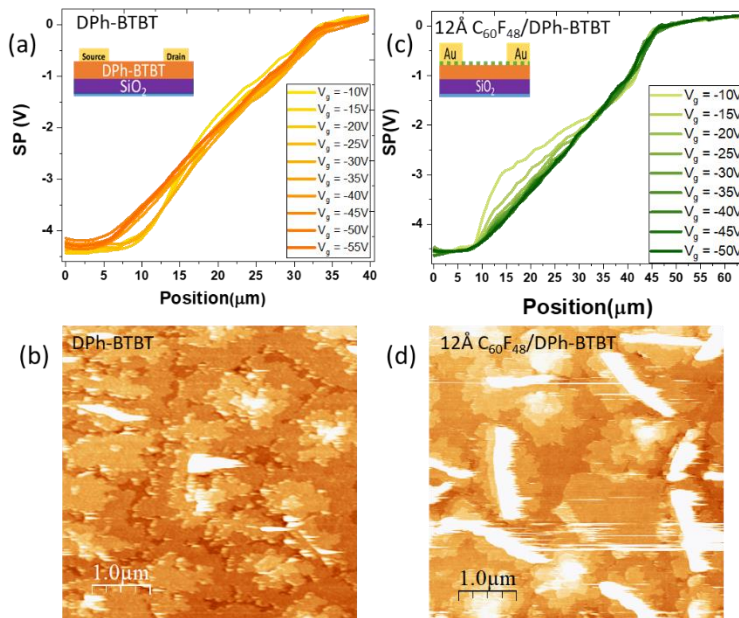


Figure 5.19. Line profiles from the surface potential map measured by KPFM on OFETs operated at  $V_{ds} = -5V$  and different  $V_g$  as indicated in the legend, and the corresponding channel topography of (a, b) bare DPh-BTBT OFET ( $L = 30\mu m$ ) and (c, d)  $C_{60}F_{48}$  (1.2nm) doped DPh-BTBT OFET ( $L = 40\mu m$ ), respectively.

This can be attributed to the lower mobility of DPh-BTBT films (one order of magnitude lower than C8-BTBT) since it determines that the total resistance is dominated by the channel resistance. Several characteristics of DPh-BTBT molecules can explain the undetectable contact resistance such as phenyl side group at the interface, extended HOMO over the phenyl group etc, leading to an efficient charge transport across the interface between the Au and DPh-BTBT. A more systematic investigation extended to other  $C_{60}F_{48}$  coverages could help to understand these results and to explore if there is an optimal coverage. Even though UPS and KPFM can be interpreted as a sign of doping in DPh-BTBT films, OFET electrical characteristics do not manifest any improvement.

In summary, a full set of nanoscale surface potential data and corresponding morphology (KPFM and AFM) combined with electronic energy analysis (UPS/XPS) and GIXD crystallographic analysis were performed. The results demonstrate the influence of the substitutional side groups in the formation of the dopant/OSC interface. Thin-film structural studies by XRD and AFM reveals that the OSC side group determines the dopant growth mode on the surface of the OSC film, hence having an impact on the interfacial morphology and work function distribution across the surface. For heterogeneous surfaces, KPFM provides the local work function information with nanoscale accuracy. The investigation of the energy level shifts in BTBT molecules indicates integer charge transfer from HOMO of BTBT molecules to the LUMO of C<sub>60</sub>F<sub>48</sub>. Both KPFM and UPS demonstrate the formation of a larger surface dipole for C8-BTBT, a fact that seems to be related to its lower IP. Lastly, the OFET parameters were examined for DPh-BTBT OFETs. Contact doping with C<sub>60</sub>F<sub>48</sub> is more effective for C8-BTBT OFETs than DPh-BTBT OFETs.



## 6. F6TCNNQ on C8-BTBT

This chapter presents the study of the evolution of the thin film structure and electronic levels of C8-BTBT thin film during the deposition of F6TCNNQ. The results are submitted to the *ACS materials and interfaces* for publishing; Copyright 2022 American Chemical Society.

To complement the study with the bulky, spherical  $C_{60}F_{48}$  molecular dopant, discussed in the previous chapters, a new dopant molecule, F6TCNNQ with similar electron affinity but with a planar shape is chosen to study the influence of the structure of the dopant molecule in the doping mechanism.

### 6.1. Co-crystal formation during F6TCNNQ deposition

To monitor if any structural change taking place at the dopant/OSC interface, GIXD measurements were taken in real-time during the growth of F6TCNNQ on a 30nm thick C8-BTBT film previously grown on 40nm CYTOP/100nm  $SiO_2$  (typical dielectric materials used in OFETs). To minimize radiation damage during synchrotron radiation measurements, the sample was laterally displaced after an exposure time of around 10sec of data collection. In-situ



GIXD experiments were performed using an incident angle of  $0.11^\circ$  (lower than the critical angle of the silicon substrate,  $0.159^\circ$ ).

Figure 6.1a shows the out-of-plane diffraction spectra from the organic film, acquired during the initial stages of the F6TCNNQ deposition, every  $0.4\text{\AA}$  and up to nominal coverage of  $35\text{\AA}$ . The most striking observation is the continuous increase in intensity around  $q_z = 3.3\text{nm}^{-1}$  from the very initial stages of deposition, which corresponds to an inter-planar spacing of  $1.9\text{nm}$ . Interestingly, there are no diffraction peaks reported around this value ( $q_z = 3.3\text{nm}^{-1}$ ), neither for F6TCNNQ nor for C8-BTBT structures.<sup>[29],[71],[50]</sup> As explained in section 2.6, BTBT derivative molecules may form co-crystals with both, F4TCNNQ and F6TCNNQ molecules.<sup>[45],[146],[147]</sup> The formation of a co-crystal is held by the interaction of the acceptor with the BTBT conjugated core resulting in two-dimensional layers with an alternate  $\pi$ -stacking of BTBT and the dopant.

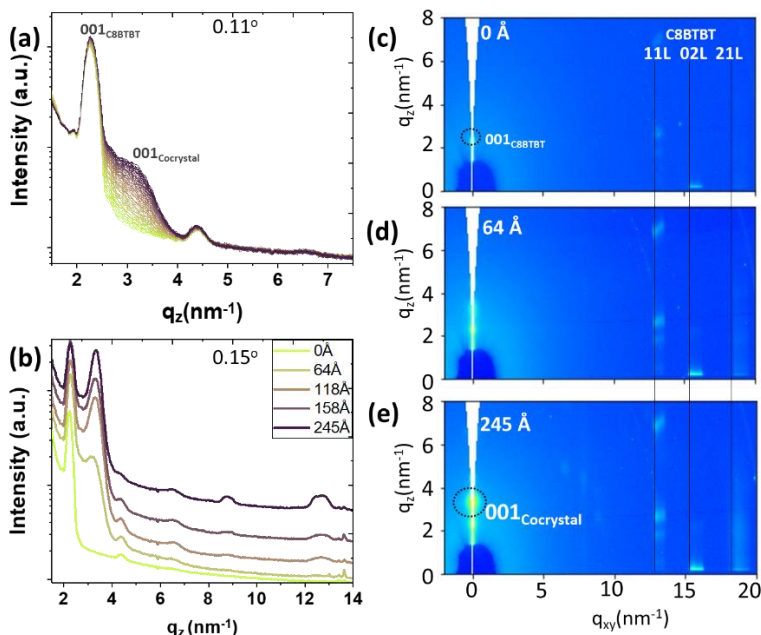
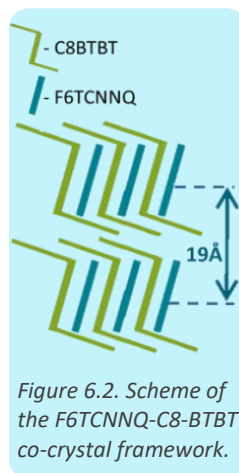


Figure 6.1. Out-of-plane GIXD spectra during the deposition of F6TCNNQ on top of a 30nm thick C8-BTBT film: (a) From 0 up to  $35\text{\AA}$  for an incident angle of  $0.11^\circ$  (b) for selected coverages of F6TCNNQ for an incident angle of  $0.15^\circ$ . (c) 2D GIXD pattern of a 30nm thick C8-BTBT film on 40nm CYTOP/100nm  $\text{SiO}_2$  and selected 2D GIXD patterns for F6TCNNQ coverages of (d)  $64\text{\AA}$  and (e)  $245\text{\AA}$ , for an incident angle of  $0.11^\circ$ .

The core is vertically separated by tilted alkyl chains of the C8-BTBT molecules as shown schematically in Figure 6.2. The new peak is attributed to the diffracted intensity between (00L) planes of the F6TCNNQ-C8-BTBT co-crystal. Figure 6.1b shows selected out-of-plane spectra obtained from the 2D maps of GIXD for larger coverages of F6TCNNQ. In this case, we have selected an incident angle of  $0.15^\circ$ , larger than the critical angle of OSC films, to probe the whole thin film thickness. The peak attributed to the F6TCNNQ-C8-BTBT co-crystal at  $q_z = 3.3\text{nm}^{-1}$  further increases in intensity with F6TCNNQ coverage and, eventually, a well-developed peak is seen. Figure 6.1c, d, and e display the 2D GIXD patterns for the pristine C8-BTBT film and the same film after depositing  $65\text{\AA}$  and  $245\text{\AA}$  of F6TCNNQ, respectively. The 2D GIXD pattern for the pristine film (Figure 6.1c) exhibits the expected diffraction intensities at  $q_{xy} \sim 13.1\text{nm}^{-1}$ ,  $q_{xy} \sim 15.7\text{nm}^{-1}$  and  $q_{xy} \sim 18.8\text{nm}^{-1}$ , assigned to (11L), (02L), and (12L) planes of C8-BTBT and (00L) Bragg reflections along  $q_z$  ( $q_z = 2.1\text{nm}^{-1}$ ). Along with the structural fingerprint of C8-BTBT, diffraction features corresponding to the co-crystal are clearly visible in the 2D pattern for  $245\text{\AA}$  of F6TCNNQ deposited on top of the C8-BTBT film (dotted circle in Figure 6.1e). The spot-like shape of the (00L) Bragg peaks for both, C8-BTBT and co-crystal, indicates a pronounced (001) fibre texture, i.e., highly ordered crystalline planes.

As observed in Figure 6.1b, a new peak starts to emerge at  $q_z = 12.6\text{nm}^{-1}$  and another at  $q_z = 8.6\text{nm}^{-1}$  for large F6TCNNQ coverages ( $> 150\text{\AA}$ ) that corresponds to the reported crystalline structure of F6TCNNQ.<sup>[71]</sup> This result indicates that, at higher coverages, F6TCNNQ crystallites coexist with the crystalline C8-BTBT and the formed co-crystals. Further insight into the spatial distribution of each of these structures can be revealed by probing the film at a different incident angle, i.e., at a condition with more penetration depth. Figure 6.3a shows the out-of-plane peaks obtained at different incident angles, from  $0.10^\circ$  to  $0.15^\circ$ , for the case of  $245\text{\AA}$  of F6TCNNQ on a  $30\text{nm}$  thick C8-BTBT film on CYTOP/SiO<sub>2</sub>. The different relative ratio of the Bragg peaks corresponding to C8-BTBT, F6TCNNQ and co-crystal for different incident angles indicates that each one is differently distributed along the vertical direction, i.e., across the film thickness. For example, the F6TCNNQ peak at  $q_z = 12.6\text{nm}^{-1}$  is more prominent at lower incident angles, which implies that F6TCNNQ crystallites are mostly located at the topmost surface of the film. At lower incident angles, C8-BTBT and co-crystal Bragg peaks have a similar intensity while for higher incident angles, the co-crystal Bragg peak is lower than that of C8-BTBT. This fact indicates that the bottom part of the film (at the interface with the dielectric substrate) consists of crystalline C8-BTBT and the co-crystals are on top of them. Besides, Figure 6.3b and c provide the  $(001)_{\text{co-crystal}}$  peak and F6TCNNQ peak as a function of the F6TCNNQ coverage,



respectively. The evolution of the co-crystal Bragg peak intensity points to progressive vertical growth of a layered structure with a spacing of 1.9nm. The co-crystal grows steadily from the early stage of the deposition. The growth slows down for an F6TCNNQ coverage larger than 150Å.

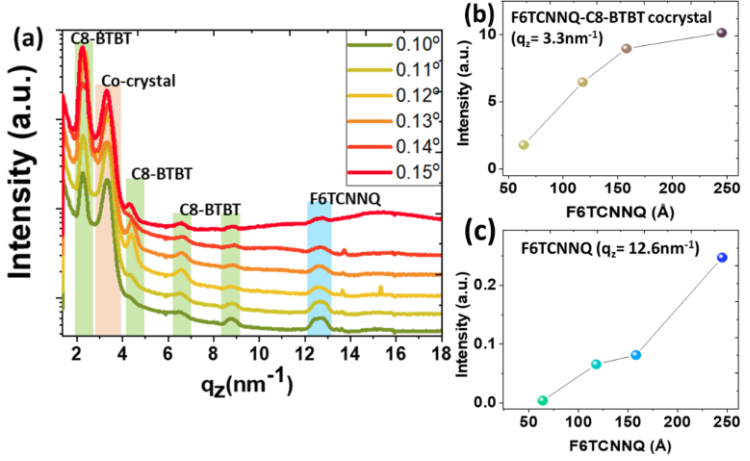
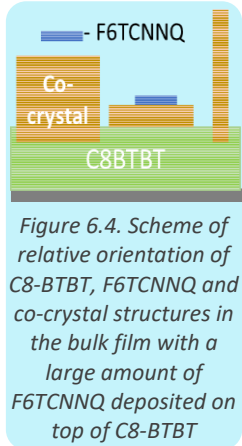


Figure 6.3. (a) Out-of-plane diffraction spectra for different incident angles (0.10°, 0.11°, 0.12°, 0.13°, 0.14°, 0.15°) for 245Å F6TCNNQ deposited on top of the C8-BTBT film. (b) Intensity of the (001)<sub>co-crystal</sub> peak (incident angle 0.1°) and (c) intensity of the 001<sub>F6TCNNQ</sub> peak (incident angle 0.15°) for increasing coverages of F6TCNNQ on C8-BTBT.

The mean value of the vertical coherence length estimated from the full width at half maximum of the (001)<sub>co-crystal</sub> peak is  $L_c \sim 18$ nm, for the largest F6TCNNQ coverage (245Å). Moreover, the Bragg peaks from C8-BTBT do not decrease in intensity as a function of dopant deposition indicating that most of the C8-BTBT structures that contribute to the Bragg peak are not affected by the co-crystal formation. During the first stages of co-crystal formation part of the C8-BTBT molecules are displaced, which would remain on the surface ready to react with newly impinging F6TCNNQ. The number of C8-BTBT molecules available at each stage on the surface would depend on the diffusion and mass transport properties of the system, but it surely decreases with deposition time and eventually, the reaction will stop. From that moment on, the excess of F6TCNNQ will nucleate to form pure F6TCNNQ crystallites.

Because the morphology of the film is relevant for understanding the interfacial structural properties, AFM measurements were taken on C8-BTBT films with different coverages of F6TCNNQ. Figure 6.5a and b show the



topography and the lateral force map of the sample grown during the GIXD experiments, i.e., with the final F6TCNNQ coverage (245Å).

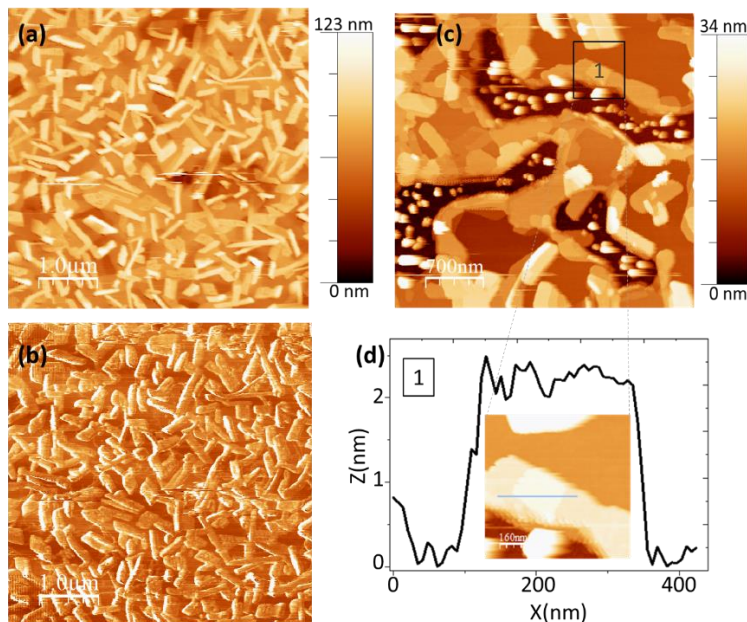


Figure 6.5. (a) Topography and (b) the corresponding lateral force map of 245Å F6TCNNQ deposited on a 30nm thick C8-BTBT film (sample grown during the GIXD measurements). (c) Topography of 20Å F6TCNNQ on a 6nm thick C8-BTBT film and (d) line profile from the area marked as 1 in (c) and shown magnified in the inset.

The average height of the crystallites is 20nm, in agreement with the coherence length estimated from the co-crystal Bragg peak. This result shows that the co-crystals are on the surface. The taller (large aspect ratio) aggregates (height > 20nm), with irregular shapes, are attributed to F6TCNNQ. The darker region in the lateral force is attributed to the surface of the C8-BTBT film that remains uncovered. This scenario consisting of F6TCNNQ-C8-BTBT co-crystals on the surface is consistent with the GIXD data. To obtain details on the interfacial morphology, the initial stages of deposition must be analysed. Figure 6.5c shows the topography of 2nm F6TCNNQ on 6nm C8-BTBT film. In this case, C8-BTBT islands leave substrate areas uncovered (lower level in the image). While the clusters observed on the native SiO<sub>2</sub> can be attributed to polycrystalline F6TCNNQ as reported by

Duva *et. al.*<sup>[67]</sup> On the C8-BTBT islands edges 3nm thick layers with rectangular flat regions about  $\sim 2$ nm high on their top are observed. A value that agrees with the inter-planar distance of the F6TCNNQ-C8-BTBT co-crystals as obtained from the corresponding Bragg peaks (mentioned earlier in this section).

In summary, the results from GIXD and the AFM morphological analysis are fully consistent and demonstrate the spontaneous co-assembly of C8-BTBT and F6TCNNQ into F6TCNNQ-C8-BTBT co-crystals. The nearly rectangular shape and flat surface of the first co-crystal formation indicate the abruptness of the interface formed.

## 6.2. Charge transfer complex formation

In order to know about the electronic characteristics of the co-crystal, in particular, elucidating whether it behaves or not as a charge-transfer complex, UV-Vis absorption spectroscopy was performed. Figure 6.6 shows the absorption spectra of a series of 35nm C8-BTBT thin films with the different amounts of F6TCNNQ deposited on their top.

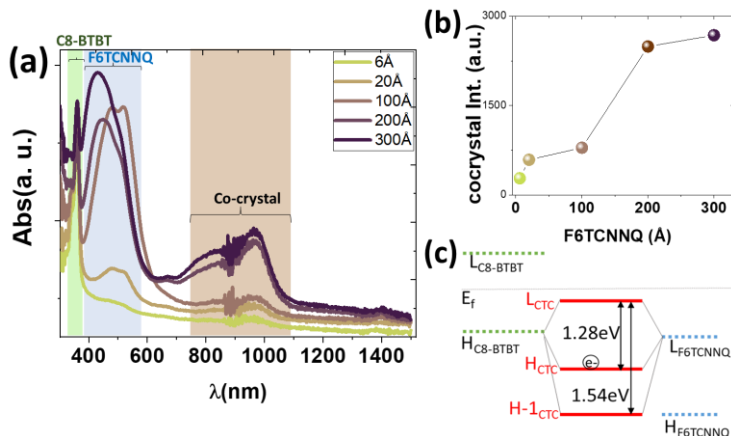


Figure 6.6. (a) UV-Vis absorption spectra for C8-BTBT films with increasing coverages of F6TCNNQ on top. Absorption peaks from different molecular species (C8-BTBT, F6TCNNQ and co-crystal) are labelled. (b) evolution of co-crystal peak area vs. F6TCNNQ coverage. (c) Scheme illustrating the formation of charge-transfer complex co-crystals due to frontier orbital hybridization of C8-BTBT and F6TCNNQ.

The observed absorption peak at  $\sim 360\text{nm}$  and the double peak at  $\sim 500\text{nm}$  is consistent with the reported absorption peaks of C8-BTBT ( $360\text{nm}$ ) and F6TCNNQ ( $468\text{nm}$ ,  $517\text{nm}$ ).<sup>[42],[148]</sup> The intensity of the absorption peak of F6TCNNQ increases with coverage. In addition, a set of new peaks around  $807\text{nm}$  and  $960\text{nm}$  (range of  $\lambda$  highlighted in brown) emerged and increase as well with F6TCNNQ coverage. The evolution of the new peaks is shown in Figure 6.6b. Interestingly, the trend of the intensity is similar to the evolution of the co-crystal Bragg peak (Figure 6.3) reaching saturation after  $200\text{\AA}$  of F6TCNNQ. As explained in section 2.3, there are two widely accepted doping mechanisms; Ion-pair formation by integer charge transfer (ICT) and the formation of charge-transfer complex (CTC). The absence of the F6TCNNQ<sup>-</sup> anion peak (expected around  $1140\text{nm}$ )<sup>[69],[149]</sup> rules out integer charge transfer between molecules. Absorption peaks near the IR region are characteristics of transitions between the frontier hybrid orbitals of charge transfer complexes, formed inside the energy gap of the OSC. Hence, the three peaks at  $646\text{nm}$ ,  $807\text{nm}$ , and  $960\text{nm}$  emerging and increasing with F6TCNNQ coverage are ascribed to the charge transfer complex in the formed F6TCNNQ-C8-BTBT co-crystals. Indeed, CTC formed between C10-BTBT and F6TCNNQ has been reported.<sup>[45]</sup> As in the F6TCNNQ-C10-BTBT co-crystal case, here there are two absorption peaks corresponding to the CTC due to the transitions from  $\text{HOMO}_{\text{CTC}}$  to the  $\text{LUMO}_{\text{CTC}}$  and  $\text{HOMO}-1_{\text{CTC}}$  to the  $\text{LUMO}_{\text{CTC}}$ . This is illustrated in Figure 6.6c. The bandgap of F6TCNNQ-C8-BTBT CTC, calculated from the absorption peak is  $1.28\text{eV}$ . Surprisingly, both neutral F6TCNNQ absorption peaks and F6TCNNQ-C8-BTBT co-crystal peaks were observed, even for low coverages of F6TCNNQ, which suggests the co-existence of non-crystalline neutral F6TCNNQ along with the co-crystals in the film.

Electronic level modification of C8-BTBT films was investigated by UV photoelectron spectroscopy (UPS). Figure 6.7 shows the evolution of frontier orbitals of C8-BTBT thin film during the preliminary stages of F6TCNNQ deposition on top. The work function of the system is increasing as F6TCNNQ is deposited on the surface. However, the largest shift is observed for the smallest F6TCNNQ coverage ( $6\text{\AA}$ ) of  $0.9\text{eV}$ , which later shifted by  $0.2\text{eV}$  with each deposition. The HOMO-onset of the UPS shifted to a lower BE for the lowest dopant coverage, which later on move towards a higher BE with further F6TCNNQ deposition. Also, an increased intensity was observed at  $1.58\text{eV}$  with onset at  $1.09\text{eV}$  (indicated in red in Figure 6.7c) in the energy gap region between the HOMO and the Fermi level. It is being reported that the gap states emerge due to charge transfer at the interface.<sup>[135],[139],[43],[150]</sup> As depicted in Figure 6.6c, the  $\text{HOMO}_{\text{CTC}}$  is expected at higher binding energy (deeper) than the  $\text{HOMO}_{\text{C8-BTBT}}$  whereas the  $\text{LUMO}_{\text{CTC}}$  is expected to be

located above. The LUMO<sub>CTC</sub> is lower than the pristine HOMO<sub>C8-BTBT</sub>, hence electron transfer from the HOMO of C8-BTBT to LUMO<sub>CTC</sub> is energetically favourable and results in a filled LUMO<sub>CTC</sub> (Figure 6.7).

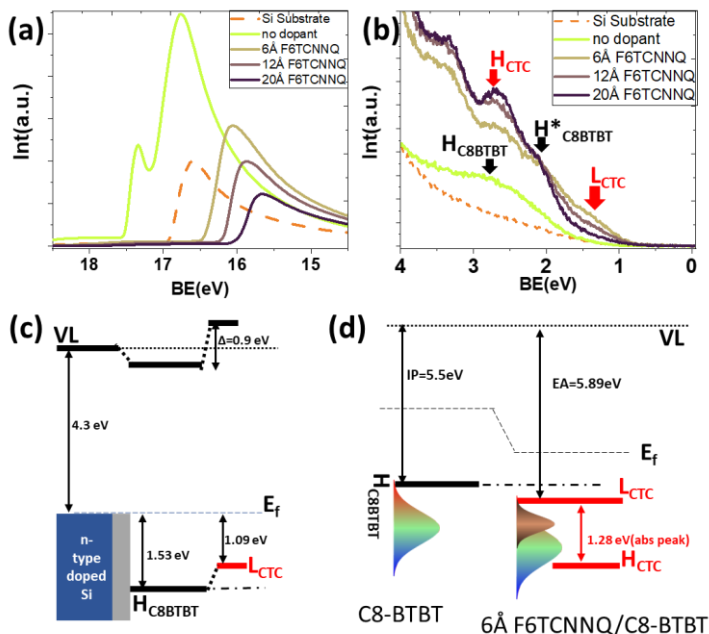


Figure 6.7. UPS spectra of the (a) secondary electron cut-off region (SECO) of the film and (b) HOMO of C8-BTBT for increasing coverages of F6TCNNQ from 0Å to 20Å on top of a 12nm thick C8-BTBT film. (c) Scheme illustrating the VL shift from the evolution of SECO and HOMO of C8-BTBT with increasing coverage of F6TCNNQ and co-crystal development. (d) Scheme displaying relative energy level (VL aligned) of F6TCNNQ-C8-BTBT CTC formed and its filled LUMO<sub>CTC</sub>.

Therefore, the increased intensity at low BE is consistent with the filling of LUMO<sub>CTC</sub>, which results in the formation of holes in the C8-BTBT (p-type doping). The doping due to the formation of a CTC was proposed by Mendez *et al.*<sup>[43]</sup> It can be observed that the LUMO<sub>CTC</sub> peak arises during the earliest stage of F6TCNNQ deposition but later diminishes with further deposition of the dopant. Since UPS is a surface-sensitive technique, this observation is the result of intensity attenuation by material accumulation on top during the further deposition, confirming that the filled LUMO<sub>CTC</sub> is an interfacial state. The peak located at  $\approx 2.7$  eV is attributed to the HOMO<sub>CTC</sub>.

The inhomogeneity of the work function along the C8-BTBT film surface has also been explored by Kelvin probe force microscopy (KPFM). Figure 6.8 shows the topography and simultaneously measured surface potential map of 2nm F6TCNNQ deposited on top of a 6nm thick C8-BTBT film.

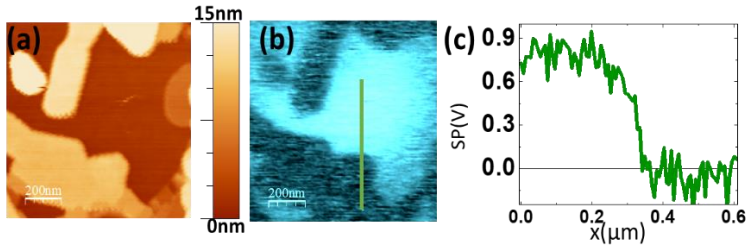


Figure 6.8. (a) Topography and the (b) corresponding surface potential map of the thin film with 2nm thick F6TCNNQ on 6nm thick C8-BTBT (c) measured SP along the green line indicated in the SP map.

The lower level in the topography is the C8-BTBT layer surface and the bright islands are the co-crystal formed on top (as explained in section 6.1). The corresponding surface potential map (Figure 6.8b) shows a lower (darker) surface potential on the co-crystal islands than on the surrounding C8-BTBT layer. Figure 6.8c shows the surface potential profile along with the co-crystal islands and the uncovered C8-BTBT, the SP difference is around 0.9V, which is consistent with the work function shift observed by UPS.

The next section presents the investigation of the impact of the formation of mixed co-crystal on the electrical properties of C8-BTBT OFETs.

### 6.3. Surface doping of C8-BTBT OFET by CTC

Bottom-gate, top-contact OFET architecture (BG-TC), with different coverages of F6TCNNQ (nominal thickness) deposited on top of a 35nm-thick C8-BTBT film was employed for this study. Figure 6.9a and b show the representative transfer curves of the C8-BTBT OFETs under linear regime operation for the different coverages of F6TCNNQ. The SiO<sub>2</sub>/OSC interface is very prone to defects that act as charge traps and result in a negative threshold voltage. To avoid this problem, C8-BTBT films were grown on 40nm CYTOP/100nm SiO<sub>2</sub> substrates and on top, different coverages of F6TCNNQ molecules were deposited. There is a clear shift of  $V_{on}$  towards positive gate



voltage as well as an increase in  $I_{off}$  with the increase in the amount of F6TCNNQ (as demonstrated in Figure 6.9c). This indicates the presence of holes in the OSC matrix, which means the film has been doped. The current measured at  $V_g = 0V$  is proportional to the conductivity of the film, and it is increasing. Hence, the F6TCNNQ-C8-BTBT co-crystals increase the conductivity of the film, which is an indication of the presence of mobile charge carriers due to doping in the organic semiconductor.

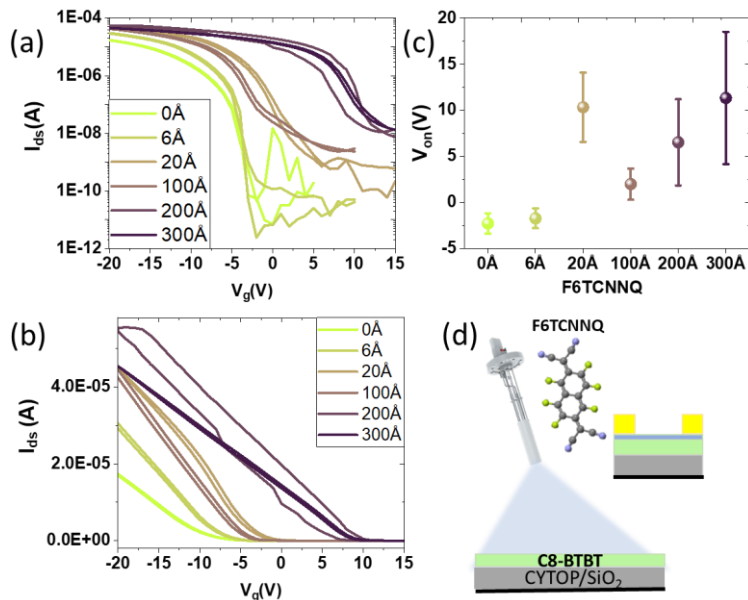


Figure 6.9. Transfer curves at  $V_{ds} = -5V$ , in (a) linear and (b) logarithmic scales for C8-BTBT (35nm) OFETs ( $L = 180\mu m$ ) with different coverage of F6TCNNQ deposited on top. (c) Average  $V_{on}$  voltage, extracted from the transfer curves for each F6TCNNQ coverage for fifteen devices, the error bar corresponds to the standard deviation. (d) Scheme of F6TCNNQ deposition on C8-BTBT films.

Figure 6.10 shows the evolution of the mobility of C8-BTBT OFETs with an increase in the amount of F6TCNNQ deposited on top. The decrease in the slope of transfer curves plotted in a linear regime, conveys the effect of decreasing mobility. The observation of mobility improvement with the dopant deposition was verified by measuring fifteen devices for each coverage. The average mobility (Figure 6.10a) of the doped devices increases and acquires a maximum value for an F6TCNNQ coverage of 100Å. Beyond this coverage, it is decreasing. The individual values of the mobility for

different channel lengths are shown in Figure 6.10b-f. The occurrence of a maximum value of mobility for C8-BTBT OFET with 100Å F6TCNNQ is observed for all channel lengths.

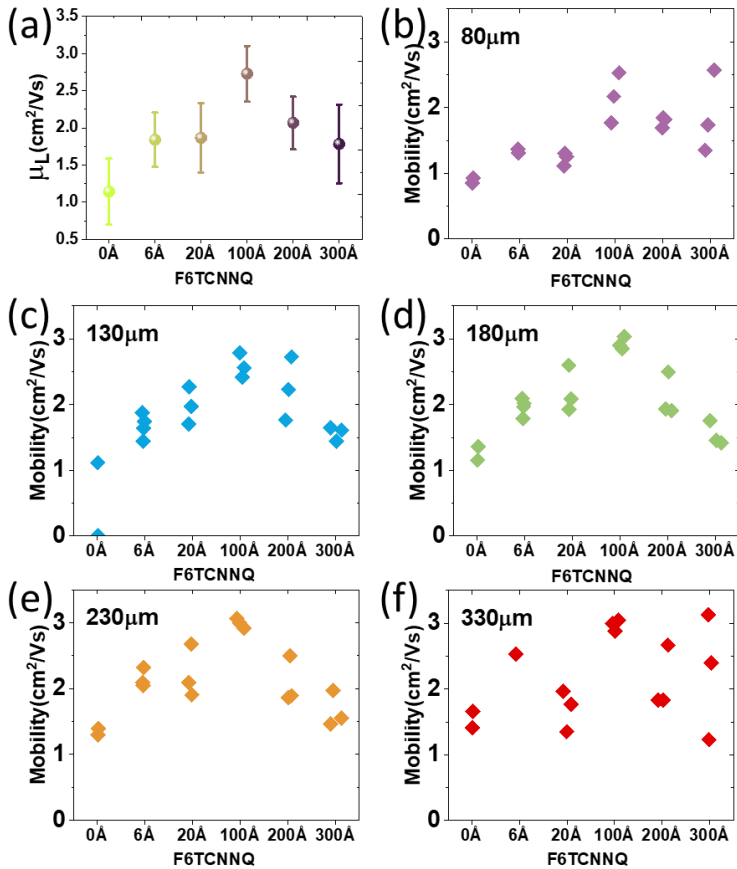


Figure 6.10. (a) Evolution of average mobility, extracted from the transfer curves of C8-BTBT OFETs with respect to F6TCNNQ coverage, for fifteen devices and the error bar corresponds to the standard deviation. (b-f) Measured mobility values of C8-BTBT OFETs with different channel lengths. The channel length for each set of OFETs is indicated on the top left corner of each graph.

Similar behaviour is observed in the drain current measured from the output curves. Figure 6.11 shows the representative output curves, obtained from the same samples corresponding to the transfer curves in Figure 6.9. The

obtained drain current for any combination of  $V_{ds}$  and  $V_g$  is higher for a device with 100Å of F6TCNNQ.

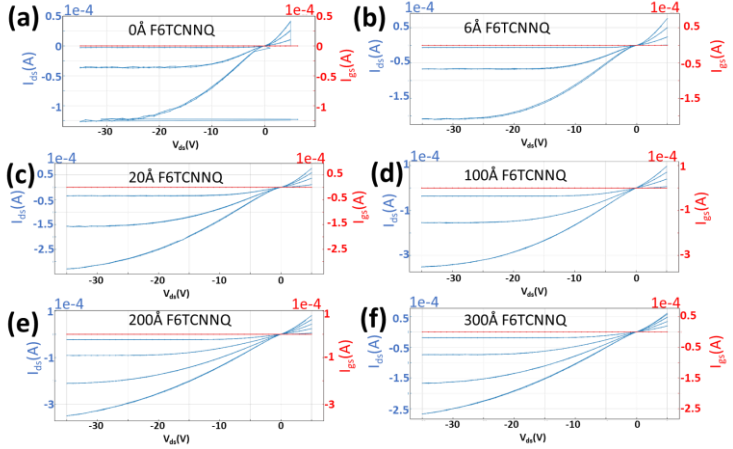


Figure 6.11. Output curves (for  $V_g = 0V, -10V, -20V, -30V$ ) of C8-BTBT OFETs of 180 $\mu m$  channel length with different coverages (indicated in the graph) of F6TCNNQ deposited all over on C8-BTBT layer.

The increase in mobility and drain current is consistent with the growth of the co-crystal as demonstrated by XRD and UV-Vis absorption spectra, which also show a saturation after deposition of 150Å of F6TCNNQ. Hence, the increased improvement in OFET performance with increasing coverage of F6TCNNQ up to 100Å can be attributed to the formation of the F6TCNNQ-C8-BTBT CTC co-crystals. Further deposition of F6TCNNQ results in the crystallization of accumulated and unreacted F6TCNNQ molecules. In the BG-TC device geometry, the F6TCNNQ molecules are deposited before i.e., they are under the gold electrodes. Hence the decrease in the C8-BTBT OFET performance with larger coverages of F6TCNNQ can be attributed to the energy barrier created by crystalline F6TCNNQ at the contact, which may increase the contact resistance of the OFETs.

To evaluate if the F6TCNNQ-C8-BTBT co-crystal influence the contact resistance, another set of samples with F6TCNNQ deposited only on the channel region, i.e., on top of the C8-BTBT film with gold contacts, were fabricated. Figure 6.12a shows the comparison of the linear transfer curve of C8-BTBT OFETs with 2nm of F6TCNNQ deposited only in the channel region (green line) and all over the surface (orange line). For the first case, the  $V_{on}$  shifted towards a negative gate voltage and the kink in the transfer

characteristic near  $V_{on}$  disappear. However, a similar value of the slope of the transfer curve at larger gate voltages for both devices indicates similar charge mobility. Figure 6.12b shows the values for the average mobility extracted for fifteen devices for each case.

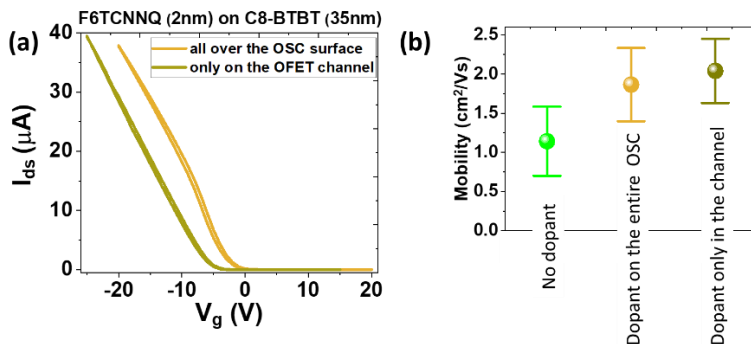


Figure 6.12. (a) Transfer curve ( $V_{ds} = -5V$ ) for C8-BTBT OFET (230 $\mu m$  channel length) with 2nm of F6TCNNQ (avocado green) only in the channel and (orange) all over the C8-BTBT layer both at the Au/C8-BTBT interface and in the channel. (b) The average mobility for fifteen devices and error bars are the standard deviations.

This result indicates that, unlike contact doping by  $C_{60}F_{48}$ , the enhancement in the mobility of C8-BTBT OFETs mainly arises from the channel doping by F6TCNNQ-C8-BTBT co-crystal formation.

To understand the effect of channel doping, BG-BC C8-BTBT (150 $\text{\AA}$ ) OFET were measured in situ, under vacuum, while depositing 55 $\text{\AA}$  of F6TCNNQ on top. 50nm Au was deposited on a 200nm thick  $SiO_2$ , which is the gate dielectric, using a shadow mask that gives a 400 $\mu m$  channel length. To reduce the difference in surface energy between Au and  $SiO_2$ , perfluorodecanthiol was used as a self-assembled monolayer (SAM) on  $SiO_2$ . Later, C8-BTBT molecules were deposited and we measured the OFET characteristics of the pristine film. Finally, F6TCNNQ molecules were deposited on top and we simultaneously measure the transfer curves. Note that measuring the same device during the deposition avoids sample-to-sample variation. Figure 6.13a shows the real-time measurement of the transfer curves during the F6TCNNQ deposition. For pristine C8-BTBT OFET, a negative  $V_{on}$  is observed, which indicates the presence of fixed traps at the dielectric/OSC interface.

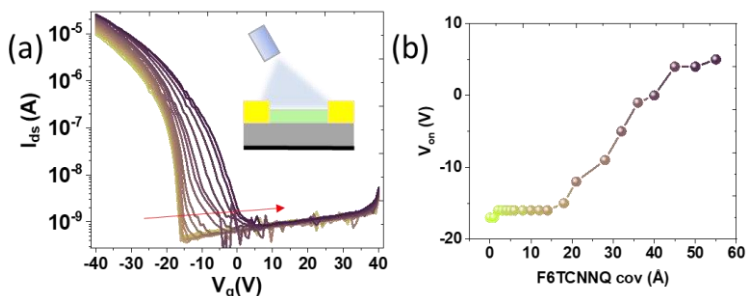
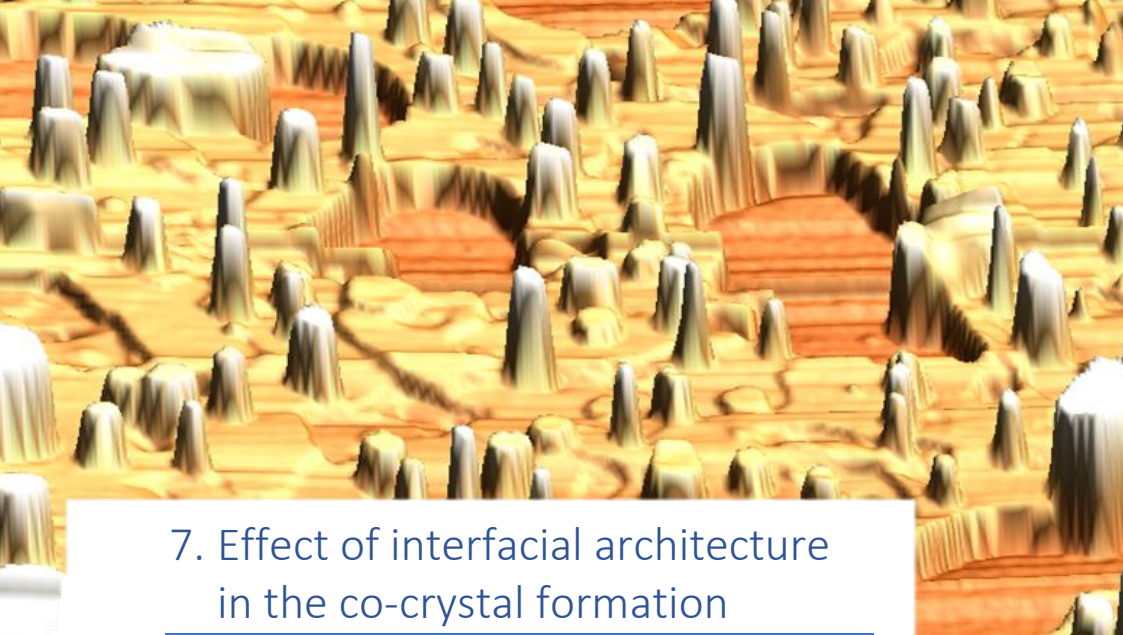


Figure 6.13. (a) Evolution of the transfer curve ( $V_{ds} = -5V$ ) for BG-BC C8-BTBT OFET acquired in-situ in the vacuum chamber during the deposition of F6TCNNQ and (b) the corresponding change in  $V_{on}$  voltage vs. amount of F6TCNNQ deposited on the surface (nominal thickness from the quartz monitor). The inset of (a) shows the scheme of the BG-BC device architecture ( $L = 400\mu m$ ).

We note that it has been reported that the passivation of these traps can shift the  $V_{on}$  towards a less negative value.[6],[151],[152],[153] As the F6TCNNQ deposition progresses, the co-crystal grows on the surface, resulting in a shift of  $V_{on}$  from  $-16V$  to  $5V$  (Figure 6.13b) without changing the  $I_{off}$  current. This result indicates that the CTC co-crystal on the surface acts as a dopant and induces free carriers in the film, passivating the traps at the dielectric/OSC interface.

The results discussed in this chapter confirm that the surface doping by CTC allows fine tunability of the  $V_{on}$  for a range of 20V, via controlling the amount of co-crystal formed on the surface, without a drastic change in mobility. It also suggests that surface doping with CTC co-crystal can be used as a post-fabrication treatment to achieve the desired  $V_{th}$  for OFETs. In summary, combining the results from XRD, AFM, UV-Vis absorption and UPS confirms that the F6TCNNQ-C8-BTBT co-crystal on the surface is doping the whole C8-BTBT film. The evolution of the structure and the electronic levels are consistent with the electrical characteristics of the OFETs, indicating that the growth of CTC co-crystals at the C8-BTBT surface serves as a p-type dopant for the C8-BTBT film. As the F6TCNNQ-C8-BTBT CTC co-crystals grow, the number of mobile holes in the channel increases, causing threshold voltage shift towards a positive gate value and an increased  $I_{off}$  current. The growth of the co-crystals does not disturb the microstructure of the underlying C8-BTBT film and thus can be used to reduce  $V_{on}$  without trading other OFET parameters.



## 7. Effect of interfacial architecture in the co-crystal formation

---

This chapter tries to elucidate the factors that affect the formation and degree of ordering of CTC co-crystals. Firstly, a discussion of the effect of temperature is presented. An increase in temperature increases the energy of the molecules and affects the molecular interactions at the interface. Secondly, we discuss the order of deposition of the C8-BTBT and F6TCNNQ, which can lead to significant changes in the interfacial morphology. Finally, we study the effect of the OSC side group by depositing F6TCNNQ on top of DPh-BTBT.

### 7.1. Role of temperature

#### 7.1.1. Impact of thermal annealing on the structure

In this section, the effect of post-annealing treatments on the heterostructure films fabricated by the sequential deposition of C8-BTBT and F6TCNNQ is addressed. Out-of-plane XRD and GIXD measurements (Figure 7.1) were performed at the Soleil synchrotron facility in France. The samples were grown at room temperature and characterized in-situ. Since the growth chamber did not have a quartz monitor microbalance to measure the thickness, the thickness of the C8-BTBT film was estimated to be 37nm from the Kiessig fringes (inset in Figure 7.1b). The observed Laue oscillations

indicate the presence of coherent domains of C8-BTBT in the film. The thin-film structure of C8-BTBT molecules on SiO<sub>2</sub> at RT and higher temperatures have been already discussed in section 4.3.

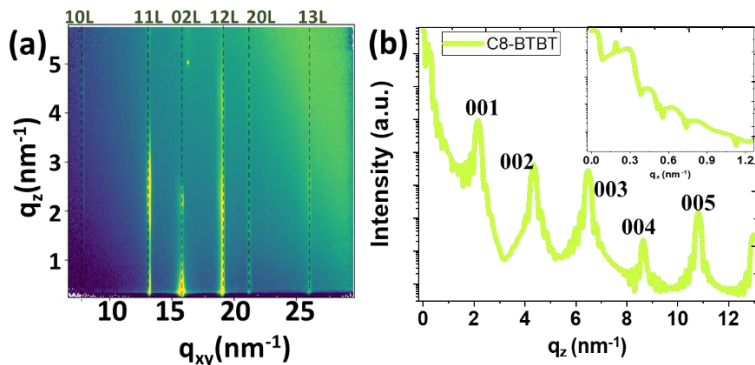


Figure 7.1. (a) 2D GIXD pattern and (b) out-of-plane XRD of pristine C8-BTBT at RT. The inset of b shows the Kiessig fringes used to estimate the film thickness.

The structural data obtained after the deposition of F6TCNNQ on the same film is shown in Figure 7.2. Surprisingly, the presence of F6TCNNQ crystallites is visible at RT. The OOP diffraction data shows the peak at  $q_z \sim 12.6 \text{ nm}^{-1}$  corresponding to the structure of F6TCNNQ as observed before (section 6.1). The 2D pattern exhibits new diffraction features, although only a few of them can be indexed according to the reported F6TCNNQ bulk structures. The diffraction spots at  $|q| = 18.7 \text{ nm}^{-1}$  and  $|q| = 20.2 \text{ nm}^{-1}$  coincide with the F6TCNNQ form I structure reported by Dasari et al.<sup>[154]</sup> It is possible that F6TCNNQ forms different polymorphs. There is no CTC co-crystal Bragg peak observed in the OOP data. Even though scattering intensity at  $q_{xy} = 18.66 \text{ nm}^{-1}$  is observed (denoted by a vertical red dash-dotted line in Figure 7.2a, b), which corresponds to an in-plane spacing of  $3.3 \text{ \AA}$ , attributed to the  $\pi$ - $\pi$  orbital mediated stacking of the mixed co-crystal. This diffraction feature was previously observed, although with a less in-plane resolution, in Figure 6.1. The fact that the intensity extends along the  $q_z$  direction, i.e., rod-shaped intensity, indicates that it is a 2D surface structure i.e., the co-crystal forms on the surface.

The films were post-annealed under vacuum for 4 minutes at the given temperature and measured after cooling down to RT. Figure 7.2b shows the 2D diffraction patterns, after annealing at  $60^\circ\text{C}$ . The co-crystal (001) peak at  $q_z \sim 3.3 \text{ nm}^{-1}$  appears in the OOP data (Figure 7.2c), indicating that the co-

crystalline structure develops in the vertical direction. The coherence length obtained from the FWHM of the peak is  $L_c = 4.5\text{nm}$ .

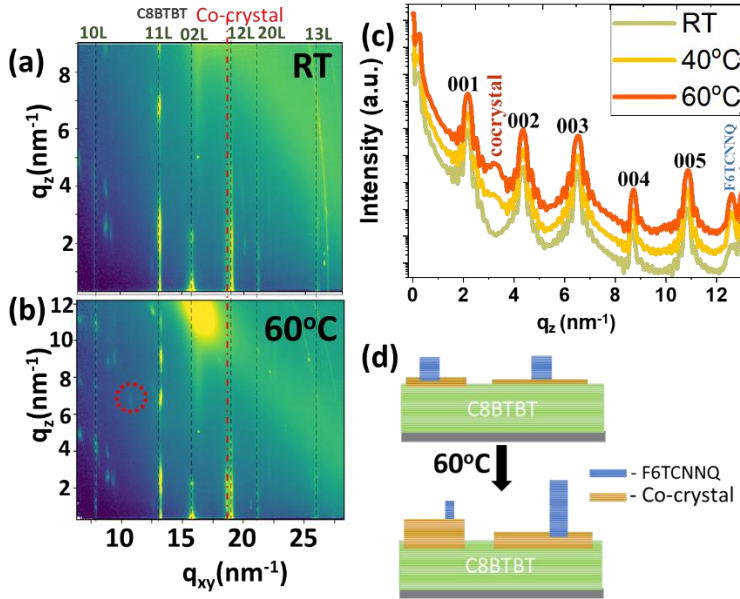


Figure 7.2. 2D GIXD pattern of the heterostructure formed by F6TCNNQ deposited on C8-BTBT (a) at RT and (b) after annealing at 60°C. (c) Out-of-plane, XRD was measured after annealing at 40°C and 60°C (as indicated in the legend). (d) Cartoons illustrating the changes in the film during annealing.

In addition, the 2D diffraction pattern shows the development of intensity at  $q_{xy} \sim 7\text{nm}^{-1}$  with a regular pattern along  $q_z$  ( $q_z \sim 5\text{nm}^{-1}$ ,  $8\text{nm}^{-1}$  and  $10.5\text{nm}^{-1}$ ). This rod is assigned to the (01L) rod of the co-crystal. Moreover, the intensity distribution of the diffraction feature at  $q_{xy} = 18.66\text{nm}^{-1}$  has acquired a pattern along  $q_z$ , which supports the change from the 2D to the 3D structure of the co-crystal. The signature of crystalline F6TCNNQ at  $q_z \sim 12.6\text{nm}^{-1}$  remains visible. From the FWHM ( $\Delta q = 0.2\text{nm}^{-1}$ ) of this peak, a coherence length of  $L_c = 31\text{nm}$  is estimated, suggesting the development of the F6TCNNQ island on the surface.

To understand the interfacial morphology modification after mild annealing, AFM measurements were done on the same sample. The topography and corresponding lateral force image of the same film after annealing at 60°C are shown in Figure 7.3.



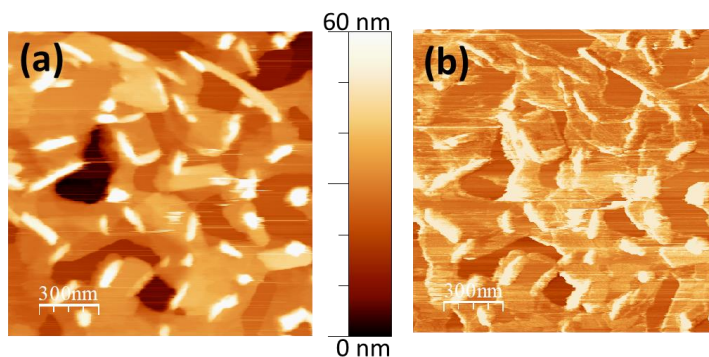


Figure 7.3. (a) Topography and the (b) corresponding lateral force map of thin film with F6TCNNQ on C8-BTBT annealed after 60°C.

The taller structures have an elongated aspect-ratio morphology (needle), with lengths of several hundred nm and heights that vary between 25nm and 40nm, consistent with the estimated coherence length for the crystalline F6TCNNQ. The region around the needles has a different contrast observed in the lateral force map. The low-friction areas (darkest colour) consist of molecular layers with a height difference of 3nm (or multiples of 3nm), confirming that they are C8-BTBT. In addition, there are a few rectangular islands, with a height of about 4nm - 9nm, which appear in the corresponding lateral force channel with an intermediate contrast. These regions are attributed to the 3D co-crystal formed by the effect of thermal annealing at 60°C (as illustrated in Figure 7.2d).

To study the impact of annealing at a higher temperature, a twin sample was prepared that was annealed directly up to 120°C for four minutes. Figure 7.4a and b show the OOP measurement and the corresponding 2D GIXD maps. OOP XRD shows prominent co-crystal (001) and (003) Bragg peaks, at  $q_z = 3.3\text{nm}^{-1}$  and  $9.9\text{nm}^{-1}$ , respectively. The second-order co-crystal Bragg peak is not clearly visible because it overlaps with the (003) Bragg peak of C8-BTBT. The coherence length, calculated from the FWHM of the (001) Bragg peaks is  $L_c = 51\text{nm}$  for the co-crystal and  $L_c = 30\text{nm}$  for C8-BTBT. In the 2D diffraction map, new structural features appear, which can be attributed to the co-crystal formation. The rod at  $q_{xy} = 18.6\text{nm}^{-1}$  visible in the 2D diffraction map corresponds to the  $\pi$ - $\pi$  co-crystal stacking. The rods observed at  $q_{xy} = 9.6\text{nm}^{-1}$ ,  $11.1\text{nm}^{-1}$ ,  $13.8\text{nm}^{-1}$  and  $22.5\text{nm}^{-1}$  appear at similar  $q$  positions reported for the F6TCNNQ-BTBT co-crystal structure by Dasari *et. al.*<sup>[154]</sup> Hence, are labelled here accordingly (red dash-dotted lines in Figure 7.4b). The (01L) rod of the co-crystal appear at the same  $q_{xy}$  position of (10L) rod of C8-BTBT but

with the co-crystal spacing ( $\Delta q_z = 3.3 \text{ nm}^{-1}$ ) along  $q_z$ . Notably, the F6TCNNQ OOP peak at  $q_z = 12.6 \text{ nm}^{-1}$ , disappeared after annealing at  $120^\circ\text{C}$ , implying that the F6TCNNQ 3D crystallites have been consumed in the formation of F6TCNNQ-C8-BTBT CTC co-crystals. The F6TCNNQ structural features in the 2D GIXD pattern also vanished, while the C8-BTBT Bragg peaks remain the same and 2D GIXD maps (Figure 7.4b) still show the diffraction pattern from the C8-BTBT structure. Hence the consumption of C8-BTBT molecules by the formation of the co-crystal is not worsening the crystallinity or coherence length of the C8-BTBT film underneath. This leads us to conclude that the co-crystallites are partially embedded in the C8-BTBT film (Figure 7.4c).

The topographical inspection of the same sample by AFM confirms this. Figure 7.4d, e, and f show the topography and corresponding lateral force image and the height profile along the marked line in the topography.

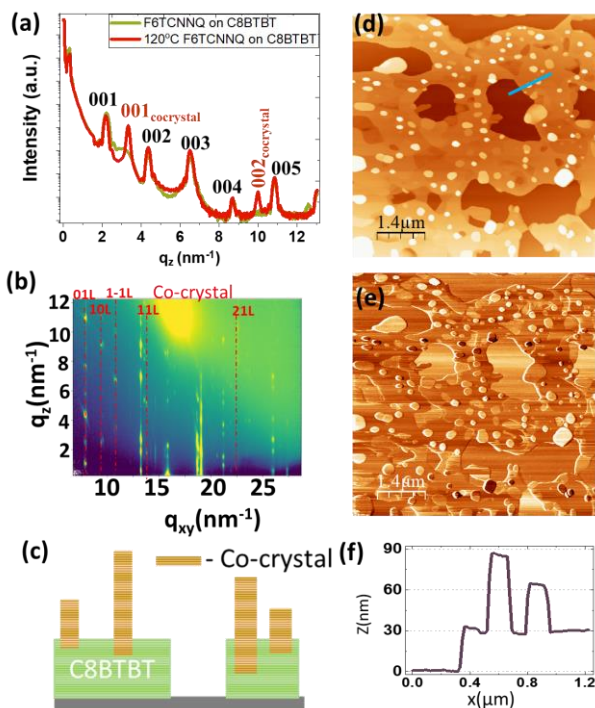


Figure 7.4. (a) Out-of-plane XRD of F6TCNNQ/C8-BTBT heterostructure measured as prepared at RT and after annealing at  $120^\circ\text{C}$  (as indicated in the legends) (b) corresponding 2D GIXD map, after annealing at  $120^\circ\text{C}$ . (c) Scheme displaying the co-crystal formed within the C8-BTBT film after annealing. (d) Topography and the (e) corresponding lateral force map of the annealed sample. (f) The height profile across the line is indicated in the topography (d).

The topography shows a discontinuous film, with the substrate visible in some regions. The average height of the film is 30nm (as shown in Figure 7.4f), in excellent agreement with the coherence length of C8-BTBT estimated from the OOP data. In addition, conversely to the needles observed at a lower annealing temperature (Figure 7.3), some structures can be spotted with a near-circular shape and a lateral size of about 200nm - 600nm. Their heights (with respect to the substrate), in a range between 25nm and 90nm, are also consistent with the  $L_c$  estimated for the co-crystal. Therefore, it is reasonable to attribute the tall structures observed in the topography to co-crystals. As illustrated in Figure 7.4c, we propose that the co-crystals are embedded within the C8-BTBT film, without altering the C8-BTBT in-plane or out-of-plane crystalline order.

To investigate the evolution of the optical absorption properties with annealing, UV-Vis absorption spectroscopy was done on glass substrates for a pristine C8-BTBT and an F6TCNNQ (12nm)/C8-BTBT (15nm) heterostructure (Figure.7.5).

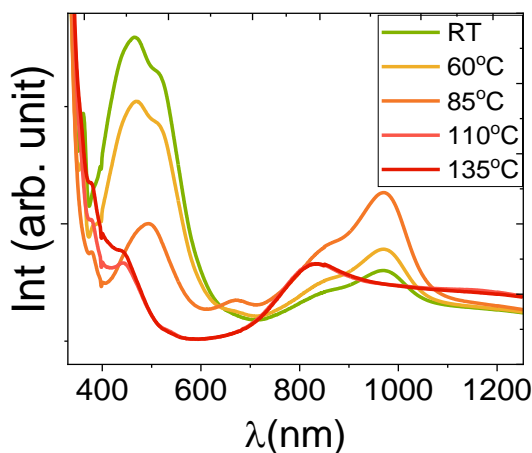


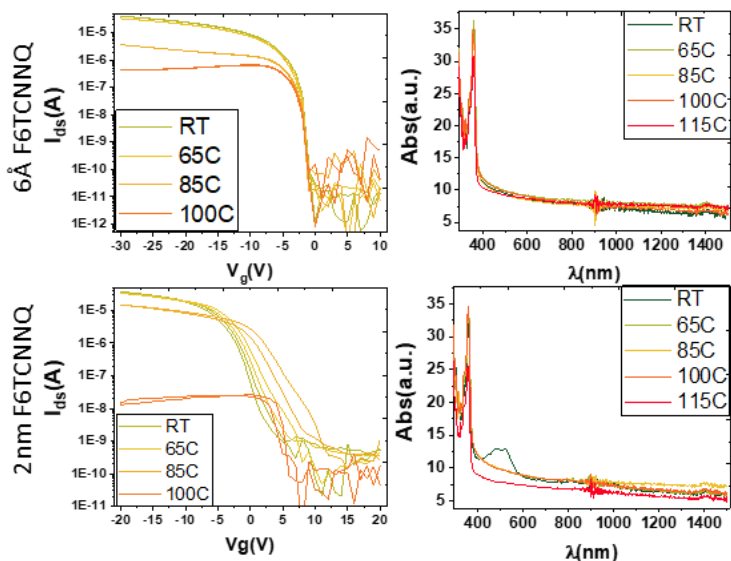
Figure.7.5. Evolution of UV-Vis absorption spectra of C8-BTBT (20nm) thin film with F6TCNNQ (14nm) on top, with increasing temperature.

For the heterostructure at RT, the absorption bands of the individual components are observed. The F6TCNNQ-C8-BTBT co-crystal CTC bands are also visible, although with lower intensity than the C8-BTBT and F6TCNNQ absorption bands. With annealing, two effects are observed. The intensity of both C8-BTBT and F6TCNNQ peaks decreases. Meanwhile, the co-crystal CTC peaks increase in intensity when the temperature is increased up to 110°C,

indicating the formation of more co-crystals. Surprisingly, the peak at 960nm diminished along with the formation of a new peak near 800nm after annealing at 130°C, implying a rearrangement of the electronic levels of the thin film. Further studies need to be done to understand this process, which is out of the scope of the thesis. UV-Vis absorption spectra along with XRD and AFM data, confirm the growth of well-ordered F6TCNNQ-C8-BTBT CTC co-crystals with annealing temperature. This parameter can be used to have control over the morphology, extent and distribution of CTC in the films.

### 7.1.2. Impact of thermal annealing on the electrical properties

This section studies the changes that occurred in C8-BTBT OFETs with annealing. As described in the previous section, annealing the C8-BTBT film up to 120°C with F6TCNNQ on top increases the formation of oriented co-crystal on the surface. Figure 7.6 shows the effect of temperature on CTC doped C8-BTBT OFETs and the corresponding UV-Vis absorption spectra. The amount of F6TCNNQ deposited on the surface of the C8BTBT layer for the samples is 6Å, 2nm, 10nm, 20nm and 30nm, from top to bottom as indicated at the left vertical axis of the corresponding panels.



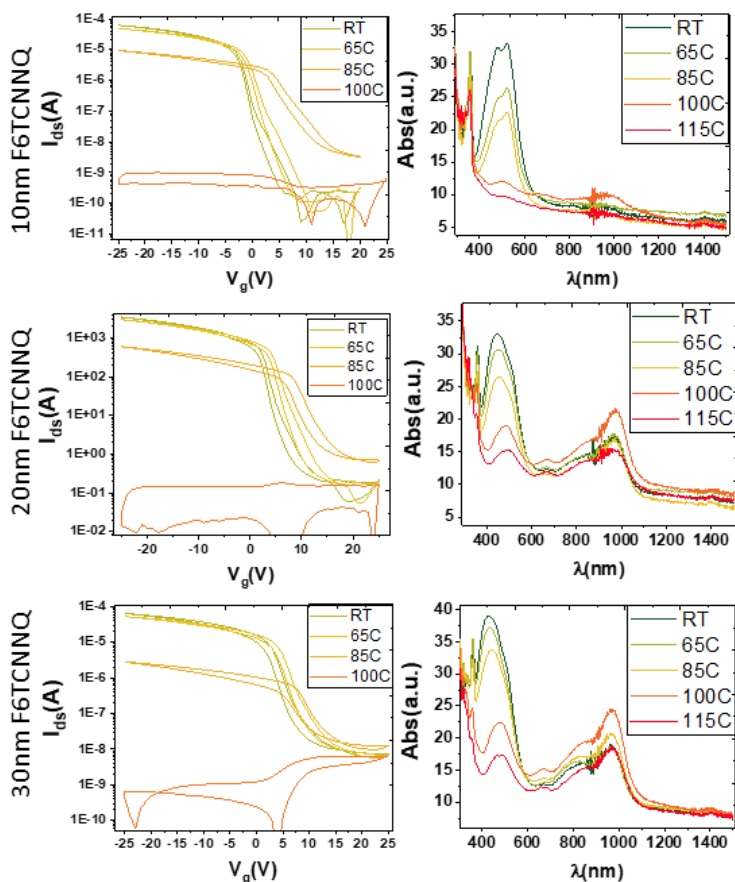


Figure 7.6. Evolution with the temperature of the transfer curves at  $V_{ds} = -30V$  (logarithmic scale) for C8-BTBT (35nm) OFETs with different amounts of F6TCNNQ deposited on top (indicated on the leftmost side of each curve). In the right panel the evolution of the corresponding UV-Vis absorption spectra. Legends in each figure show the respective annealing temperatures.

The increase in temperature adversely affected the C8-BTBT OFETs and worsened their performance. There is an increase in the  $I_{off}$  current and  $V_{on}$  with temperature in the samples with an F6TCNNQ coverage above 2nm. In addition, the  $I_{off}$  current and  $V_{on}$  shifts increase with F6TCNNQ coverage. An increase in temperature promotes the interaction of unreacted F6TCNNQ with C8-BTBT and aids the formation of CTC co-crystal. These results indicate that the film is being doped by the F6TCNNQ-C8-BTBT CTC co-crystal and

there is an extra generation of free charge carriers with an increase in temperature. The maximum current measured ( $I_{on}$ ) was not increasing with temperature, in fact,  $I_{on}$  and the subthreshold slope decreased with temperature for all F6TCNNQ coverages. UV-Vis absorption spectroscopy shows the further formation of CTC co-crystals with increasing temperature for which a considerable amount of F6TCNNQ was deposited on the surface. After annealing at 100°C, most of the films show a predominance of CTC peaks, indicating the larger thermal stability of the co-crystals.

## 7.2. Relevance of the deposition sequence on the co-crystal formation

In this section, we address the impact of the deposition sequence on the structural quality of the heterostructure and on the formation of the mixed co-crystal. Conversely to the previous heterostructures, here F6TCNNQ was firstly deposited on the Si/SiO<sub>2</sub> substrate and after being characterized by OOP XRD and GIXD, C8-BTBT was deposited on top. The amount of deposited materials was the same as in section 7.1.1.

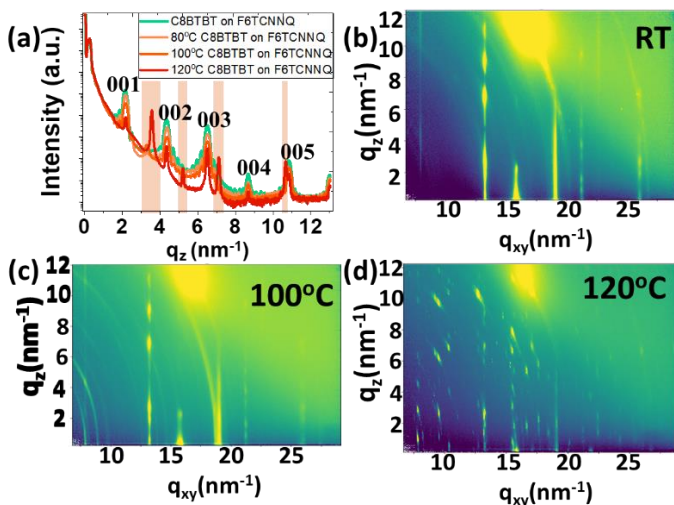


Figure 7.7. (a) Out-of-plane XRD of C8-BTBT on top of F6TCNNQ, measured at RT and after annealing at 80°C, 100°C and 120°C (as indicated in the legends). Highlighted area shows the emerged co-crystal peaks after annealing. (b) Corresponding 2D GIXD map measured after annealing at (b) RT and after annealing at (c) 100°C and (d) 120°C.

The cyan-coloured curve in Figure 7.7a shows the out-of-plane diffraction pattern of the C8-BTBT/F6TCNNQ heterostructure at RT and Figure 7.7b shows the corresponding 2D GIXD map. It has been reported that F6TCNNQ is polycrystalline on native SiO<sub>2</sub>.<sup>[67]</sup> This fact has been confirmed by our GXID data for F6TCNNQ on SiO<sub>2</sub>. As shown in appendix 10.2, the 2D diffraction pattern consists of diffraction powder rings indicating that F6TCNNQ molecules aggregate on the surface without any preferential orientation on the surface (as illustrated in the cartoon in the Figure 7.8a). Both the observation of C8-BTBT Bragg peaks up to the fifth order in the OOP XRD and the 2D GIXD diffraction pattern indicate that C8-BTBT grows with the same structure and orientation as it is on SiO<sub>2</sub>. No evidence of co-crystal formation was observed at RT, pointing to the importance that the sequence employed for the deposition of OSC and dopant has in the co-crystal formation.

To investigate if, in the present case, increasing temperature promotes co-crystal growth, the sample was annealed at diverse temperatures (Figure 7.7a). The corresponding OOP data displayed for 100°C (orange curve) reveal the co-crystal formation by the emergence of the (001) co-crystal Bragg peak around  $q_z = 3.3\text{nm}^{-1}$  (enclosed by a pink vertical band). The most significant change in the 2D GXID map (Figure 7.7c) is the emergence of diffraction powder rings (see Table 10.1 in the Appendix). The  $q$ -position of the rings agrees with the co-crystal structural features observed for F6TCNNQ on C8-BTBT (see Figure 7.4b), having here a large azimuthal disorder instead of (001) texture. C8-BTBT remains unaffected as observed in the OOP and GIXD data.

Further annealing of the film at 120°C promotes larger structural changes. In OOP spectrum (red line in the Figure 7.7a), the peak at  $q_z = 3.3\text{nm}^{-1}$ , disappear and four new peaks emerge at  $q_z = 3.6\text{nm}^{-1}$ ,  $5.2\text{nm}^{-1}$ ,  $7.1\text{nm}^{-1}$ , and  $10.7\text{nm}^{-1}$ . These new peaks correspond to two different inter-planar distances of 1.76nm and 1.2nm, which are smaller than the periodicity obtained from the 001 planes of the co-crystal formed with the previous deposition sequence (i.e., F6TCNNQ on top of C8-BTBT). The coherence length calculated from the FWHM of these new peaks is, on average,  $L_c = 80\text{nm}$ . Unlike the previous heterostructure after annealing at 120°C, this case shows a dramatic decrease in the intensity and the width of the OOP Bragg peaks of the C8-BTBT. This could be due to the combined effect of desorption of C8-BTBT molecule from the surface and consumption for co-crystal formation. The diffraction spots corresponding to C8-BTBT in 2D GIXD maps became fainter. The rings also disappeared after the annealing in the 2D GIXD map (Figure 7.7d). A complex diffraction pattern is now visible, which seems to agree with a complex mixing scenario.

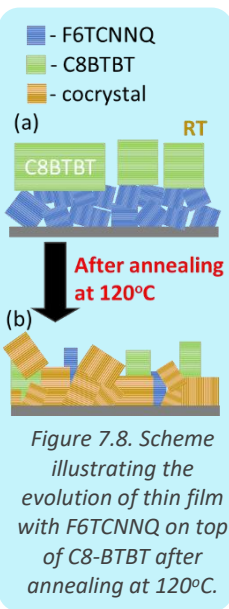


Figure 7.8. Scheme illustrating the evolution of thin film with F6TCNNQ on top of C8-BTBT after annealing at 120°C.

There are mainly two plausible scenarios that could explain the result shown in Figure 7.8b. The first is the existence of two preferential orientations of the co-crystal on the surface and the other is the existence of different polymorphs. Both scenarios would adversely affect the C8BTBT thin film structure and C8-BTBT OFETs. The results reveal the importance of the order of deposition of C8-BTBT and F6TCNNQ in the formation of ordered CTC co-crystals.

### 7.3. Influence of the OSC side groups on the co-crystal formation

To investigate the role played by the OSC side group in the co-crystal formation, F6TCNNQ was deposited on top of DPh-BTBT thin films. The effect of thermal post-annealing treatment was also investigated.

The heterostructure (F6TCNNQ/DPh-BTBT) was grown at the ICMAb and measured at the NCD-SWEET beamline of the ALBA synchrotron a few days after the growth. The experimental set-up allows annealing of the sample under N<sub>2</sub> and performs GIXD measurements in-situ. Figure 7.9a shows the out-of-plane XRD of pristine DPh-BTBT as well as DPh-BTBT with 70Å and 140Å of F6TCNNQ on top. Pristine DPh-BTBT film (20nm thick) shows the characteristics of OOP Bragg peaks of oriented crystalline films with (001) planes parallel to the surface.

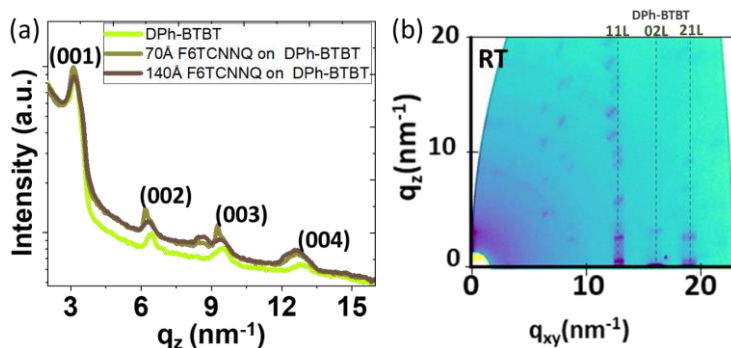


Figure 7.9. (a) Out-of-plane XRD obtained from GIXD performed on a pristine 20nm thick DPh-BTBT film (green) and a 20nm thick DPh-BTBT film with different coverages of F6TCNNQ on top (as indicated by the legends) at RT. (b) 2D GIXD map of the 20nm thick DPh-BTBT film with 140Å F6TCNNQ on top, at RT.



No prominent changes were observed in the OOP diffraction pattern even after 140Å of F6TCNNQ deposition. The appearance of peaks around  $q_z \sim 8.7\text{nm}^{-1}$  and  $12.6\text{nm}^{-1}$  for 140Å of F6TCNNQ coverage, on the DPh-BTBT film, is attributed to crystalline F6TCNNQ, as already seen in the case of C8-BTBT with F6TCNNQ on top. Figure 7.9b displays the 2D GIXD diffraction pattern obtained for 140Å of F6TCNNQ on the DPh-the BTBT film. In addition to the diffraction features of the DPh-BTBT structure, there are several rings with spots along with them in the GIXD map which indicate the coexistence of polycrystalline F6TCNNQ with vertically oriented 3D crystallites of F6TCNNQ. There is no evidence of F6TCNNQ-DPh-BTBT co-crystal formation.

To evaluate if an increase in temperature could trigger the co-crystal formation between DPh-BTBT and F6TCNNQ, the samples were annealed stepwise and measured in-situ at different temperatures. Figure 7.10a shows the OOP diffraction data measured at different temperatures for the heterostructure. Surprisingly, no changes were observed in the OOP peaks of DPh-BTBT. 2D GIXD maps (Figure 7.10b) also do not show noticeable differences in the diffraction patterns with an increase in temperature. A reduction in the intensity of the F6TCNNQ rings suggests either the desorption of F6TCNNQ from the surface or the transformation to an amorphous phase. In any case, there is no evidence of co-crystal formation.

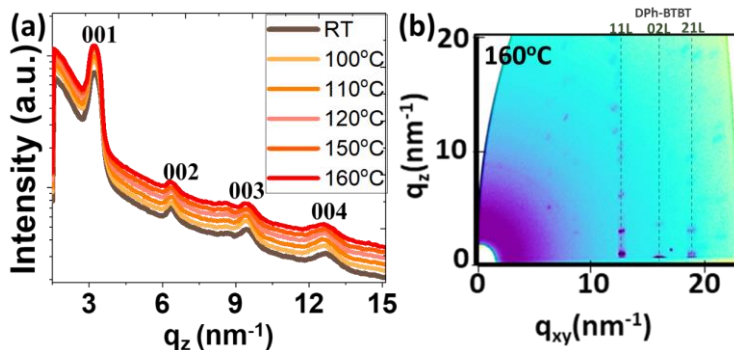
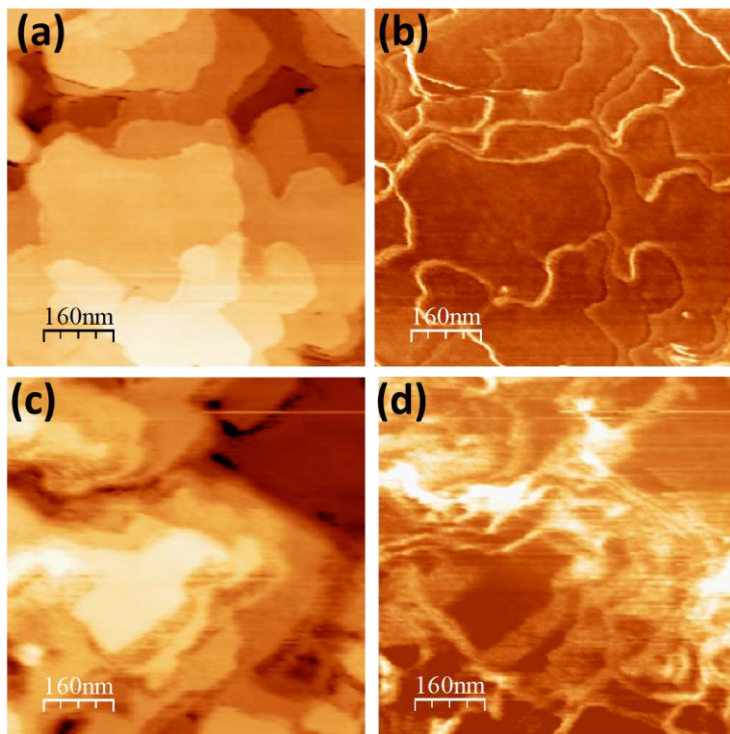


Figure 7.10. (a) Out-of-plane XRD obtained from 2D GIXD performed on 20nm thick DPh-BTBT film with 140Å of F6TCNNQ on top, measured at different temperatures (as indicated by the legends). (b) Corresponding 2D GIXD map measured at 160°C.

To investigate the morphology of the F6TCNNQ- DPh-BTBT interface, AFM measurements were performed. Figure 7.11a shows the topography of a bare 20nm thick DPh-BTBT film and Figure 7.11c the film after 7nm of F6TCNNQ was deposited on top and annealed at 160°C. A multi-layered structure of the

DPh-BTBT film is observed in both cases. But in the case of DPh-BTBT with F6TCNNQ plus annealing shows low density aggregates around the steps of DPh-BTBT. Comparison between the corresponding lateral force images (Figure 7.11b, d) these aggregates can be attributed to F6TCNNQ, consistent with the observation of faint F6TCNNQ rings in the 2D GIXD map (Figure 7.10b). Both XRD and AFM data indicate that the phenyl-termination of the BTBT films does not allow intermixing even at elevated temperatures. Therefore, these results point to the relevance of the flexible alkyl chains of the BTBT in the formation of F6TCNNQ-C8-BTBT CTC co-crystals.



*Figure 7.11. (a) Topography and (b) lateral force map of a pristine 20nm thick DPh-BTBT film. (c) Topography and (d) lateral force map of a 20nm thick DPh-BTBT film with 70Å of F6TCNNQ on top plus annealing at 160°C.*

In summary, a detailed study of the influence of the structure of the interface in the formation of co-crystals has been done. The results from XRD, AFM and UV-Vis absorption confirm the further growth of F6TCNNQ-C8-BTBT CTC co-crystal at higher temperatures. The influence of the deposition sequence of

C8-BTBT and F6TCNNQ has been demonstrated. Whereas co-crystal formation also occurs when C8-BTBT is deposited on top of F6TCNNQ, the data suggest the formation of different polymorphs. Even though the DPh-BTBT molecule has a similar HB packing of the BTBT cores, there is no evidence of the formation of F6TCNNQ-DPh-BTBT co-crystals even after thermal annealing, which reveals the significance of the type of side groups of OSC in the co-crystal formation. It is proposed that the packing of the phenyl group of DPh-BTBT hinders the intercalation of F6TCNNQ molecules between its BTBT core.

## 8. Co-evaporation of F6TCNNQ and C8-BTBT

Generation of mobile holes by the CTC crystallites formed from co-deposition of dopant and OSC, in the circumjacent OSC film has been reported but is effective for only small dopant concentrations.<sup>[45],[43]</sup> This chapter presents the study of the C8-BTBT OFET co-evaporated with F6TCNNQ, since mixing dopant in the organic semiconductor (OSC) matrix (bulk doping) is a widely used strategy to dope, which often results in the formation of dopant-OSC charge transfer complex and co-crystals.<sup>[43],[48],[40],[155]</sup>

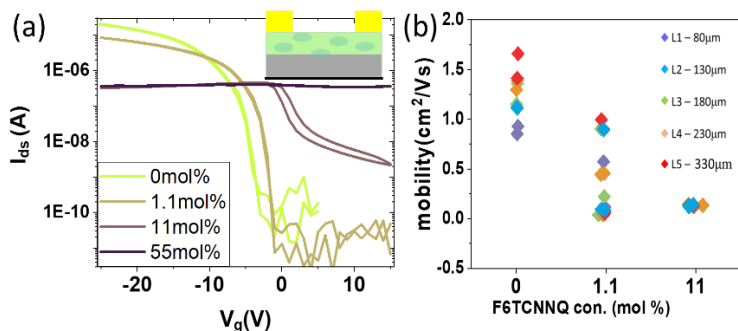


Figure 8.1. Linear transfer curves at  $V_{ds} = -5V$  for OFETs with  $L = 230\mu m$  in BG-TC geometry for C8-BTBT and F6TCNNQ co-evaporated films with the indicated concentrations. (b) Evolution of mobility calculated for C8-BTBT OFETs with different channel lengths with respect to the amount of F6TCNNQ.

Figure 8.1a shows the transfer characteristic of BG-TC C8-BTBT OFETs with different concentrations of F6TCNNQ co-evaporated with C8-BTBT ( $\sim 35\text{nm}$ ). Four sets of devices were investigated, starting with the pristine device without dopant and then increasing the dopant concentration up to 55mol% by adapting the relative evaporation rate of F6TCNNQ. A shift of  $V_{\text{on}}$  towards a more positive gate value as well as an increase in the off current with an increment in F6TCNNQ concentration was observed. This indicates that the C8-BTBT film is being doped. The evolution of the mobility for different channel lengths with respect to F6TCNNQ concentration is shown in Figure 8.1b. Even though the  $V_{\text{on}}$  voltage of the transistor shifts with the increasing concentration of F6TCNNQ, the incorporation of the dopant worsened the mobility of the transistor. For dopant concentration of 55mol%, the transistor behaviour has fully deteriorated, and the film became conductive.

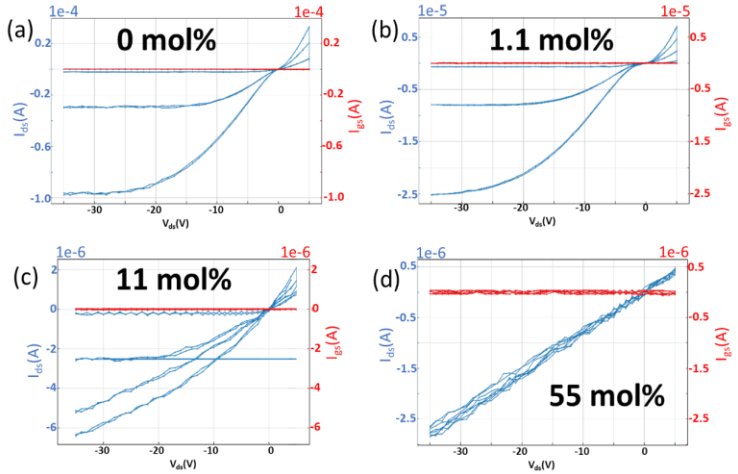


Figure 8.2. Representative output curves ( for  $V_g = 0\text{V}, -10\text{V}, -20\text{V}, -30\text{V}$ ) of C8-BTBT OFETs of  $230\mu\text{m}$  channel length co-evaporated with increasing molecular percentage of F6TCNNQ from 0mol% to 55mol% as indicated for each graph.

A similar trend, i.e., lower mobility with increasing dopant concentration has been reported for Pentacene OFETs.<sup>[52],[47]</sup> The output curves of representative bulk doped OFETs of  $230\mu\text{m}$  channel length are given in Figure 8.2, which also display deterioration of C8-BTBT OFET performance with increasing F6TCNNQ concentration.

UV-Vis absorption spectroscopy and 2D grazing incidence X-ray diffraction (GIXD) were performed. The samples were grown on glass substrates during the fabrication of the OFETs. In the UV-Vis absorption spectra shown Figure.8.3, a set of new peaks (brown band) started to emerge at large F6TCNNQ concentrations along with the peaks from C8-BTBT, F6TCNNQ (green and blue bands, respectively). The new set of peaks reveals the presence of F6TCNNQ-C8-BTBT CTC. Hence, the changes observed in C8-BTBT OFETs prepared by co-deposition can be explained by doping due to the CTC formed within the OSC layer.

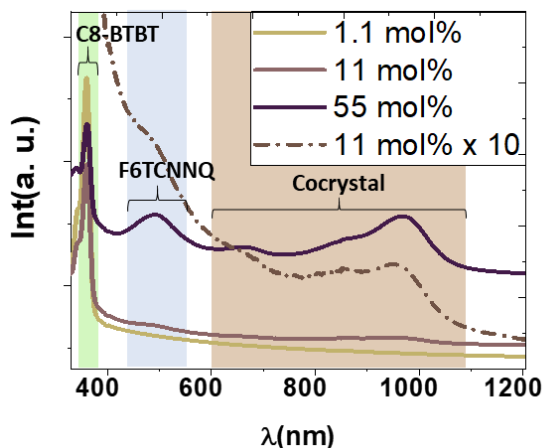


Figure.8.3. UV-Vis absorption spectra for co-evaporated C8-BTBT films with F6TCNNQ concentration. Absorption peaks from C8-BTBT, F6TCNNQ and CTC are labelled.

To understand the thin film structure of the C8-BTBT film co-evaporated with F6TCNNQ, 2D GIXD measurements were performed on the same samples. The out-of-plane x-ray diffraction measurements of the co-evaporated films of C8-BTBT with different mol% of F6TCNNQ are shown in Figure 8.4a. The (001) and (002) Bragg peaks from C8-BTBT have been observed for all F6TCNNQ concentrations. The new peak at  $q_z = 3.3\text{nm}^{-1}$ , observed at a high dopant concentration of 55mol%, corresponds to the C8-BTBT-F6TCNNQ cocrystal. The 2D GIXD maps of co-evaporated film of C8-BTBT and 55mol% F6TCNNQ shown in Figure 8.4b shows no visible changes for C8-BTBT diffraction features. The co-crystal features appear as spots in the out-of-plane direction.

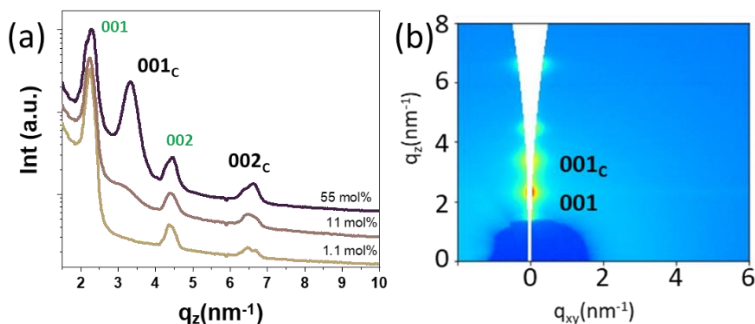


Figure 8.4. (a) Out-of-plane, XRD features for C8-BTBT-F6TCNNQ co-evaporated thin films with increasing F6TCNNQ concentration, from the 2D GIXD map obtained at  $0.15^\circ$  incident angle. (b) 2D GIXD map measured at  $0.11^\circ$  incident angle, for 55mol% of F6TCNNQ. Indicated 001 peak is from ordered C8-BTBT and 001<sub>c</sub> is from the F6TCNNQ-C8-BTBT CTC co-crystal.

The emergence of Bragg peaks indicated that the co-crystal has a 3D crystalline structure, within the OSC matrix. A fair amount of C8-BTBT remains unaffected. However, these results cannot explain the decrease of field effect mobility observed in the C8-BTBT OFETs with increasing dopant concentration.

Figure 8.5 shows the AFM images of the OFET channel topography with an F6TCNNQ concentration of 1.1mol%, 11mol% and 55mol% respectively. The 1.1mol% of F6TCNNQ doped C8-BTBT OFET shows similar morphology to that of C8-BTBT OFETs.<sup>[32]</sup> For increasing dopant concentration, the channel morphology of the OFETs changed drastically.

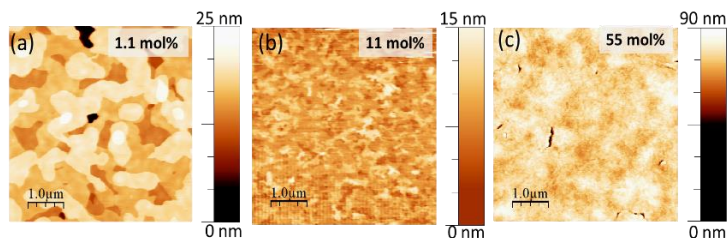


Figure 8.5. Channel morphology of the co-evaporated C8-BTBT FETs with F6TCNNQ concentration of (a) 1.1mol%, (b) 11mol% and (c) 55mol%.

For a concentration of 55mol% F6TCNNQ, the topmost surface is featureless except for a few cracks. The observed differences in morphology point to an

explicit decrease in the lateral size of the C8-BTBT domains as the most plausible origin of the reduction in field-effect mobility of the OFETs as the dopant-OSC ratio is increased.

In summary, the combined analysis by AFM, GIXD and UV-Vis absorption reveals the formation of a C8-BTBT-F6TCNNQ CTC co-crystal structure in the co-evaporated film. The shift in  $V_{on}$  and the increase in  $I_{off}$  current indicates the increased density of free carriers in the organic semiconductor film. Even though CTC formation and the presence of mobile charges are demonstrated to occur, the spatial distribution of the co-crystals in the bulk disrupts the structural order of the OSC thin film. Hence, a decrease in the field-effect mobility even for a dopant ratio of about 1mol% is observed due to a reduction of the lateral size of the grain morphology.



## 9. Conclusion

---

The work presented in this thesis aims to understand the role of both, the particular structure of the molecules and the packing adopted during thin film growth, in the doping phenomena of organic semiconductors. OSC with aromatic and aliphatic side chains along with flat and spherical dopant molecules have been employed for the investigation. The diverse dopant-OSC interfaces have been examined by using AFM, KPFM, Synchrotron X-ray diffraction techniques, XPS/UPS, and UV-Vis absorption spectroscopy. The evolution of the interfacial morphology and the electronic levels during the doping process were investigated in correspondence to the molecular structure of the OSC and the dopant.

First, the interface formed between the C8-BTBT molecule with octyl chain side group and spherical  $C_{60}F_{48}$  was studied. It is demonstrated that the dopant molecule forms crystallites at the step edges of C8-BTBT, hindering dewetting of the C8-BTBT film and increasing the stability of the films and the OFETs. There is no intercalation observed between C8-BTBT and  $C_{60}F_{48}$ . Then we have explored the effect of the OSC molecular side groups in the interface formation. The interface formed in  $C_{60}F_{48}$ /DPh-BTBT and  $C_{60}F_{48}$ /C8-BTBT heterostructures has been compared.  $C_{60}F_{48}$  distribute homogeneously on top of the DPh-BTBT film, revealing the importance of the OSC side group in the formation of the interfacial morphology. The evolution of energy levels during doping reveals the presence of surface dipoles arising from integer charge transfer from C8-BTBT and DPh-BTBT to  $C_{60}F_{48}$ . The difference in interfacial morphology due to the different side groups determines the nanoscale surface potential distribution at the interface.

Furthermore, the impact of the dopant molecular structure was investigated by probing the interface of the F6TCNNQ/C8-BTBT heterostructure. It is demonstrated that F6TCNNQ intercalates with underlying C8-BTBT molecules to form co-crystallites. Further analysis of factors affecting the formation of C8-BTBT-F6TCNNQ CTC on the surface is also presented. It is shown that in F6TCNNQ/C8-BTBT heterostructures, the temperature promotes the growth of CTC on the surface while in the inverted heterostructure (C8-BTBT on F6TCNNQ), exclusive structural features have been observed with an increase in temperature and are attributed to different polymorphs of the co-crystals. On the other hand, no evidence for the formation of DPh-BTBT-F6TCNNQ co-

crystals has been found, even at a higher temperature. These results clearly indicate the influence of the OSC side groups in CTC formation.

Finally, to investigate the effect of the dopant molecular structure on the doping mechanism, OFETs of C8-BTBT were fabricated and characterized before and after doping with  $C_{60}F_{48}$  and F6TCNNQ. The spherical  $C_{60}F_{48}$  dopant undergoes ion pair formation by integer charge transfer across the interface and results in surface dipoles that reduce the contact resistance. In turn, the planar F6TCNNQ dopant molecule undergoes ground state charge transfer complex formation by intermixing of OSC and dopant molecules at the interface, which dopes the C8-BTBT film and generates mobile charge carriers. Depending on the amount of deposited F6TCNNQ, doping can contribute to passivate charge traps or to increase the conductivity of the film. It is also demonstrated CTC formation in the C8-BTBT: F6TCNNQ co-evaporated films, which disturbs the structural order of the C8-BTBT film and results in deterioration of the device performance.

This thesis work demonstrates the importance of molecular structure in thin-film growth, dopant/OSC interface formation and doping mechanism. The structure of molecules determines the extent and mechanism of surface doping. This fact also opens the possibility of selecting a dopant or choosing a particular doping mechanism to get a specific outcome or for tuning device parameters, selectively. In fact, controlled doping is a challenge in the field of organic electronics, and we believe that the conclusions of this work can be of general applicability during the fabrication of stable and efficient doped organic electronic devices.

## 10. Appendix

### 10.1. F6TCNNQ-C8-BTBT co-crystal formation from solution processing

The objective was to investigate the interface of F6TCNNQ and C8-BTBT films developed from solution processing.

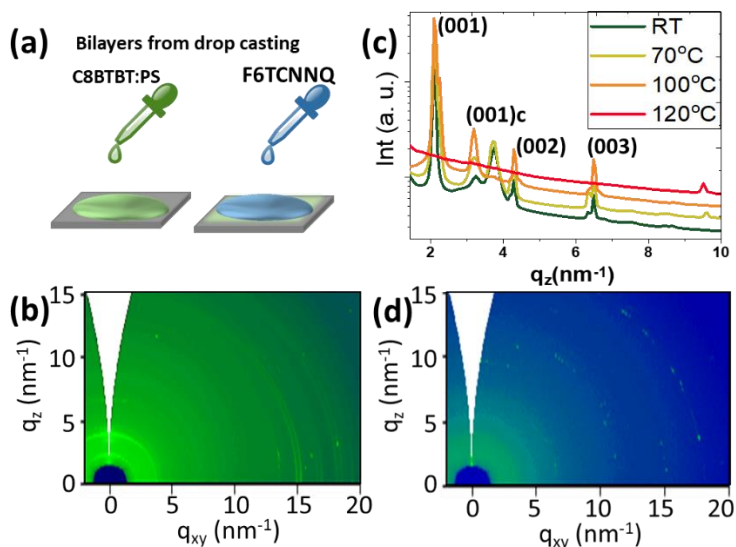


Figure 10.1. (a) Scheme for sequential deposition of C8-BTBT and F6TCNNQ from solution and (b) the corresponding GIXD map at RT. (c) Out-of-plane peaks of sequentially drop-casted heterostructure film at different annealing temperatures as indicated in the legend. (d) GIXD of the thin film from sequential deposition after annealing at 120°C.

2D GIXD maps of thin-film fabricated from sequential deposition of F6TCNNQ and C8-BTBT solutions in chloroform are shown in (Figure 10.1 b). 1mM C8-BTBT solution was drop cast on Si substrate, then 1mM solution of F6TCNNQ was drop cast on top of it. After each deposition, the sample was heated to

70°C to remove excess solvent. The GIXD map shows rings at  $q$  positions corresponding to the crystalline structures of C8-BTBT and F6TCNNQ films.<sup>[32],[156]</sup> Out-of-plane diffraction patterns obtained from the cut along the  $q_z$  direction are shown in Figure 10.1c, which show diffraction peaks at  $q_z \sim 2.2\text{nm}^{-1}$ ,  $q_z \sim 4.4\text{nm}^{-1}$  and  $q_z \sim 6.6\text{nm}^{-1}$  corresponding to the characteristic (00L) Bragg peaks of C8-BTBT. Two diffraction peaks at  $q_z \sim 3.3\text{nm}^{-1}$  and  $q_z \sim 3.8\text{nm}^{-1}$  are observed in the  $q_z$  direction. Both are attributed to different co-crystals formed between the F6TCNNQ and C8-BTBT molecules, possibly due to differences in the mixing stoichiometry. Yet, the intensity of these peaks is small indicating a smaller amount of co-crystals were formed in the film. Figure 10.1c compares the diffraction peaks in the OOP direction at different annealing temperatures and Figure 10.1d shows the GIXD map of the film after annealing at 120°C. The variation in Bragg peak intensity observed after annealing at 100°C shows the rearrangement of the structure is happening in the film and all of which later disappear after annealing at 120°C.

## 10.2. XRD features of F6TCNNQ

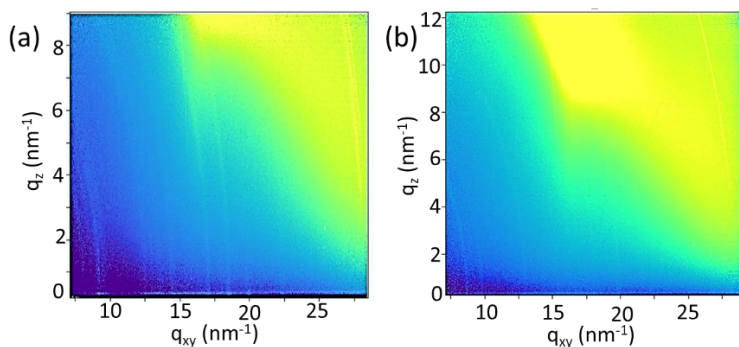


Figure 10.2. 2D GIXD maps of F6TCNNQ on  $\text{SiO}_2$  at (a) RT and (b) after annealing at 120°C

Faint rings like features are observed on the 2D GIXD maps of the sample with F6TCNNQ deposited on top of native  $\text{SiO}_2$  at RT and after annealing at 120°C for 4min (Figure 10.2). This implies the polycrystalline growth of F6TCNNQ on Si substrate. The table below shows the  $q$ -values corresponding to the F6TCNNQ XRD features, obtained from the 2D GIXD maps.

F6TCNNQ on SiO <sub>2</sub>		F6TCNNQ on C8-BTBT	
q at RT (nm <sup>-1</sup> )	q at 120°C (nm <sup>-1</sup> )	q at RT (nm <sup>-1</sup> )	q at 100°C (nm <sup>-1</sup> )
8.13	8.67	8.23	7.83
8.70	9.78	9.28	8.13
9.63	13.05	9.57	8.85
12.51	18.09	9.65	9.69
13.50	19.89	10.20	12.57
14.52		12.54	13.83
17.10		12.64	14.61
18.51		13.60	18.75
20.00		14.59	
22.26		18.72	
		20.26	
		20.32	
		20.30	
		22.33	

Table 10.1. Values of  $q$  corresponding to the powder diffractions rings observed for F6TCNNQ on SiO<sub>2</sub> (from the data in Figure 10.2) and F6TCNNQ on C8-BTBT (Figure 7.7).

## 11. References

---

- [1] P. Güell-Grau, F. Pi, R. Villa, J. Nogués, M. Alvarez, B. Sepúlveda, *Appl. Mater. Today* **2021**, *23*.
- [2] M. Dei, J. Aymerich, M. Piotto, P. Bruschi, F. J. del Campo, F. Serra-Graells, *Electron.* **2019**, *8*, 1.
- [3] M. Zea, R. Texidó, R. Villa, S. Borrós, G. Gabriel, *ACS Appl. Mater. Interfaces* **2021**, *13*, 33524.
- [4] M. Mass, L. S. Veiga, O. Garate, G. Longinotti, A. Moya, E. Ramón, R. Villa, G. Ybarra, G. Gabriel, *Nanomaterials* **2021**, *11*.
- [5] H. Kobayashi, N. Kobayashi, S. Hosoi, N. Koshitani, *J. Chem. Phys.* **2013**, *139*, 014707.
- [6] F. Zhang, X. Dai, W. Zhu, H. Chung, Y. Diao, *Adv. Mater.* **2017**, *29*, 1700411.
- [7] S. Bayatpour, J. C. Mello, A. Ferguson, W. Braunecker, J.-H. Choi, I. Fischer, F. Cicoira, S. Gomez-Carretero, P. Graziosi, P. Kjall, N. Kopidakis, Y. Iwasa, J. Leger, H. Jimison, Leslie, P. Meredith, B. Mostert, Albertus, O. D. Jurchescu, J.-D. Oh, D. Olson, M. Prezioso, O. Ostroverkhova, A. Riminucci, M. Owens, Roisin, J. Rivnay, A. Pezzella, A. Salleo, C. Santato, W. Phillips, Thomas, J. Sayago, A. P. H. J. Schenning, S. Toshner, H.-S. Seo, J. Wunsche, J. Zaumseil, T. Takenobu, T. Kristen, *organic electronics* (Eds.: Cicoira, F.; Santato, C.), Vol. 3, Wiley-VCH Verlag GmbH & Co. KGaA, **2013**.
- [8] A. A. Virkar, S. Mannsfeld, Z. Bao, N. Stingelin, *Adv. Mater.* **2010**, *22*, 3857.
- [9] J. Rivnay, S. C. B. Mannsfeld, C. E. Miller, A. Salleo, M. F. Toney, *Chem. Rev.* **2012**, *112*, 5488.
- [10] A. F. Paterson, S. Singh, K. J. Fallon, T. Hodsdon, Y. Han, B. C. Schroeder, H. Bronstein, M. Heeney, I. McCulloch, T. D. Anthopoulos, *Adv. Mater.* **2018**, *30*, 1.
- [11] M. M. Torrent, C. Rovira, *Chem. Soc. Rev.* **2008**, *37*, 827.
- [12] M. Waldrup, O. D. Jurchescu, D. J. Gundlach, E. G. Bittle, *Adv. Funct. Mater.* **2019**, *30*, 1904576.
- [13] C. Ruzié, J. Karpinska, A. Laurent, L. Sanguinet, S. Hunter, T. D. Anthopoulos, V. Lemaire, J. Cornil, A. R. Kennedy, O. Fenwick, P. Samorì, G. Schweicher, B. Chattopadhyay, Y. H. Geerts, *J. Mater. Chem. C* **2016**, *4*, 4863.
- [14] K. Takimiya, I. Osaka, T. Mori, M. Nakano, *Acc. Chem. Res.* **2014**, *47*, 1493.
- [15] K. He, W. Li, H. Tian, J. Zhang, D. Yan, Y. Geng, F. Wang, *ACS Appl. Mater.*

- [16] Y. Tsutsui, G. Schweicher, B. Chattopadhyay, T. Sakurai, J. B. Arlin, C. Ruzié, A. Aliev, A. Ciesielski, S. Colella, A. R. Kennedy, V. Lemaure, Y. Olivier, R. Hadji, L. Sanguinet, F. Castet, S. Osella, D. Dudenko, D. Beljonne, J. Cornil, P. Samori, S. Seki, Y. H. Geerts, *Adv. Mater.* **2016**, *28*, 7106.
- [17] Y. Yuan, G. Giri, A. L. Ayzner, A. P. Zombelt, S. C. B. Mannsfeld, J. Chen, D. Nordlund, M. F. Toney, J. Huang, Z. Bao, *Nat. Commun.* **2014**, *5*:3005, 1.
- [18] G. Schweicher, V. Lemaure, C. Niebel, C. Ruzié, Y. Diao, O. Goto, W. Y. Lee, Y. Kim, J. B. Arlin, J. Karpinska, A. R. Kennedy, S. R. Parkin, Y. Olivier, S. C. B. Mannsfeld, J. Cornil, Y. H. Geerts, Z. Bao, *Adv. Mater.* **2015**, *27*, 3066.
- [19] W. Wei, C. Yang, J. Mai, Y. Gong, L. Yan, K. Zhao, H. Ning, S. Wu, J. Gao, X. Gao, G. Zhou, X. Lu, J. M. Liu, *J. Mater. Chem. C* **2017**, *5*, 10652.
- [20] H. Ebata, T. Izawa, E. Miyazaki, K. Takimiya, M. Ikeda, H. Kuwabara, T. Yui, *J. Am. Chem. Soc.* **2007**, *129*, 15732.
- [21] W. Deng, X. Zhang, H. Dong, J. Jie, X. Xu, J. Liu, L. He, L. Xu, W. Hu, X. Zhang, *Mater. Today* **2019**, *24*, 17.
- [22] Y. Yao, L. Zhang, T. Leydecker, P. Samori, *J. Am. Chem. Soc.* **2018**, *140*, 6984.
- [23] M. R. Reddy, H. Kim, C. Kim, S. Y. Seo, *Synth. Met.* **2018**, *235*, 153.
- [24] C. Liu, Y. Xu, Y. Y. Noh, *Mater. Today* **2015**, *18*, 79.
- [25] T. Minari, P. Darmawan, C. Liu, Y. Li, Y. Xu, K. Tsukagoshi, *Appl. Phys. Lett.* **2012**, *100*, 093303.
- [26] I. Temiño, F. G. Del Pozo, M. R. Ajayakumar, S. Galindo, J. Puigdollers, M. Mas-Torrent, *Adv. Mater. Technol.* **2016**, *1*, 1.
- [27] A. Pérez-Rodríguez, I. Temiño, C. Ocal, M. Mas-Torrent, E. Barrena, *ACS Appl. Mater. Interfaces* **2018**, *10*, 7296.
- [28] M. Dohr, H. M. A. Ehmann, A. O. F. Jones, I. Salzmänn, Q. Shen, C. Teichert, C. Ruzié, G. Schweicher, Y. H. Geerts, R. Resel, M. Sferrazza, O. Werzer, *Soft Matter* **2017**, *13*, 2322.
- [29] G. Gbabode, M. Dohr, C. Niebel, J. Y. Balandier, C. Ruzié, P. Négrier, D. Mondieig, Y. H. Geerts, R. Resel, M. Sferrazza, *ACS Appl. Mater. Interfaces* **2014**, *6*, 13413.
- [30] K. Takimiya, H. Ebata, K. Sakamoto, T. Izawa, T. Otsubo, Y. Kunugi, *J. Am. Chem. Soc.* **2006**, *128*, 12604.
- [31] M.-T. M. Salzillo Tommaso, Campos Antonio, Babuji Adara, Santiago Raul, BromleyStefan T., Ocal Carmen, Barrena Esther, Jouclas Rémy, Ruzie Christian, Schweicher Guillaume, Geerts Yves H., *Adv. Electron. Mater.* **2020**, *30*, 2006115.
- [32] A. Babuji, I. Temiño, A. Pérez-Rodríguez, O. Solomeshch, N. Tessler, M. Vila, J. Li, M. Mas-Torrent, C. Ocal, E. Barrena, *ACS Appl. Mater. Interfaces* **2020**, *12*, 28416.
- [33] S. Kwon, J. Kim, G. Kim, K. Yu, Y. R. Jo, B. J. Kim, J. Kim, H. Kang, B. Park, K.

- Lee, *Adv. Mater.* **2015**, *27*, 6870.
- [34] R. Yamamoto, K. Noda, Y. Wada, T. Toyabe, *Electron. Commun. Japan* **2017**, *100*, 61.
- [35] B. Kořata, V. Kozmik, J. Svoboda, V. Novotná, P. Vaněk, M. Glogarová, *Liq. Cryst.* **2003**, *30*, 603.
- [36] S. Shinamura, I. Osaka, E. Miyazaki, A. Nakao, M. Yamagishi, J. Takeya, K. Takimiya, *J. Am. Chem. Soc.* **2011**, *133*, 5024.
- [37] L. Wang, T. Li, Y. Shen, Y. Song, *Phys. Chem. Chem. Phys.* **2016**, *18*, 8401.
- [38] H. Shirakawa, E. J. Louis, A. G. MacDiarmid, C. K. Chiang, A. J. Heeger, *J. Chem. Soc. Chem. Commun.* **1977**, 578.
- [39] T. Mayer, C. Hein, E. Mankel, W. Jaegermann, M. M. Müller, H. J. Kleebe, *Org. Electron.* **2012**, *13*, 1356.
- [40] I. Salzmann, G. Heimel, M. Oehzelt, S. Winkler, N. Koch, *Acc. Chem. Res.* **2016**, *49*, 370.
- [41] Y. Xu, H. Sun, A. Liu, H. H. Zhu, W. Li, Y. F. Lin, Y. Y. Noh, *Adv. Mater.* **2018**, *30*, 13.
- [42] G. Duva, P. Beyer, R. Scholz, V. Belova, A. Opitz, A. Hinderhofer, A. Gerlach, F. Schreiber, *Phys. Chem. Chem. Phys.* **2019**, *21*, 17190.
- [43] H. Méndez, G. Heimel, S. Winkler, J. Frisch, A. Opitz, K. Sauer, B. Wegner, M. Oehzelt, C. Röthel, S. Duhm, D. Többsen, N. Koch, I. Salzmann, *Nat. Commun.* **2015**, *6*, 8560.
- [44] A. Opitz, *J. Phys. Condens. Matter* **2017**, *29*, 1.
- [45] H. Méndez, G. Heimel, A. Opitz, K. Sauer, P. Barkowski, M. Oehzelt, J. Soeda, T. Okamoto, J. Takeya, J. B. Arlin, J. Y. Balandier, Y. Geerts, N. Koch, I. Salzmann, *Angew. Chemie - Int. Ed.* **2013**, *52*, 7751.
- [46] W. Chen, D. C. Qi, H. Huang, X. Gao, A. T. S. Wee, *Adv. Funct. Mater.* **2011**, *21*, 410.
- [47] B. Lüssem, M. L. Tietze, H. Kleemann, C. Hoßbach, J. W. Bartha, A. Zakhidov, K. Leo, *Nat. Commun.* **2013**, *4*, 2775.
- [48] P. Beyer, D. Pham, C. Peter, N. Koch, E. Meister, W. Brütting, L. Grubert, S. Hecht, D. Nabok, C. Cocchi, C. Draxl, A. Opitz, *Chem. Mater.* **2019**, *31*, 1237.
- [49] I. Salzmann, G. Heimel, S. Duhm, M. Oehzelt, P. Pingel, B. M. George, A. Schnegg, K. Lips, R. P. Blum, A. Vollmer, N. Koch, *Phys. Rev. Lett.* **2012**, *108*, 035502.
- [50] A. Opitz, G. Duva, M. Gebhardt, H. Kim, E. Meister, T. Meisel, P. Beyer, V. Belova, C. Kasper, J. Pflaum, L. Pithan, A. Hinderhofer, F. Schreiber, W. Brütting, *Mater. Adv.* **2022**, *3*, 1017.
- [51] I. Salzmann, G. Heimel, *J. Electron Spectros. Relat. Phenomena* **2015**, *204*, 208.
- [52] H. Kleemann, C. Schuenemann, A. A. Zakhidov, M. Riede, B. Lüssem, K. Leo,



- [53] Y. Xu, H. Sun, A. Liu, H. H. Zhu, W. Li, Y. F. Lin, Y. Y. Noh, *Adv. Mater.* **2018**, *30*, 13.
- [54] B. Lüssem, C. M. Keum, D. Kasemann, B. Naab, Z. Bao, K. Leo, *Chem. Rev.* **2016**, *116*, 13714.
- [55] J. Li, C. W. Rochester, I. E. Jacobs, S. Friedrich, P. Stroeve, M. Riede, A. J. Moulé, *ACS Appl. Mater. Interfaces* **2015**, *7*, 28420.
- [56] I. E. Jacobs, E. W. Aasen, J. L. Oliveira, T. N. Fonseca, J. D. Roehling, J. Li, G. Zhang, M. P. Augustine, M. Mascal, A. J. Moulé, *J. Mater. Chem. C* **2016**, *4*, 3454.
- [57] I. Bruder, S. Watanabe, J. Qu, I. B. Müller, R. Kopecek, J. Hwang, J. Weis, N. Langer, *Org. Electron.* **2010**, *11*, 589.
- [58] P. Strobel, J. Ristein, L. Ley, K. Seppelt, I. V. Goldt, O. Boltalina, *Diam. Relat. Mater.* **2006**, *15*, 720.
- [59] Y. Smets, C. B. Stark, F. Schmitt, M. T. Edmonds, S. Lach, C. A. Wright, D. P. Langley, K. J. Rietwyk, A. Schenk, A. Tadich, M. Wanke, C. Ziegler, L. Ley, C. I. Pakes, *Org. Electron.* **2013**, *14*, 169.
- [60] B. Nell, K. Ortstein, O. V. Boltalina, K. Vandewal, *J. Phys. Chem. C* **2018**, *122*, 11730.
- [61] M. L. Tietze, P. Pahner, K. Schmidt, K. Leo, B. Lüssem, *Adv. Funct. Mater.* **2015**, *25*, 2701.
- [62] S. Kawasaki, T. Aketa, H. Touhara, F. Okino, O. V. Boltalina, I. V. Gol'dt, S. I. Troyanov, R. Taylor, *J. Phys. Chem. B* **1999**, *103*, 1223.
- [63] R. Taylor, *J. Fluor. Chem.* **2004**, *125*, 359.
- [64] B. Nell, K. Ortstein, O. V. Boltalina, K. Vandewal, *J. Phys. Chem. C* **2018**, *122*, 11730.
- [65] R. Mitsumoto, T. Araki, E. Ito, Y. Ouchi, K. Seki, K. Kikuchi, Y. Achiba, H. Kurosaki, T. Sonoda, H. Kobayashi, O. V. Boltalina, V. K. Pavlovich, L. N. Sidorov, Y. Hattori, N. Liu, S. Yajima, S. Kawasaki, F. Okino, H. Touhara, *J. Phys. Chem. A* **1998**, *102*, 552.
- [66] P. K. Koech, A. B. Padmaperuma, L. Wang, J. S. Swensen, E. Polikarpov, J. T. Darsell, J. E. Rainbolt, D. J. Gaspar, *Chem. Mater.* **2010**, *22*, 3926.
- [67] G. Duva, L. Pithan, C. Zeiser, B. Reisz, J. Dieterle, B. Hofferberth, P. Beyer, L. Bogula, A. Opitz, S. Kowarik, A. Hinderhofer, A. Gerlach, F. Schreiber, *J. Phys. Chem. C* **2018**, *122*, 18705.
- [68] R. Kuhrt, M. Hantusch, B. Buechner, M. Knupfer, *J. Phys. Chem. C* **2021**, *125*, 18961.
- [69] V. Vijayakumar, P. Durand, H. Zeng, V. Untilova, L. Herrmann, P. Algayer, N. Leclerc, M. Brinkmann, *J. Mater. Chem. C* **2020**, *8*, 16470.
- [70] Y. Karpov, T. Erdmann, M. Stamm, U. Lappan, O. Guskova, M. Malanin, I. Raguzin, T. Beryozkina, V. Bakulev, F. Günther, S. Gemming, G. Seifert, M.

- Hambusch, S. Mannsfeld, B. Voit, A. Kiri, *Macromolecules* **2017**, *50*, 914.
- [71] R. R. Dasari, X. Wang, R. A. Wiscons, H. F. Haneef, A. Ashokan, Y. Zhang, M. S. Fonari, S. Barlow, V. Coropceanu, T. V. Timofeeva, O. D. Jurchescu, J. L. Brédas, A. J. Matzger, S. R. Marder, *Adv. Funct. Mater.* **2019**, *29*, 1904858.
- [72] A. Tsumura, H. Koezuka, T. Ando, *Appl. Phys. Lett.* **1986**, *49*, 1210.
- [73] H. I. Un, J. Y. Wang, J. Pei, *Adv. Sci.* **2019**, *6*.
- [74] F. Ante, D. Kälblein, U. Zschieschang, T. W. Canzler, A. Werner, K. Takimiya, M. Ikeda, T. Sekitani, T. Someya, H. Klauk, *Small* **2011**, *7*, 1186.
- [75] S. Olthof, S. Mehraeen, S. K. Mohapatra, S. Barlow, V. Coropceanu, J. L. Brédas, S. R. Marder, A. Kahn, *Phys. Rev. Lett.* **2012**, *109*, 1.
- [76] A. F. Paterson, N. D. Treat, W. Zhang, Z. Fei, G. Wyatt-Moon, H. Faber, G. Vourlias, P. A. Patsalas, O. Solomeshch, N. Tessler, M. Heeney, T. D. Anthopoulos, *Adv. Mater.* **2016**, *28*, 7791.
- [77] J. W. Borchert, B. Peng, F. Letzkus, J. N. Burghartz, P. K. L. Chan, K. Zojer, S. Ludwigs, H. Klauk, *Nat. Commun.* **2019**, *10*.
- [78] P. V. Pesavento, R. J. Chesterfield, C. R. Newman, C. D. Frisble, *J. Appl. Phys.* **2004**, *96*, 7312.
- [79] D. He, J. Qiao, L. Zhang, J. Wang, T. Lan, J. Qian, Y. Li, Y. Shi, Y. Chai, W. Lan, L. K. Ono, Y. Qi, J. Bin Xu, W. Ji, X. Wang, *Sci. Adv.* **2017**, *3*, 1.
- [80] K. Pei, A. Ho, Y. Lau, P. Kwok, L. Chan, *Phys. Chem. Chem. Phys.* **2020**, *22*, 7100.
- [81] A. Ablat, A. Kyndiah, G. Houin, T. Y. Alic, L. Hirsch, M. Abbas, *Sci. Rep.* **2019**, *9*, 1.
- [82] M. Kano, T. Minari, K. Tsukagoshi, *Appl. Phys. Lett.* **2009**, *94*.
- [83] T. Breuer, G. Witte, *ACS Appl. Mater. Interfaces* **2013**, *5*, 9740.
- [84] R. Sato, M. Dogishi, T. Higashino, T. Kadoya, T. Kawamoto, T. Mori, *J. Phys. Chem. C* **2017**, *121*, 6561.
- [85] N. Castagnetti, A. Girlando, M. Masino, C. Rizzoli, C. Rovira, *Cryst. Growth Des.* **2017**, *17*, 6255.
- [86] J. Tsutsumi, S. Matsuoka, S. Inoue, H. Minemawari, T. Yamada, T. Hasegawa, *J. Mater. Chem. C* **2015**, *3*, 1976.
- [87] Q. Wei, L. Liu, S. Xiong, X. Zhang, W. Deng, X. Zhang, J. Jie, *J. Phys. Chem. Lett.* **2020**, *11*, 359.
- [88] Y. Kiyota, T. Kadoya, K. Yamamoto, K. Iijima, T. Higashino, T. Kawamoto, K. Takimiya, T. Mori, *J. Am. Chem. Soc.* **2016**, *138*, 3920.
- [89] F. Zhang, X. Dai, W. Zhu, H. Chung, Y. Diao, *Adv. Mater.* **2017**, *29*, 1.
- [90] A. Ashokan, C. Hanson, N. Corbin, J. L. Brédas, V. Coropceanu, *Mater. Chem. Front.* **2020**, *4*, 3623.
- [91] D. Kim, K. Baeg, M. Caironi, C. Liu, Y. Xu, D. Kim, *Adv. Funct. Mater.* **2014**,

24, 6252.

- [92] Y. Xu, H. Sun, E. Shin, Y. Lin, W. Li, Y. Noh, *Adv. Mater.* **2016**, *28*, 8531.
- [93] R. Pfattner, C. Rovira, M. Mas-Torrent, *Phys. Chem. Chem. Phys.* **2014**, *17*, 26545.
- [94] A. V. Kepman, V. F. Sukhoverkhov, A. Tressaud, C. Labrugere, E. Durand, N. S. Chilingarov, L. N. Sidorov, *J. Fluor. Chem.* **2006**, *127*, 832.
- [95] G. C. Binnig, C. F. Quate, *Phys. Rev. Lett.* **1986**, *56*, 930.
- [96] L. Gross, F. Mohn, N. Moll, P. Liljeroth, G. Meyer, *Science (80-. )*. **2009**, *325*, 1110.
- [97] P. Hawkes, J. Spence, *Handbook Microscopy*, **2019**.
- [98] M. H. Korayem, S. Safari, A. Amanati, M. Damircheli, N. Ebrahimi, *Int. J. Adv. Manuf. Technol.* **2010**, *50*, 979.
- [99] Lord Kelvin, *London, Edinburgh, Dublin Philos. Mag. J. Sci.* **1898**, *46*, 82.
- [100] W. A. Zisman, *Rev. Sci. Instrum.* **1932**, *3*, 367.
- [101] W. N. Hansen, G. J. Hansen, **2001**, *481*, 172.
- [102] I. Horcas, R. Fernández, J. M. Gómez-Rodríguez, J. Colchero, J. Gómez-Herrero, A. M. Baro, *Rev. Sci. Instrum.* **2007**, *78*, 013705.
- [103] F. Silvestri, Nanoscale Morphology and Microstructure of Organic Thin Films, UAB, **2021**.
- [104] T. N. Krauss, Structure and morphology of Organic Films of PTCDI-C on Silicon Dioxide, Institut für Theoretische und Angewandte Physik der Universität Stuttgart, **2006**.
- [105] G. Bracco, B. Holst, *Surface Science Techniques*, Vol. 51, **2013**.
- [106] G. R. Castro, *J. Synchrotron Radiat.* **1998**, *5*, 657.
- [107] J. Rubio-Zuazo, P. Ferrer, A. López, A. Gutiérrez-León, I. Da Silva, G. R. Castro, *Nucl. Instruments Methods Phys. Res. Sect. A Accel. Spectrometers, Detect. Assoc. Equip.* **2013**, *716*, 23.
- [108] P. Ferrer, J. Rubio-Zuazo, C. Heyman, F. Esteban-Betegón, G. R. Castro, *J. Synchrotron Radiat.* **2013**, *20*, 474.
- [109] R. Scholz, A.-D. Müller, F. Müller, I. Thurzo, B. A. Paez, L. Mancera, D. R. T. Zahn, C. Pannemann, U. Hillerlingmann, *Org. Field-Effect Transistors IV* **2005**, *5940*, 594001.
- [110] Y. Hu, G. Li, Z. Chen, *IEEE Electron Device Lett.* **2018**, *39*, 276.
- [111] D. S. H. Charrier, M. Kemerink, B. E. Smalbrugge, T. de Vries, R. A. J. Janssen, *ACS Nano* **2008**, *2*, 622.
- [112] K. P. Puntambekar, P. V. Pesavento, C. D. Frisbie, *Appl. Phys. Lett.* **2003**, *83*, 5539.
- [113] L. Bürgi, H. Sirringhaus, R. H. Friend, *Appl. Phys. Lett.* **2002**, *80*, 2913.

- [114] K. Takimiya, T. Yamamoto, H. Ebata, T. Izawa, *Sci. Technol. Adv. Mater.* **2007**, *8*, 273.
- [115] G. Gbabode, M. Dohr, C. Niebel, J. Balandier, C. Ruzié, P. Négrier, D. Mondieig, Y. H. Geerts, M. Sferrazza, G. Gbabode, M. Dohr, C. Niebel, J. Balandier, C. Ruzié, G. Gbabode, M. Dohr, C. Niebel, J. Balandier, C. Ruzie, *ACS Appl. Mater. Interfaces*, Washington, D.C. Am. Chem. Soc. **2018**, *6*, 13413.
- [116] C. Grigoriadis, C. Niebel, C. Ruzié, Y. H. Geerts, G. Floudas, *J. Phys. Chem. B* **2014**, *118*, 1443.
- [117] A. A. Günther, M. Sawatzki, P. Formánek, D. Kasemann, K. Leo, *Adv. Funct. Mater.* **2016**, *26*, 768.
- [118] J. Y. Park, M. Salmeron, *Chem. Rev.* **2014**, *114*, 677.
- [119] C. Ocal, E. Barrena, F. Silvestri, L. Pithan, A. Babuji, *J. Phys. Chem. C* **2021**, *125*, 5363.
- [120] T. Izawa, E. Miyazaki, K. Takimiya, *Adv. Mater.* **2008**, *20*, 3388.
- [121] J. L. Hou, D. Kasemann, J. Widmer, A. A. Günther, B. Lüssem, K. Leo, *Appl. Phys. Lett.* **2016**, *108*, 103303.
- [122] T. Minari, T. Miyadera, K. Tsukagoshi, Y. Aoyagi, H. Ito, *Appl. Phys. Lett.* **2007**, *91*, 053508.
- [123] C. Liu, Y. Xu, Y. Li, W. Scheideler, T. Minari, *J. Phys. Chem. C* **2013**, *117*, 12337.
- [124] W. Zhao, Y. Qi, T. Sajoto, S. Barlow, S. R. Marder, A. Kahn, *Appl. Phys. Lett.* **2010**, *97*, 123305.
- [125] T. Breuer, A. Karthäuser, H. Klemm, F. Genuzio, G. Peschel, A. Fuhrich, T. Schmidt, G. Witte, *ACS Appl. Mater. Interfaces* **2017**, *9*, 8384.
- [126] K. Kniaź, J. E. Fischer, K. Kniaź, J. E. Fischer, G. B. M. Vaughan, W. J. Romanow, J. P. McCauley, R. M. Strongin, A. B. Smith, H. Selig, G. B. M. Vaughan, D. M. Cox, S. K. Chowdhury, J. P. McCauley, R. M. Strongin, A. B. Smith, *J. Am. Chem. Soc.* **1993**, *115*, 6060.
- [127] W. Feng, P. Long, Y. Y. Feng, Y. Li, *Adv. Sci.* **2016**, *3*, 1.
- [128] E. K. Lee, M. Y. Lee, C. H. Park, H. R. Lee, J. H. Oh, *Adv. Mater.* **2017**, *29*, 1.
- [129] A. Babuji, F. Silvestri, L. Pithan, A. Richard, Y. H. Geerts, N. Tessler, O. Solomeshch, C. Ocal, E. Barrena, *ACS Appl. Mater. Interfaces* **2020**, *12*, 57578.
- [130] C. Grigoriadis, C. Niebel, C. Ruzié, Y. H. Geerts, G. Floudas, *J. Phys. Chem. B* **2014**, *118*, 1443.
- [131] A. O. F. Jones, B. Chattopadhyay, Y. H. Geerts, R. Resel, *Adv. Funct. Mater.* **2016**, *26*, 2233.
- [132] A. M. S. Dresselhaus, H. K. K. a Muller, **1995**, 161.
- [133] M. Dohr, O. Werzer, Q. Shen, I. Salzmänn, C. Teichert, C. Ruzié, G.

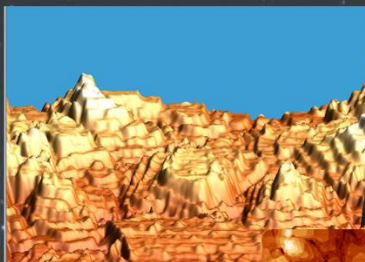
- Schweicher, Y. H. Geerts, M. Sferrazza, R. Resel, *ChemPhysChem* **2013**, *14*, 2554.
- [134] E. Zojer, T. C. Taucher, O. T. Hofmann, *Adv. Mater. Interfaces* **2019**, *6*.
- [135] S. Park, T. Schultz, X. Xu, B. Wegner, A. Aljarb, A. Han, L. J. Li, V. C. Tung, P. Amsalem, N. Koch, *Commun. Phys.* **2019**, *2*.
- [136] J. Niederhausen, P. Amsalem, A. Wilke, R. Schlesinger, S. Winkler, A. Vollmer, J. P. Rabe, N. Koch, *Phys. Rev. B - Condens. Matter Mater. Phys.* **2012**, *86*, 1.
- [137] P. Amsalem, J. Niederhausen, A. Wilke, G. Heimel, R. Schlesinger, S. Winkler, A. Vollmer, J. P. Rabe, N. Koch, *Phys. Rev. B - Condens. Matter Mater. Phys.* **2013**, *87*.
- [138] P. Amsalem, G. Heimel, M. Oehzelt, N. Koch, *J. Electron Spectros. Relat. Phenomena* **2015**, *204*, 177.
- [139] S. Braun, W. R. Salaneck, M. Fahlman, *Adv. Mater.* **2009**, *21*, 1450.
- [140] L. Lyu, D. Niu, H. Xie, Y. Zhao, N. Cao, H. Zhang, Y. Zhang, P. Liu, Y. Gao, *Phys. Chem. Chem. Phys.* **2017**, *19*, 1669.
- [141] N. Koch, A. Gerlach, S. Duhm, H. Glowatzki, G. Heimel, A. Vollmer, Y. Sakamoto, T. Suzuki, J. Zegenhagen, J. P. Rabe, F. Schreiber, *J. Am. Chem. Soc.* **2008**, *130*, 7300.
- [142] I. Salzmann, S. Duhm, G. Heimel, M. Oehzelt, R. Kniprath, R. L. Johnson, J. P. Rabe, N. Koch, *J. Am. Chem. Soc.* **2008**, *130*, 12870.
- [143] R. Schlesinger, S. Winkler, M. Brandt, S. Blumstengel, R. Ovsyannikov, A. Vollmer, N. Koch, *Phys. Chem. Chem. Phys.* **2019**, *21*, 15072.
- [144] and C. I. P. M. T. Edmonds, M. Wanke, A. Tadich, H. M. Vulling, K. J. Rietwyk, P. L. Sharp, C. B. Stark, Y. Smets, A. Schenk, Q.-H. Wu, L. Ley, *J. Chem. Phys.* **2016**, *136*, 124701.
- [145] T. Schultz, T. Lenz, N. Kotadiya, G. Heimel, G. Glasser, R. Berger, P. W. M. Blom, P. Amsalem, D. M. de Leeuw, N. Koch, *Adv. Mater. Interfaces* **2017**, *4*, 1.
- [146] Y. Shibata, J. Tsutsumi, S. Matsuoka, H. Minemawari, S. Arai, R. Kumai, T. Hasegawa, *Adv. Electron. Mater.* **2017**, *3*, 1700097.
- [147] Y. Shibata, J. Tsutsumi, S. Matsuoka, K. Matsubara, Y. Yoshida, M. Chikamatsu, T. Hasegawa, *Appl. Phys. Lett.* **2015**, *106*, 143303.
- [148] P. Tisovský, A. Gáplovský, K. Gmucová, M. Novota, M. Pavúk, M. Weis, *Org. Electron.* **2019**, *68*, 121.
- [149] F. Zhang, A. Kahn, *Adv. Funct. Mater.* **2018**, *28*, 1.
- [150] S. Braun, W. R. Salaneck, *Chem. Phys. Lett.* **2007**, *438*, 259.
- [151] S. Olthof, S. Singh, S. K. Mohapatra, S. Barlow, S. R. Marder, B. Kippelen, A. Kahn, *Appl. Phys. Lett.* **2012**, *101*, 1.
- [152] M. L. Tietze, K. Leo, B. Lüssem, *Org. Electron.* **2013**, *14*, 2348.

- [153] S. G. J. Mathijssen, M. J. Spijkman, A. M. Andringa, P. A. Van Hal, I. McCulloch, M. Kemerink, R. A. J. Janssen, D. M. De Leeuw, *Adv. Mater.* **2010**, 22, 5105.
- [154] R. R. Dasari, X. Wang, R. A. Wiscons, H. F. Haneef, A. Ashokan, Y. Zhang, M. S. Fonari, S. Barlow, V. Coropceanu, T. V. Timofeeva, O. D. Jurchescu, J. L. Brédas, A. J. Matzger, S. R. Marder, *Adv. Funct. Mater.* **2019**, 29, 1.
- [155] J. Zhang, J. Jin, H. Xu, Q. Zhang, W. Huang, *J. Mater. Chem. C* **2018**, 6, 3485.
- [156] J. Li, I. Duchemin, O. M. Roscioni, P. Friederich, M. Anderson, E. Da Como, G. Kociok-Köhn, W. Wenzel, C. Zannoni, D. Beljonne, X. Blase, G. D'Avino, *Mater. Horizons* **2019**, 6, 107.

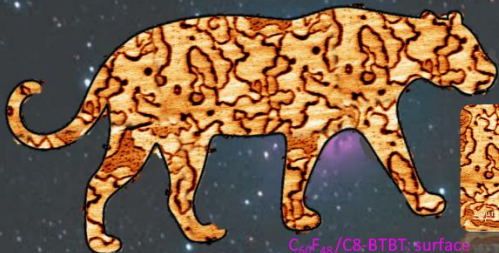
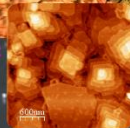




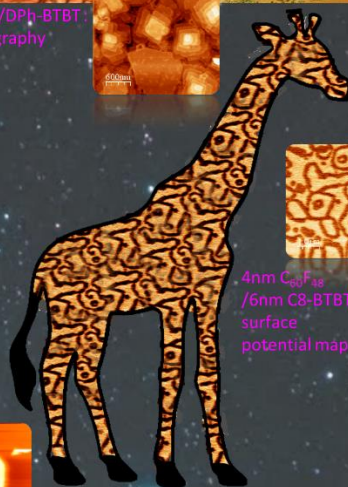
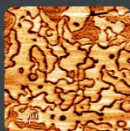
F6TCNNQ/DPh-BTBT:  
Lateral force



$C_{60}F_{48}$ /DPh-BTBT  
Topography



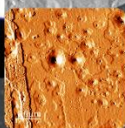
$C_{60}F_{48}$ /C8-BTBT: surface  
potential map



4nm  $C_{60}F_{48}$   
/6nm C8-BTBT:  
surface  
potential map

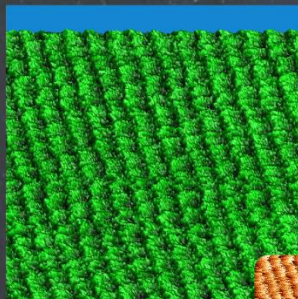
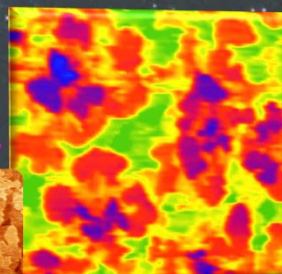
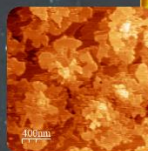


Asymmetric BTBT-C8:  
Topography

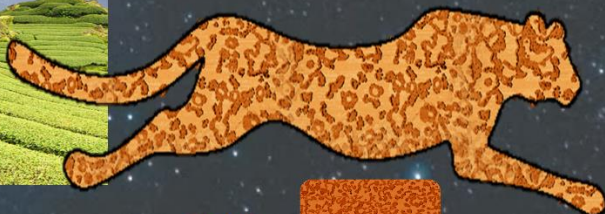


2nm  $C_{60}F_{48}$   
/6nm C8-BTBT:  
OFET:  
Amplitude  
channel

DPh-BTBT:  
Topography



5nm C8-BTBT: Lateral force



4nm  $C_{60}F_{48}$   
/6nm C8-BTBT:  
Lateral force

